TU Delft

Mixed convective heat transfer across a turbulent flow over a porous wall layer

A Numerical Study

ANEEK CHAKRABORTY

Mixed convective heat transfer across a turbulent flow over a porous wall layer

A Numerical Study

by

ANEEK CHAKRABORTY

to obtain the degree of Master of Science

at the Delft University of Technology,

to be defended publicly on Tuesday August 22nd, 2023 at 14:00.

Student number: 5475465.
Project Duration: November 2022 - August 2023.

Thesis committee:

Dr.Ir.Wim-Paul Breugem,	TU Delft, Supervisor, Chair
Dr.Pedro Costa,	TU Delft, Daily Supervisor
Dr. Ir. Jurriaan Peeters,	TU Delft, Committe Member
Dr. Ir. Geert Keetels,	TU Delft, Committe Member

This thesis is confidential and cannot be made public until August 22, 2023.

TU Delft

M. Sc. Thesis

Mixed convective heat transfer across a turbulent flow over a porous wall layer – A numerical study

Energy, Process and Flow Technology – 3ME
TU Delft

Aneek Chakraborty [Student No.: 5475475]

August 17, 2023

Abstract

Thermal convection is a phenomenon seen in almost all facets of life, ranging from planetary convection to ocean currents and convection inside the Earth. The physics of thermal convection complicates when a porous wall layer is present. Flow over urban canopies, forest canopies or flow in underground aquifers are classic examples where thermal convection occurs in the presence of turbulent flow over a medium that may be described as a porous wall layer. The present work focuses on simulating pressure-driven turbulent flow over a simplified, ordered porous medium consisting of a regular array of cubes. The work further couples it with natural convection arising due to unstable stratification, to provide insight into its momentum and heat transfer characteristics.

Direct numerical simulations (DNS) have been performed with a finite-difference Navier-Stokes solver to validate the model for buoyancy-driven convection and the classical Rayleigh-Bénard convection. Further, we extended the solver with a volume penalization Immersed Boundary Method (IBM) to model the ordered porous medium, which was validated against reference data. The bulk Reynolds in the overlying free channel region is fixed at 5500, the Prandtl number at 0.1, with an adiabatic boundary condition on the surface of the cubes. The bulk Richardson number, to cover different flow scenarios, from pure shear to purely buoyancy-driven flows, is also varied. The flow statistics show three distinct regimes spatially, (1) the porous region, (2) the turbulent channel and (3)the *interface regime*, where heat transfer timescales vary drastically between the porous region and the turbulent flow region.

Looking at the regime transition from the perspective of changing Ri_b, the change starts at about bulk Richardson number $Ri_b \approx 0.1$, with the flow switching from mostly buoyancy dominated to shear-dominated convection. The possible regimes as a function of the governing parameters are described, with three regimes formed using critical Rayleigh number limits for convection in free media and in porous media. The qualitative analysis of the thermal structures formed reveals, indeed, that the theorized critical limits are indeed seen through simulations. Lastly, length and velocity scalings are also suggested separately for shear-driven and buoyancy-driven regimes for different regions of the flow domain.

Acknowledgement

Hailing from a city in India where I had lived 22 years of my life, the decision to embark upon a journey to pursue my Masters's in a country 9000 miles away, alone, in the midst of a raging pandemic was probably the most daring decision I had ever taken. Here I was, in a new environment, in the midst of people I had never met before, taking on one of the most challenging academic ventures of my life. Unsurprisingly, looking back at the time period starting two years back, the first thing that comes to mind is not the fluid dynamics equations I learnt or the coding skills I developed. It is the people I met in the Netherlands, the memories I shared with them and the support I received from my friends and family back in India. So this piece of writing is the one unique part of my thesis where I would not talk about turbulence or multiphase flows. Rather, it is a token of my gratitude and thankfulness for the human beings who made this journey possible.

First and foremost, I would like to thank my supervisors Dr. Wim-Paul Breugem and Dr. Pedro Costa. Wim-Paul's guidance throughout the 9 months of this thesis was one of the major driving forces behind it. His weekly meetings over this entire duration have taught me invaluable lessons on how to analyse scientific data, how to derive scaling relations in fluid mechanics and most importantly, what it means to be passionate about a subject. It truly was an enriching experience to work with him. When I started this thesis, my knowledge in handling large-scale codes or high-performance computing was close to negligible. If it was not for Pedro and the hours that he spent listening to and clearing the most basic doubts, this thesis would not have germinated the way it did. His kind demeanour and cheerful nature, coupled with his insane coding skills, is something I aspire to imbibe one day as a computational scientist. I would also like to thank Dr. Jurriaan Peeters and Dr. Geert Keetels for finding time from their schedule and agreeing to be a part of my thesis committee.

Over these two years in Delft, I have had the great fortune to know several wonderful people. When I first arrived in the Netherlands, the burden of assignments forced me to make acquaintances. These acquaintances turned into friends and after two years, I can call them my family away from home. Ali, Sanath, Gokul and Mayanka - this acknowledgement could not have started with anyone else but you all. I do not think I would have survived even a single day if it was not for the companionship I received from you. Be it the dinners or lunches in Ali's house or the long dinners in the Prof. S. common rooms, with conversations ranging from the weirdest, funniest to the most serious of topics, I truly am indebted to all of you for providing me with a safe space - in the better times, but especially in the darker times. Jelle, thanks for being my academic partner in the first year to my part-time volleyball coach in the second year - I truly learnt alot from you. My classmates in EFPT and other friends in TU Delft - Maitreyee, Dimitris, Marina, Julia and Hamza I have learnt something or the other from all of you. I really look forward to seeing what all of you achieve in your lives. Further, I would also thank the professors of all the courses I undertook during my Masters. It truly was a steep learning curve and I could not have done it without your guidance.

Abhyuday, you were a great senior during my Bachelor and your guidance in the formative years of my Master's has been equally invaluable. I truly cannot wait to start the next chapter of my life in your department - quite a funny transition from being your junior once to being your colleague. My Bengali gang in the Netherlands - Leonid, Sayantan, Sagnik, Anirban, Somnath, I am thankful that you included me in your lives and I look forward to future get-togethers and Nolan movie screenings. Aryama, you are probably my closest friend from my Bachelor days, thanks for being there on the gloomiest of days, even if not in person, but rather in spirit. Our conversations have always been enriching and I am lucky to have you as a friend. The people I met 6 years back during my Bachelor days - Aditya, Sohail, Shuvayan, Ritwika, Arkava - I am glad we kept in close contact, even years after I left my Bachelor days behind. It would be unfair to not talk about two people who influenced my life in unique ways over the last few years. Akriti, you were a driving force behind what I have achieved today and you truly were my best friend. The two years we knew each other, it was simply some of the best times I have spent in my life - be it the video calls on a winter evening in Delft or the scooter ride in Kolkata. I hope you achieve everything that you aspire for. Isabella, knowing you were probably one of the best things that happened to me in the Netherlands. After the first year of Master where my social life had almost

taken a toll, getting to know you was like a breath of fresh air. Be it the walks through the lanes of Hague or exploring the most unknown cafes in some forlorn alley - I was lucky that I got you as a friend in my life.

I know one person who would be extremely proud to see where I am today - Dida, my grandmother. I hope you are watching from wherever you are and that you keep showering your love and blessings like you used to. Baba (father), I have been a first-hand witness to the effort you put in from my school admission days to my college days and even till date- all to see me become something that you probably aspired to be. I am grateful for all that love and I hope I make you proud one day. Lastly, ma (mother), my unsaid best friend in the world. Simply put, I would be nowhere without the sacrifices you made, throughout my 24 years of existence. Your fierce intelligence, unwavering kindness and resilience in the face of crisis are some of the life lessons I hope to inculcate in myself. I hope that someday I will achieve everything you had dreamt of and make your sacrifices worth it.

It's a monumental task to summarize one's gratitude and thankfulness within a page or two because of whom this journey was possible. I tried my best. All these people have knowingly and unknowingly helped me reach this junction - and I am really glad I have had all of them in my life. Lastly, I am glad I made the daring gamble of choosing Process and Energy for my Masters. As my favourite quote from The Office summarizes it:
"You miss 100% of the shots you don't take.
-Wayne Gretzky "
-Michael Scott.

"Theory can only take you so far."

Oppenheimer

Contents

List of Tables

List of Figures

1

Introduction

Thermal convection is the phenomenon arising in fluids when less dense, warmer fluid rises up and denser, colder fluid comes down, under the influence of gravity, giving rise to natural circulation. Such convection is seen throughout nature, occurring over several decades of length and time scales. From atmospheric systems and planetary motions to the heating of water on a stove, heat and momentum transfer through convection is among the most common phenomena present around us. Over the last few decades, understanding how natural convection is intertwined with several other physical mechanisms occurring around us has been the object of study in the scientific community (see Figure 1.1). Starting from geothermal convection, which is one of the main modes of heat transfer from earth's crust Anderson et al. (1979) and convection patterns in ocean currents (Marshall and Schott (1999)) to the formation of convection-driven 'Hadley' cells, which are the rolls formed when hot air rises up in the Earth's atmosphere near the Equator, resulting in circulation (Hadley (1735)), convection drives almost all large-scale processes in the biosphere. Even in other planetary systems like that of Jupiter and Saturn, the vortical storms present on their surface have their origin in deep planetary convection, which can be simplified into a form of rotating Rayleigh-Bénard convection (Yadav et al. (2020)). The polygonal cell-shaped surfaces on Pluto can also be attributed to planetary Rayleigh-Bénard convection (Trowbridge et al. (2016)). At scales closer to our everyday experience, in ventilation systems, convective circulation plays a major role, mainly in urban settings and both experimental and numerical investigations have been performed to study and improve such ventilation patterns (Ziskind et al. (2002); Dubovsky et al. (2001)). Finally, a separate field of study became relevant in the past several years concerning convection in biological systems or 'bioconvection' concerning the patterns formed by self-organized flow due to microorganisms in liquid cultures (Bees (2020)), though this form of convection is driven by concentration differences, not thermal gradients.

Convection in porous media – be it free/natural (without mean external flow) or forced (with external flow) – is a more complex problem as far as the underlying physics is concerned. These types of flows also abound in the environment and in industry, such as in oil extraction, underground aquifers for carbon dioxide sequestration, and the flow over densely built urban settlements, referred to as urban canopies in literature (see Figure 1.2). In particular, atmospheric flow over rural (for instance, a forest) or urban canopies has been extensively studied as flow over porous media by modelling the canopy as a porous layer (adopting a continuum approach to model the canopy). Studying flow over urban settlements is particularly important because with the help of reliable modelling results, long-standing problems related to floods or rising temperatures can be resolved. Coceal et al. (2006) analysed flow over cubical porous-media-like obstacles by performing Direct Numerical Simulations (DNS), and described the flow over urban canopy by spatially

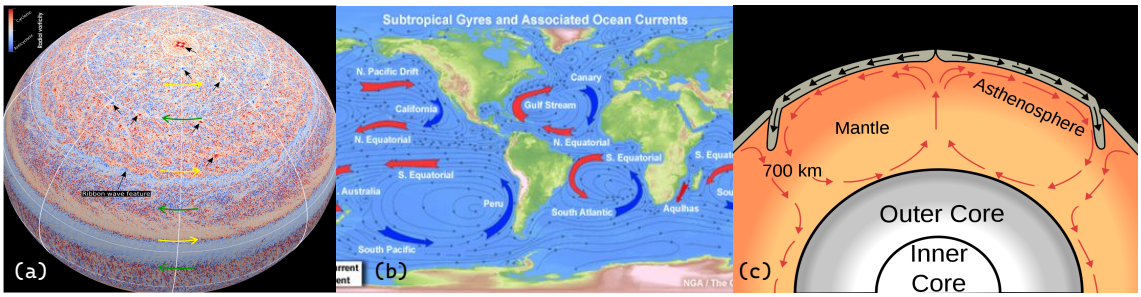

Figure 1.1: (a): Vortical storms due to deep convection currents in Jupiter (Yadav et al. (2020)); (b): Convection currents in oceans (Meteorology (2011));(c): Convection in the mantle of the earth (Wikipedia (2007)).

averaging the flow statistics. It was found that unsteady effects play a determining role in the lower canopy layer (see also Coceal et al. (2007)). Similar modelling approaches can also be found in the work by Kristóf and Papp (2018) who used Large-Eddy Simulations (LES) to model urban dispersion, described as a porous medium formed by cuboidal elements. Further work was also done by Santiago and Martilli (2010), who used mesoscale models for modelling this type of system. Another major field where convection in porous media plays a huge role is in carbon-dioxide sequestration in aquifers. For instance, De Paoli et al. (2016) numerically analysed buoyancy-driven distribution of solute concentration in porous media with anisotropic permeability; Hong and Kim (2008) used a theoretical analysis in saturated anisotropic porous media to derive stability conditions for buoyancy-driven flows; and Hassanzadeh et al. (2009) performed a linear stability analysis in carbon-dioxide-saturated brine in porous aquifers, designed to reduce carbon dioxide leaks. Applications of convective flows in porous media can also be found in other fields, such as microelectronics (Park and Bergles (1987)) and thermal energy storage (Nagano et al. (2002)).

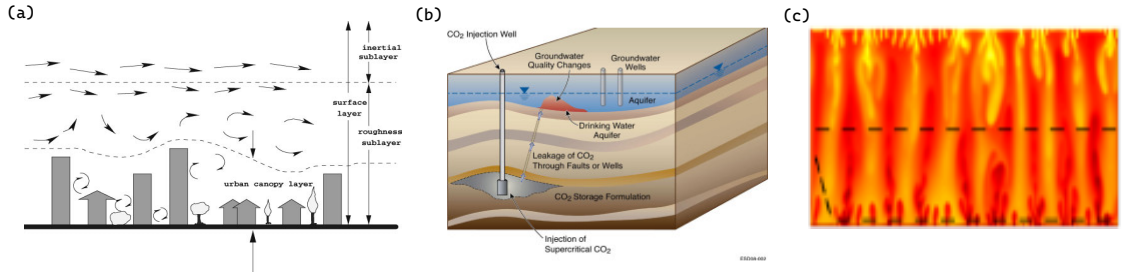

Figure 1.2: (a): Flow over urban canopy modelled as flow over obstacles (which can be extended to porous media)(Britter and Hanna (2003)); (b): Carbon dioxide aquifers (Birkholzer (2009)); (c): Buoyancy driven convection in aquifers as shown by De Paoli et al. (2016).

These examples share the same basic model governing their physics - turbulent flow across a porous wall layer, in the presence of thermal convection. In all the flow situations discussed, ranging from flow over urban canopies to flow in aquifers, the physics stems from the interaction between the turbulent flow and the porous layer.

This transition regime from flow in a clear region to flow between the porous wall layers has a spectrum of underlying governing principles, which makes the study of this problem both complicated and highly interesting. Turbulent flow over urban canopies, as described above, has been investigated, but the physics that has been uncovered in literature merely scratches the surface. This is precisely the problem that will be tackled in this M.Sc. thesis. A schematic of the problem is shown in Figure 1.3.

To study numerically this challenging problem, a clear workflow must be established. Along with the physics, the approach which will be taken to simulate this problem is also nontrivial. A hoard of parameters come into play, starting from buoyancy forces, their interplay with the viscous forces especially in the porous layer, the forced convection caused due to the turbulent flow and the microstructure of the porous medium itself. To tie all these factors together, a well-structured literature review focusing on both the physics and the approach is necessary.

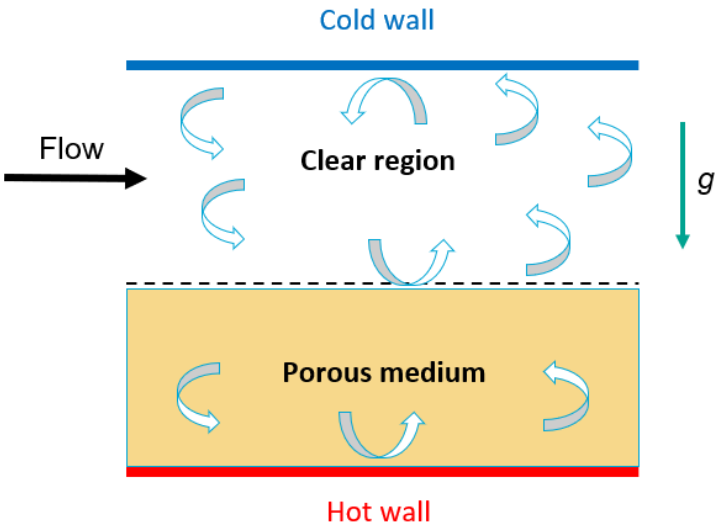

Figure 1.3: Schematic of the problem to be investigated in the present thesis. The convection is represented by the rolls, whereas the flow direction is shown by the black arrow.

The chapters in this thesis are arranged as follows:
Chapter 1 - Introduction.
Chapter 2 - Literature Review: An overview of the existing literature on natural convection in free and porous media, along with turbulent flow.
Chapter 3 - Research goals: Defines the scope and research goal of the present thesis.
Chapter 4 - Methods: The section describes the main research goal of the thesis, followed by a section on the numerical methods used. The implementation of the IBM algorithm is also described in detail.
Chapter 5 - Geometry, Mesh and Implementation: This section elaborates on the geometry and parameters used in the modelling, along with the mesh specifications.
Chapter 6 - Validation: Validation of the buoyancy-driven convection, Rayleigh-Bénard convection and turbulent flow over porous medium.
Chapter 7 - Results: This section starts by defining the governing parameters and moves on to statistical and qualitative analysis of flow statistics. Finally, a regime map is defined to bind together the flow regimes identified.
Chapter 8 - Conclusions and Recommendations: Provides a summary of the results obtained with future recommendations.

2

Literature review

The literature review is divided into two parts, the first one focusing on the physics behind the problem and the second one on the approach this thesis takes to solve that problem. In the beginning, the fundamentals and the literature behind buoyancy-driven convection, without and with a porous layer, are explained. Following that, turbulent flow characteristics over a porous layer are elaborated on. Finally, the two discussions are made to converge, to analyse the problem in question – the turbulent flow over a porous wall layer in the presence of mixed convection.

2.1 Buoyancy-driven convection

The fundamental physical concept behind the origin of buoyancy-driven flows is in the formation of a temperature gradient across a fluid domain in the presence of a body force, in most cases gravity. Buoyancy-driven flows can also originate due to other factors, where the density gradient arises due to differences in a scalar concentration (e.g., salinity). However, in the present thesis, the focus is placed on thermally-driven convection only. With increasing temperature, the fluid in the bottom of the system becomes less dense, and rises up, while the cooler, less dense fluid sinks down. This creates circulatory patterns, governed by the interplay between buoyancy forces and viscous forces. This ratio between the buoyancy and viscous forcing is known as the Rayleigh number denoted by Ra, to be defined later in section 2.2. Moreover, the ratio between momentum diffusivity and thermal diffusivity also plays a part in the thermal transport by the fluid momentum, which is characterized by the Prandtl number Pr. Le Quéré (1991) studied buoyancy-driven flows inside a differentially heated cavity (i.e., with the temperature gradient perpendicular to gravity), for varying Ra for 10^6, 10^7 and 10^8.The Nusselt number (Nu) was analysed for these three cases. Very recently, Yang et al. (2021) used Smoothed Particle Hydrodynamics (SPH) to analyse Nu and flow characteristics for Ra varying from 10^4 to 10^9. The authors further extended their study to compare the buoyancy force and pressure gradient force contribution on the acceleration for varying Ra. The next section focuses on a specific case of buoyancy-driven flows – Rayleigh Bénard convection.

2.2 Rayleigh-Bénard convection

Rayleigh-Bénard convection is among the most widely studied buoyancy-driven flows, where the temperature gradient is aligned with gravity (see Figure 2.1). The most remarkable feature of Rayleigh-Bénard convection is the formation of convection cells (or 'Bénard' cells) which are large-scale convection rolls formed when the upper boundary of a planar fluid domain is cooled and the lower boundary is heated up. Lord Rayleigh first tried to support Bénard's experiments on the formation of convection rolls in a horizontal domain of fluid (Rayleigh (1916)) with an analytical model. He proved the formation of convection cells with the liquid motion being in ascension in the middle of a cell and descension at the boundary of the cells, resulting in a circulatory pattern, as seen in Figure 2.1 .

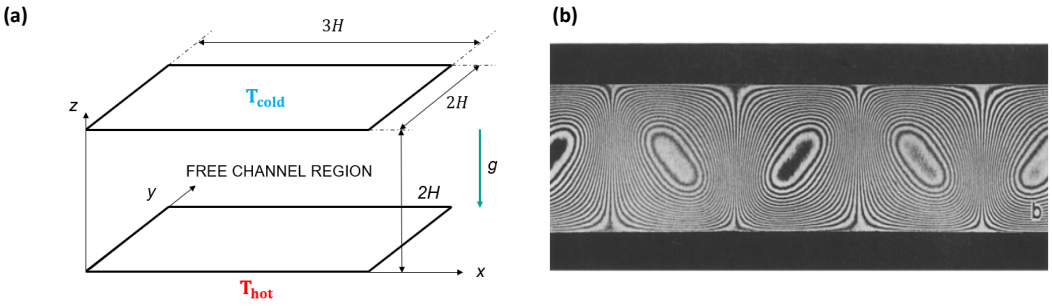

Figure 2.1: (a) Schematic to represent the setup for Rayleigh Bénard convection; (b) Rayleigh Bénard convection in a horizontal fluid domain at Rayleigh number $Ra = 3000$ (Bühler et al. (1979))

To analyse the physics of this problem, it is important to consider the buoyancy effects which appear in the fluid domain given by the Oberbeck-Bousinessq approximation (Oberbeck (1879)), later modified by Bousinessq (1903). This approximation assumes that density ρ is independent of pressure, and varies with temperature T linearly. These can then be related as: $\rho = \rho_0(1 - \alpha(T - T_{ref}))$, where α is the volumetric coefficient of thermal expansion. If the variations in density throughout the domain are small, effects of variable inertia may be neglected, and buoyancy effects can be simplified to a buoyancy momentum source term, which can be directly related to the gravitational acceleration g and the local temperature difference $T - T_{ref}$; here T_{ref} is taken as the mean temperature between the hot and cold walls (see Figure 2.1)). This results in a very simple coupling between the transport of thermal energy and of momentum, which can however represent, with high fidelity, the dynamics of systems undergoing thermal convection with small density variations.

Before delving further into the physics of Rayleigh-Bénard convection, it is important to introduce the Rayleigh number Ra and how it emerges from the governing equations.
The Navier-Stokes equations for an incompressible flow with the Oberbeck-Bousinessq approximation Oberbeck-Bousinessq approximation, are given as:

$$\nabla \cdot \mathbf{u} = 0, \tag{2.2.1}$$

$$\rho_f \frac{\partial \mathbf{u}}{\partial t} + \rho_f \nabla \cdot \mathbf{u}\mathbf{u} = -\nabla p + \mu_f \nabla^2 \mathbf{u} + \rho_f \mathbf{g}\alpha(T - T_{ref}). \tag{2.2.2}$$

Further, the energy equation is given as:

$$\rho c_p \frac{\partial T}{\partial t} + \rho c_p \nabla \cdot \mathbf{u}T = k\nabla^2 T. \tag{2.2.3}$$

From Figure 2.1, the characteristic length scale can be chosen as H, the time scale τ as $\frac{H^2}{\kappa}$ and thus the velocity scale U_c as $\frac{\kappa}{H}$. The incompressible Navier-Stokes equations, normalized by

characteristic scales, are given as:

$$\frac{U_c}{H}\nabla^*\cdot\mathbf{u}^* = 0, \tag{2.2.4}$$

$$\frac{\partial \mathbf{u}^*}{\partial t^*} + \frac{U_c\tau}{H}\nabla^*\mathbf{u}^*\mathbf{u}^* = -\frac{U_c\tau}{H}\frac{\nabla^* P^*}{\rho^*} - \frac{\alpha\Delta T_c\tau^2}{H}\mathbf{g}T^* + \frac{\nu}{\kappa}\nabla^{*2}\mathbf{u}^*, \tag{2.2.5}$$

$$\frac{\partial T^*}{\partial t^*} + \frac{U_c\tau}{H}\mathbf{u}^*\cdot\nabla^* T^* = \frac{\kappa\tau}{H^2}\nabla^{*2}T^*. \tag{2.2.6}$$

This can further be simplified to:

$$\nabla^*\cdot\mathbf{u}^* = 0, \tag{2.2.7}$$

$$\frac{\partial \mathbf{u}^*}{\partial t^*} + \nabla^*\cdot\mathbf{u}^*\mathbf{u}^* = -\frac{\nabla^* P^*}{\rho^*} - Ra\ Pr\ \hat{g}T^* + Pr\nabla^{*2}\mathbf{u}^*, \tag{2.2.8}$$

$$\frac{\partial T^*}{\partial t^*} + \mathbf{u}^*\cdot\nabla^* T^* = \nabla^{*2}T^*. \tag{2.2.9}$$

Thus it is seen that Ra and Pr are the two main dimensionless numbers appearing which are relevant to the present problem.

The Rayleigh number dictates precisely the relative importance of buoyancy forcing over the viscous forcing in the transport of thermal energy and is given by:

$$\boxed{Ra = \frac{\alpha(T - T_{ref})gH^3}{\nu\kappa}.} \tag{2.2.10}$$

Further, the Prandtl number determines the importance of momentum diffusivity over thermal diffusivity, given as:

$$\boxed{Pr = \frac{\nu}{\kappa}.} \tag{2.2.11}$$

When the Rayleigh-Bénard convection process starts between two horizontal plates, velocity and thermal boundary layers are formed along the upper and lower plates. These boundary layers actively participate in the heat transfer process in the near wall region and in the global heat transport in the fluid layer. The problem can thus be simplified to be a system where the Rayleigh number and Prandtl number (Pr) are the control parameters that are known a priori, and the output is in the form of Nusselt number:

$$Nu = \frac{QH}{k\Delta T}, \tag{2.2.12}$$

where Q is the heat flux and k is the thermal conductivity of the fluid and the convective Reynolds number:

$$Re_{conv} = \frac{U_{conv}H}{\nu}, \tag{2.2.13}$$

where U_{conv} characterizes the convective velocity scaling. Since the Re_{conv} is $f(Ra, Pr)$, the velocity scaling can be derived to be:

$$U_{conv} \sim \sqrt{\alpha\Delta T g H}. \tag{2.2.14}$$

The Prandtl number controls the relative thickness of the velocity and thermal boundary layers, while the temperature gradient in the domain, which is the steepest within the thermal boundary layer, affects the Nusselt and Reynolds numbers. Therefore it is key to determine the exact relations between Nu, Ra and Pr. Extensive work has been performed on coming to a consensus about the dependence of Nu on Ra and Pr (Ahlers et al. (2009), Chillà and Schumacher (2012)). The earliest work in this aspect can be traced back to Malkus and Chandrasekhar (1954), where the upper limit to turbulent heat transport being restricted by the smallest eddy size is investigated, along with the stability regime within which perturbations do not become unstable in the boundary layer (theory of marginally stable thermal boundary layer). This led to a considerably large body of work (Grossmann and Lohse (2000, 2001, 2004); Ahlers et al. (2009)), which led to the Grossman-Lohse theory. Indeed, Grossmann and Lohse (2000) proposed Nu and Re scaling as a function

of Ra and Pr, with the assumption of large scale convection circulations (termed as 'wind of turbulence' by the authors); this assumption breaks down below $Re \sim 50$), by dividing the domain into four regimes based on the dissipation rate of mechanical kinetic energy (ϵ_u) or dissipation rate of thermal energy (ϵ_θ). On the basis of this classification, the regime may either be dominated by the boundary layer (BL), or by the bulk dynamics:

$$\epsilon_u = \epsilon_{u,BL} + \epsilon_{u,bulk}, \tag{2.2.15}$$

$$\epsilon_\theta = \epsilon_{\theta,BL} + \epsilon_{\theta,bulk}. \tag{2.2.16}$$

More specifically, the four regimes are: (I) Both ϵ_u and ϵ_θ dominated by BL; (II) ϵ_u dominated by bulk but ϵ_θ dominated by BL; (III) ϵ_θ dominated by bulk but ϵ_u dominated by BL and (IV) Both ϵ_u and ϵ_θ dominated by bulk of fluid domain. The GL theory is formulated in a way such as with experimental data, the pre-factors of the scalings can also be derived, thus providing a universal theory of predicting $Nu(Ra, Pr)$ and $Re(Ra, Pr)$. Later, this theory was formulated for higher Pr by Grossmann and Lohse (2001). Moreover, Grossmann and Lohse (2004) extended the GL theory, decomposing ϵ_θ into plume (also referred to as detached thermal BL) and non-plume (background) regimes, mainly to model heat transfer in near-wall (plume-dominated) regions and core (background or non-plume) regions:

$$\epsilon_\theta = \epsilon_{\theta,plume} + \epsilon_{\theta,background}. \tag{2.2.17}$$

The classical 1/3 scaling between $Nu - Ra$ was formulated based on the work by Malkus and

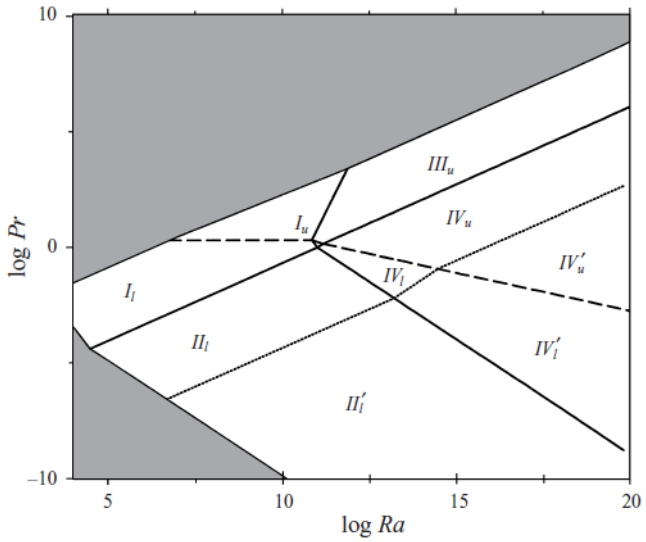

Figure 2.2: The Pr-Ra plane by Grossmann and Lohse (2000) with the 4 regimes of RB convection (u represents the high Pr cases and l represents the low Pr cases). The present thesis is focused on $Pr = 0.1$ at lower Ra, which corresponds to region I_l.

Chandrasekhar (1954) and later verified by Grossmann and Lohse (2000) for region where both ϵ_u and ϵ_θ dominated by bulk. As noted in the textbook by Nieuwstadt et al. (2016), this 1/3 scaling is seen when the flow is over hydraulically smooth walls. Heat transfer characteristics for turbulent BLs were investigated by Shraiman and Siggia (1990) for fluids with $Pr \gg 1$ and high Ra (a regime where thermal BL is completely nested within viscous BL). They derived a scaling for $Nu(Ra, Pr)$ as $Nu \sim 0.27 Ra^{\frac{2}{7}} Pr^{-\frac{1}{7}}$. This 2/7 scaling is in close agreement with the results from Castaing et al. (1989), who found a scaling estimate of 0.282 ± 0.006 from a $Nu - Ra$ correlation derived from experimental results with Helium in a Ra regime extending from around 10^6 (soft turbulence) to 10^{12}(hard turbulence) (Heslot et al. (1987) explains soft turbulence as a regime extending from $Ra = 2.5 \times 10^5$ to $Ra = 4 \times 10^7$ where convective rolls are seen. Similarly hard turbulence is the regime extending from $Ra = 4 \times 10^7$ for about 4 decades, characterized by plumes detaching from an oscillating boundary layer). Castaing et al. (1989) built his work on the foundation laid by Kraichnan (1962), where the $Nu - Ra$ scaling is formulated to be asymptotically approaching $\frac{1}{2}$ at high Ra. The deviation from the classical 1/3 scaling is justified due to the enhanced stirring near boundary layers which arise due to shear layers attached to eddies. Nieuwstadt et al. (2016)

derived the same scaling for hydraulically rough walls, where the reasoning of enhanced stirring given by Kraichnan, holds. This scaling is also further verified by the work of Grossmann and Lohse (2000), when ϵ_θ and ϵ_u are both bulk dominated and Pr is low. However, their conclusion for high Pr in this regime supports the 1/3 law, which is a deviation from Kraichnan (1962), probably due to the laminar assumption. Finally, in the present thesis, the focus will be placed on $Pr = 0.1$, as shown in Figure 2.2. From Grossmann and Lohse (2000) and Figure 2.2, the scaling which will be necessary to serve as a comparison to scalings obtained in the present work (mixed convection in the presence of porous wall layer) is given as $Nu \sim Ra^{\frac{1}{4}} Pr^{\frac{1}{8}}$ as seen from Grossmann and Lohse (2000).

2.2.1 Direct numerical simulations of Rayleigh-Bénard convection

Over the past few decades, due to the obvious limitations of analysing Rayleigh-Bénard convection using experiments, various numerical studies using direct numerical simulations have been carried out to study the dynamics of these flows in great detail. RB convection has been simulated for air ($Pr = 0.71$) inside an infinite horizontal channel by Grötzbach (1982), with the Ra being increased to identify the change in regimes. Around $Ra = 1500$, stable stratification is seen with conduction as the primary mode of heat transfer (similar regime identified by Krishnamurti (1973)). The critical Ra, beyond which convection starts, is around 1700. By $Ra = 7000$, non-steady 3D vortical structures start forming, which is also seen in the work by Shan (1997). Then, around $Ra = 87\,000$, the convection field becomes turbulent and the movement of hot and cold plumes from the walls becomes chaotic. Grötzbach (1982) extended his simulation until $Ra = 3.8 \times 10^5$ where it is seen the large-scale structures grow smaller in spatial dimensions.

Kaczorowski and Wagner (2009) performed DNS of RB convection at even higher Ra, starting from 3.5×10^5 up to 2.31×10^8, and demonstrated the start of transition regime towards hard turbulence over this range. They observed that, with increasing Ra, turbulent thermal dissipation rates increase in BL whereas kinetic dissipation rate dominates in the core. They also found the scaling for the thickness of thermal BL as $\delta_t = 1/2\ Nu$ which matches with the findings from Grossmann and Lohse (2000). The velocity spectra follow $-5/3$ law in the centre, while the thermal energy spectra follow the Bolgiano scaling with $-7/5$ scaling in the equilibrium range. One of the most crucial qualitative deductions was that thermal plumes which originate from the near wall region convert the thermal energy to kinetic energy, which ultimately gives rise to the circulation present in RB convection. A more detailed analysis based on the probability distribution function of thermal dissipation rate shows that the domain can be divided into three regions - bulk, plumes and conductive sub-layer.

The range of Ra investigated above will be instrumental, to serve as a benchmark in this thesis for validating the Rayleigh-Bénard convection model developed, before considering the effects of a porous medium in the system.

2.3 Convection in a porous layer

The presence of a porous layer inside a fluid domain complicates the physics of convection. From the macroscopic Volume-Averaged Navier-Stokes (VANS) equations, it is seen that an extra drag term appears due to the solid matrix inside the fluid as derived by Whitaker (1998). In the laminar regime, this drag term is linear and this is referred to as the Darcian regime in literature (Darcy's law is valid in this regime, which is explained later in this section). Forchheimer (1901) provided a correction to the classical Darcy's law to include inertial effects when the flow undergoes a transition from laminar to the turbulent regime, naturally termed as the non-Darcy regime.
Before delving into the physics behind convection in porous media (a schematic is presented of the simplified geometry in 2.3), it is necessary to introduce a few governing parameters.

- Porosity (ϕ) – It is the fraction of the total volume inside the porous domain which is occupied by void space volume.

- Permeability (K) – In uniform porous media, permeability can be seen as the ease of percolation inside the porous media. In other words, a more permeable porous media effectively has a lower pressure drop for fluid passing through it. Permeability has units of length squared, so often its square root is taken to be the effective pore size. Darcy found that steady-state flow showed a proportional relation between flow rate and applied pressure difference. This is known as Darcy's law, denoted by:

$$\mathbf{v} = \mu^{-1}\mathbf{K} \cdot \nabla P \tag{2.3.1}$$

  Here, $\mathbf{K}$ is known as intrinsic permeability and depends closely on the geometry of the medium. In the case of anisotropic media, $\mathbf{K}$ becomes a second-order rank tensor. Here $\mathbf{v}$ is the macroscopic superficial velocity vector and μ is the fluid dynamic viscosity.

- Effective thermal conductivity (k_{eff}) – In the present topic, where convection in porous media is being dealt with, it is important to arrive at an expression for the effective thermal conductivity for the porous region. Inside a porous region, the thermal conductivity is greatly affected by the topology and geometry of the solid matrix. So the investigation of any physical phenomena inside porous media requires a clear understanding of the effective thermal conductivity as a first step.
  If heat conduction in solid and fluid phases occurs in parallel (the temperature gradient is the same between both phases, but heat flux is divided) then effective conductivity k_{eff} is:

$$k_{eff} = (1-\phi)k_s + \phi k_f \tag{2.3.2}$$

  and if heat conduction takes place in series (the heat flux is the same between both phases, but the temperature gradient is different), effective conductivity k_{eff} is:

$$k_{eff} = \frac{k_s k_f}{(1-\phi)k_f + \phi k_s}. \tag{2.3.3}$$

  However, in cases where there is simultaneous parallel and series heat transfer, a rough estimate is given by using the weighted geometric mean:

$$k_{eff} = k_s^{1-\phi} k_f^{\phi} \tag{2.3.4}$$

  where k_s is conductivity of solid and k_f is conductivity of fluid. J.C.Maxwell (1873) proposed a thermal conductivity model for more complex situations where expressions for effective conductivity of a heterogenous medium (dilute suspension of spherical particles of conductivity k_s in a continuous matrix of conductivity k_f), given by:

$$k_{eff} = k_f \left(1 + \frac{3\phi}{\frac{k_s+2k_f}{k_s-k_f} - \phi} \right) \tag{2.3.5}$$

  More complicated models to find effective thermal conductivity have also been proposed which will be dealt with later in the thesis.

Lapwood (1948) and Horton and Rogers (1945) provided a fundamental study on the marginal stability of fluid domain inside a porous media under a vertical temperature gradient with gravity. It was shown that on satisfying these stability criteria, convective flow may occur inside such a domain. Like the Rayleigh number controlling convection in a fluid domain without the influence of porous media, the Rayleigh Darcy number is the dimensionless quantity used to control convection in a fluid-filled porous media, given by:

$$\boxed{Ra^* = Ra \times Da = \frac{gH^3(T_{hot}-T_{cold})\alpha}{\nu\kappa} \times \frac{K}{H^2} = \frac{gHK(T_{hot}-T_{cold})\alpha}{\nu\kappa}.} \tag{2.3.6}$$

Otero et al. (2004) studied porous medium convection and heat transport over a range of Rayleigh-Darcy numbers from the onset of convection at $Ra^* = 4\pi^2$ (Lapwood (1948)) to $Ra^* = 10^4$. With increasing Ra^*, the flow structure goes from steady-state to chaotic dynamical states, and two

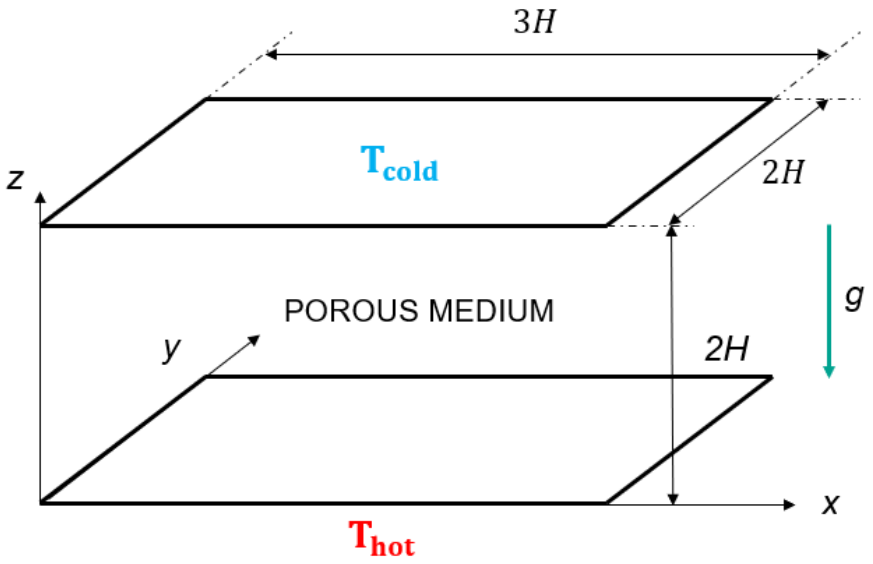

Figure 2.3: Schematic to represent setup for convection inside porous media

distinct regimes can be identified. From the onset of convection to a range of moderate Ra^* (about $Ra^* = 1300$ as found by Hewitt et al. (2012)), time-dependent convection rolls develop, which is analogous to the Rayleigh-Bénard convection seen in (Grötzbach (1982); Kaczorowski and Wagner (2009)) and the $Nu \sim Ra^*$ scaling behaviour is seen. However, at higher Ra^* turbulence sets in and instead of convection rolls, at first blobs of hot and cold fluid are seen which slowly give way to more organised columnar plume structures (Hewitt et al. (2012)). This regime is better described by $Nu \sim Ra^{*0.9}$ scaling which is a deviation from the conventional scaling described above. Hewitt et al. (2012) extended this work to find and qualitatively describe the regimes

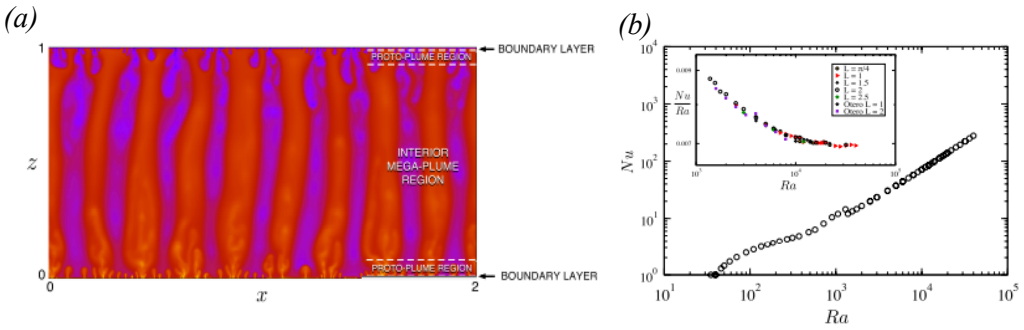

Figure 2.4: (a) The plume regimes - metaplume and protoplume ; (b) The Nu with Ra graph (inset shows the independence of Nu from aspect ratio (Hewitt et al. (2012)).)

in the plume structures seen in the high Ra^* regime. The interior of the domain is dominated by vertical heat exchange columns or 'megaplumes', whereas, at the boundaries of the domain, short wavelength instabilities give rise to 'protoplumes'. The transition zone is dominated by a protoplasm mixing layer, giving rise to the columnar megaplumes. Even though the domain is dominated by such columnar structures, surprisingly the Nu was asymptotically independent of the aspect ratio. The sudden discontinuity seen in Figure 2.4 around $Ra^* = 1300$, denotes the sudden change in regime from soft to hard turbulence, which is also visible in the contours presented by Hewitt et al. (2012). This work was further extended by the author (Hewitt (2020)) to also analyse the scenario where convection effects are induced through one surface only instead of both top and bottom in case of typical RB convection, though this is outside the purview of this thesis.

Nithiarasu et al. (1997) worked on comparing convective heat transfer in uniformly porous media with variable porosity media, and extended his work to compare the heat transfer in the

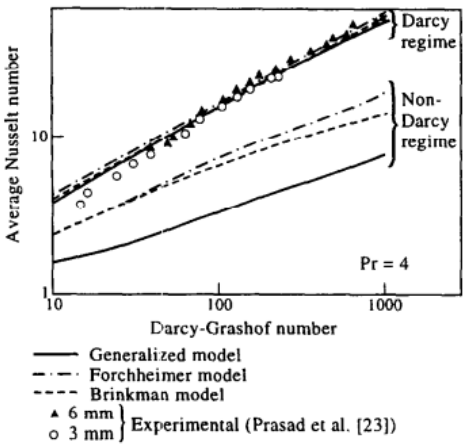

Figure 2.5: Comparison of Nithiarasu et al. (1997) with Brinkmann and Forcheimmer models in non-Darcy regime ; and with Prasad et al. (1985) for Darcy regime.

non-Darcian regime, also using Forcheimmer and Brinkmann models. It is seen that without convective or non-linear drag terms, Nu shows a great match with the results from Brinkmann and Forcheimmer models presented by Lauriat and Prasad (1989). When the convective and porosity effects are implemented, at high Ra^*, the Nu results differ from Lauriat and Prasad (1989) (see Figure 2.5).

In the present thesis, the focus will majorly be placed on the Darcian regime and how external flow over it changes the features seen by Hewitt et al. (2012) and Otero et al. (2004).

2.4 Heat transfer characteristics due to turbulent flow over porous media

Before delving into convection in a turbulent flow regime over a porous media, it is important to understand the physical mechanisms governing turbulent flow over porous media itself. Turbulent flow through a porous medium is mainly governed by the bulk Reynolds number given by:

$$\boxed{Re_b = \frac{U_b H}{\nu}}. \tag{2.4.1}$$

Flow over porous wall layers has been a topic of interest because of the vast spectrum of fascinating underlying physics that governs such flows, in particular at the transition between the open flow region and the porous region. Breugem and Boersma (2005) investigated the properties of turbulent flow over a porous media by performing DNS in a channel with porous media using two approaches - the continuum approach (the Volume-Averaged Navier Stokes equations are solved) and the direct approach (Direct Numerical Simulation using Immersed Boundary Method) and a control case with DNS for a channel flow with solid walls. The continuum approach is outside the purview of this thesis and will be discussed in an additional section. For the DNS with Immersed Boundary method, Breugem and Boersma (2005) adopted a geometrical domain of $30 \times 20 \times 9 = 5400$ cubes with porosity $\phi = 0.875$ (as the pore size d_p equals the cube size d_f). The permeability value was obtained by comparison between theoretical and computational models in the laminar regime. Following that, the Darcy number was calculated as $Da = \frac{K}{H^2} = 3.4 \times 10^{-4}$ where K is the permeability of the grid of cubes. It is important to note from the study by Breugem and Boersma (2005) that the effects of bulk flow, friction velocity at the top and permeable wall, permeability and roughness are all characterised by subsequent Reynolds numbers. The bulk Re_b characterizes the flow in the bulk region of the domain or the clear channel region, whereas the friction Reynolds number is effectively a measure of the turbulence intensity at the permeable and top walls. The permeability Reynolds number decides the relative importance of using $\sqrt{K_c}$, the square root of the permeability at the interface to the viscous length scale. On the other hand, the roughness Reynolds number deals with assessing the dominance of the size of the roughness element with the viscous wall unit, inherently judging the effect of a roughness layer on the flow. It is interesting

to note here that in the present simulations, Breugem et al. (2006) modelled the geometry of the porous medium in a way such that Re_d is kept low while Re_K is sufficiently large to study effect of changing permeability on the flow.

Figure 2.6 shows the profile of volume, Reynolds and phase averaged horizontal velocity $\langle\overline{u}\rangle^s$ normalized by bulk velocity U_b and it is seen that the maximum is reached near the solid top wall for the porous media cases. Also, this shows that there is larger skin friction at the permeable wall.

$Re_b = \frac{U_b H}{\nu}$	$Re_\tau^p = \frac{u_\tau^p H}{\nu}$	$Re_\tau^t = \frac{u_\tau^t H}{\nu}$	$Re_K = \frac{u_\tau^p \sqrt{K_c}}{\nu}$	$Re_d = \frac{u_\tau^p d_p}{\nu}$
5500	669	394	12.4	33.4

Table 2.1: Reynolds numbers and their values used by Breugem and Boersma (2005).

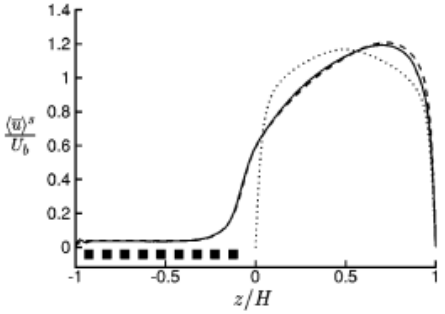

Figure 2.6: Reynolds and volume average streamwise velocity normalized by bulk velocity U_b for DNS with cubes (—); DNS with continuum (- - -) and DNS with solid walls (...) (Breugem and Boersma (2005)).

The volume-averaged rms velocity profiles for streamwise direction, normalized by u_τ^p for DNS with cubes (see Figure 2.7), compared with the case where DNS is done for flow between two solid walls shows that in case of solid walls, the peak is higher as it is associated with low and high-speed streaks in the near-wall region. However, in the case of permeable walls, due to the weak wall-blocking effect, streaks are not created. Rather, large vortical structures are seen near the permeable wall which is also proved in a further study by (Breugem et al. (2006)). They showed that these vortical structures are due to Kelvin-Helmholtz instabilities originating from an inflection point in the mean velocity profile near the fluid/porous interface.

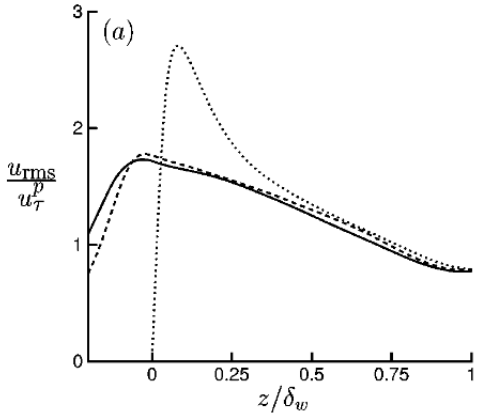

Figure 2.7: Root mean square streamwise horizontal velocity for DNS with cubes (—); DNS with continuum (- - -) and DNS with solid walls (...) (Breugem and Boersma (2005)).

Chandesris et al. (2013) extended the work by Breugem et al. (2006); Breugem and Boersma (2005) to include the effects of heat transfer when there is flow over porous media. They neglected the effect of buoyancy in their simulations i.e. essentially the Bousinessq term in the wall-normal

momentum equation is negligible ($Ra{\cdot}Pr << 1$ and the term was neglected in the governing Navier-Stokes equations). The authors pointed out the difference in time scales for thermal diffusion in the porous region (scaled by $\frac{H^2}{\alpha}$) and turbulent momentum diffusion in a free channel (scaled by $\frac{H}{u_\tau^p}$) and showed that it is of the order $Re_\tau^p Pr$. They used a fluid of $Pr = 0.1$ and $Re_b = 5500$ to bring down this ratio to around 60. They further investigated three cases by varying the temperature boundary conditions at the domain walls and the porous cube surfaces. The three cases are, as shown in Figure 2.8, are:

- Cube surfaces are adiabatic; constant temperature at the top and bottom wall. ($T_{topwall} > T_{bottomwall}$)
- Cube surfaces are adiabatic; constant heat flux at the top and bottom wall.
- Incoming heat flux on cube surfaces; constant heat flux at top and bottom wall.

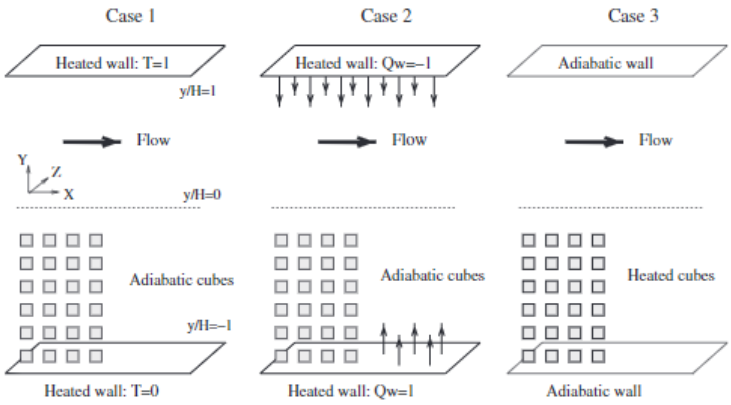

Figure 2.8: Schematic of the three cases investigated by Chandesris et al. (2013).

The root-mean-square temperature profiles were analysed for the 3 cases (see Figure 2.9). The local peak for case 1 and case 2 were near the top wall but for case 3, it is seen that the peak is inside the porous matrix. The author explains that this is seemingly surprising as the flow deep inside the porous matrix is laminar. The reasoning behind this can be traced back to the fact that the cubes in the porous matrix filter out the small-scale fluctuations of velocity, and the large-scale fluctuations penetrate the matrix which ultimately gives rise to high-temperature fluctuations. But

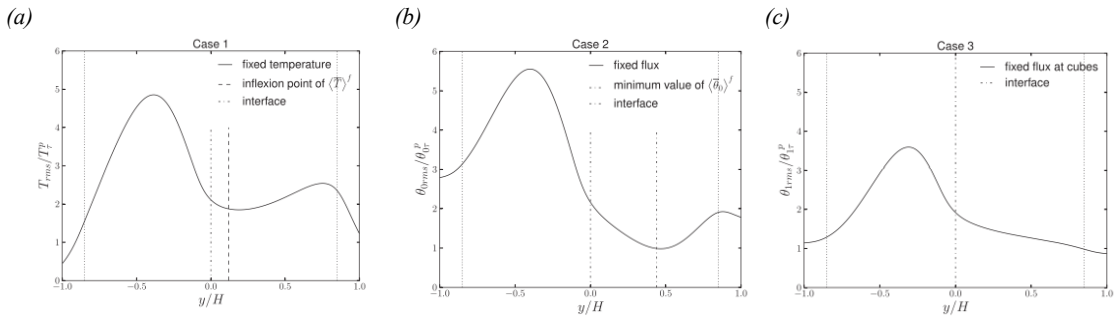

Figure 2.9: Volume averaged rms temperature profiles for the three cases.(Chandesris et al. (2013))

the interesting point in this reasoning is that this is not caused by turbulence, but due to pressure waves. This fact is also proved in the study by Breugem and Boersma (2005), where it is shown that the subfilter scale pressure has almost negligible contribution to the rms pressure and it is majorly dominated by large scale fluctuations, as seen in Figure 2.10.

Chandesris et al. (2013) further derived and verified a macroscopic turbulent diffusivity hy-

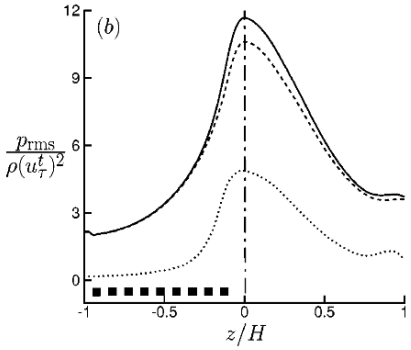

Figure 2.10: Volume averaged RMS pressure (—) with respective contribution from large scale (- - -) and small scale fluctuations (...). (Breugem and Boersma (2005)).

pothesis. The turbulent thermal diffusivity is defined by :

$$\alpha_{t_\phi} = \frac{-\langle\overline{v'T'}\rangle^f}{\partial\langle\overline{T}\rangle^f/\partial y} \tag{2.4.2}$$

It is seen that this diffusivity factor for all 3 cases decreases in the porous matrix and reduces to a value close to zero deep into the matrix. This in turn proves the reasoning stated above that even though large-scale fluctuations can penetrate the matrix, there is no turbulent mixing present.

2.5 Convection in porous media in the presence of external flow

The physics when mixed convection is coupled with turbulent flow over a porous media is governed by a dimensionless number known as the bulk Richardson number Ri_b which is the ratio of buoyancy to shear production in the bulk of flow. Ri_b can be expressed as:

$$\boxed{Ri_b = \frac{Ra}{Re_b^2 Pr} = \frac{\alpha(T - T_{ref})gH}{U_b^2}}, \tag{2.5.1}$$

where Re_b is the bulk velocity of the flow. (Note: The Re prescribed for Rayleigh-Bénard convection is based on the convective velocity scaling and is obtained as an output parameter. When the simulation changes to having a turbulent flow along with mixed convection, Re_b is used as an input parameter. The velocity in this case is the bulk velocity in the clear region).

The literature on the physics of mixed convection in porous media is not widespread. Iida and Kasagi (1997) carried out DNS simulations of mixed convection in turbulent channels at low $Ri_b < 0.3$. The authors observed interestingly that heat transfer increases steadily with increasing Ri_b, but the increase in C_f is non-monotonic - it decreases till $Ri_b = 0.05$ and then increases. Sid et al. (2015) studied DNS results for simulations till $Ri_b = 1$ and confirmed the non-monotonic trend. They also observed significant deviation in mean velocity and temperature profiles when buoyancy starts dominating, from the shear-driven cases. They also showed the Reynolds analogy breaks down and the turbulent Prandtl number is not uniform due to the effects of buoyancy. Pirozzoli et al. (2017) studied the same problem and conducted numerical studies over a vast parametric space ranging from $Ri_b = 0$ to $Ri_b = \infty$, whilst varying both Reynolds and Rayleigh number. Their results showed that the flow statistics for forced convection are almost fully interpretable, but for free convection, there are results which demand more clarity. They also found that vertical velocity and temperature fluctuation characteristics conform more to pre-established models, which show vertical motions are controlled by thermal plumes.

Chu et al. (2019) performed DNS of turbulent flow over staggered cylindrical porous media. The authors found out that increasing Re shows higher Nu and pressure drop, but St/C_f shows pressure drop increases faster as Re increases (C_f is the skin friction coefficient which quantifies the skin shear stress by non-dimensionalizing it using dynamic pressure. St is the Stanton number

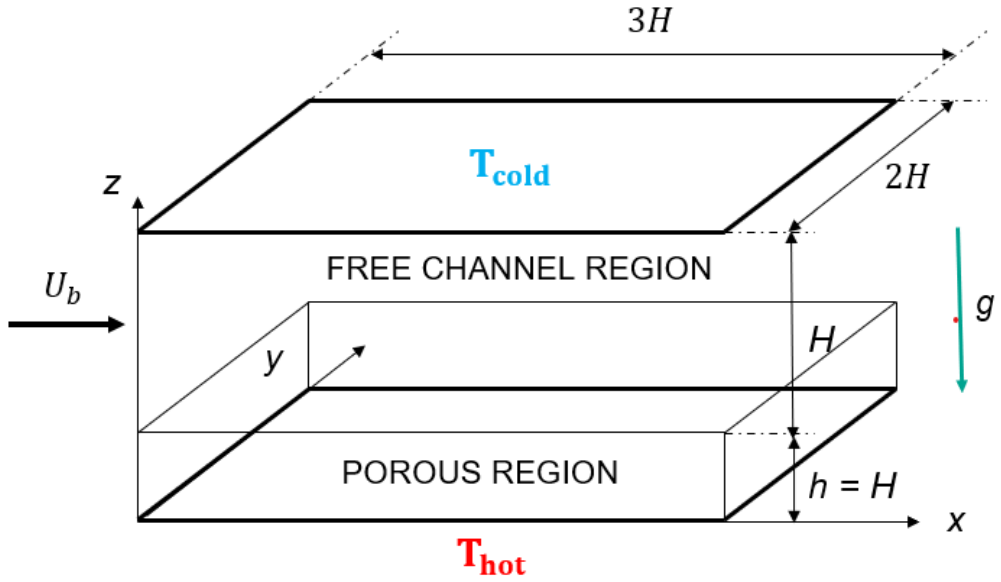

Figure 2.11: Schematic to represent the present simulation setup where the channel is divided into porous and free channel regions. Mixed convection is enforced, along with a turbulent flow over the porous wall layer.

which is the ratio of heat transferred to the fluid to the thermal capacity of the fluid). Very recently, Schäfer et al. (2022) studied turbulent flow over heterogenous ribbed surfaces modelling surface roughness at varying bulk Richarson numbers. Regimes were identified for convection roll-to-cell transitions based on varying Ri_b and also it was seen that the rib spacing affected the dynamics of the convection rolls. It must also be taken into notice that Chu et al. (2019) studied temperature as a passive scalar, without coupling buoyancy whereas Schäfer et al. (2022) studied buoyancy force-driven convection (Ri_b is non-zero). The present thesis will focus on a very similar problem considering non-zero Richardson number (thermally-driven buoyancy is accounted for), with the flow being over porous media instead of ribbed surfaces (a simplified schematic is presented in Figure 2.11).

The final part of this thesis will deal with the Monin-Obukhov scaling, which provides a single length scale to differentiate between shear-dominated and buoyancy-dominated regions, given by:

$$L = \frac{u_\tau^3}{\alpha g Q}, \tag{2.5.2}$$

where u_τ is the wall friction velocity, g is the acceleration due to gravity and Q is the wall heat-flux normalized by ρc_p. It is uncommon in literature where MO similarity has been used for unstable stratification in channels. Its most common usage is for the analysis of atmospheric boundary layers, where it is used to estimate heat flux and shear stress from mean temperature and velocity gradients.

Before delving into the research goal itself, it is necessary to identify the dimensionless parameters governing flow physics using dimensionless analysis. A section later is also dedicated to the derivation of the ratio of thermal diffusion timescales between turbulent flow and flow inside porous media.

2.5.1 Timescale ratios arising in turbulent flow over porous media in the presence of convection

One of the major points of concern while analysing the physics of convection in porous media with turbulent external flow, is the difference in the timescales between the turbulent momentum

transfer and the thermal transport in the porous media.
In convective turbulence, the characteristic velocity scale for outer region can be given by (Nieuwstadt et al. (2016)):

$$w^* = \left(\alpha g H \overline{w'T'}\right)^{\frac{1}{3}}, \tag{2.5.3}$$

where $\alpha = \frac{1}{T_{ref}}$ for ideal gases and H is the clear-fluid layer height.
So the turbulent thermal diffusion timescale can be derived as:

$$t^*_{turb} = \left(\frac{H^2 T_{ref}}{g\overline{w'T'}}\right)^{\frac{1}{3}}. \tag{2.5.4}$$

Now the Nusselt number Nu can be written as:

$$Nu = \frac{\overline{w'T'}H}{\Delta T \kappa_f}, \tag{2.5.5}$$

assuming that in the core region of the turbulent clear-fluid layer thermal conduction is neglected. which gives:

$$\overline{w'T'} = \frac{Nu \Delta T \kappa_f}{H}. \tag{2.5.6}$$

Substituting $\overline{w'T'}$ in the timescale we get:

$$t^*_{turb} = \left(\frac{H^3}{\alpha Nu \Delta T \kappa_f g}\right)^{\frac{1}{3}}. \tag{2.5.7}$$

The timescale for thermal diffusion inside the porous media is given by:

$$t^*_{porous} = \frac{h^2}{\kappa_{eff}}, \tag{2.5.8}$$

where κ_{eff} is the macroscopic effective thermal diffusivity in the porous layer. The ratio between these two timescales can thus be expressed as:

$$\frac{t^*_{porous}}{t^*_{turb}} = \frac{h^2}{\kappa_{eff}} \left(Nu\ \alpha\ \Delta T \kappa_f\ g\right)^{\frac{1}{3}} \frac{1}{H}, \tag{2.5.9}$$

which can be rewritten as:

$$\frac{t^*_{porous}}{t^*_{turb}} = \left(\frac{h}{H}\right)^2 \left(\frac{\kappa_f}{\kappa_{eff}}\right) \left(\frac{\alpha \Delta T H^3 g}{\kappa_f \nu_f} \frac{\nu_f}{\kappa_f}\right)^{\frac{1}{3}} Nu^{\frac{1}{3}}. \tag{2.5.10}$$

It can be rearranged to produce:

$$\frac{t^*_{porous}}{t^*_{turb}} = (RaPr)^{\frac{1}{3}} Nu^{\frac{1}{3}} \left(\frac{h}{H}\right)^2 \left(\frac{\kappa_f}{\kappa_{eff}}\right), \tag{2.5.11}$$

and the Nu can further be decomposed as a $f(Ra, Pr)$ from Table 2.2. Now, κ/κ_{eff} is of order 1, Pr is of order 1 and both Nu and Ra are of order much higher than 1. Therefore $\frac{t^*_{porous}}{t^*_{turb}} >> 1$, which proves that there is, indeed, a major disparity in the two timescales.

2.5.2 Numerical methods

Having defined the problem and the complicated physics that entails it, it is necessary to have numerical methods which can successfully simulate such flow physics, without compromising on computational cost. This section is divided into three sections: In the first section, the focus is briefly placed on the finite-difference DNS solver, followed by a discussion on the immersed boundary methods being used.

Direct numerical simulations will be implemented in the present thesis to solve the problem. DNS has been an effective tool for the past few decades, because unlike Reynolds-averaged methods or Large Eddy simulations, DNS resolves all the scales in a flow situation ranging from the macrostructure to the microstructure. Since it is important in the present thesis to study the flow properties at the smallest scales, especially inside the porous wall layer, DNS will be the most effective tool possible to carry out the simulations. Also, the work by Chandesris et al. (2013) does not couple the thermal transport to the momentum equation and solves the temperature field by treating it as a passive scalar. The present thesis aims to couple the thermal energy to momentum equation and DNS will be instrumental in providing accurate solutions to such coupled problems. The starting point for the present work is the CaNS code developed by Costa (2018). CaNS is a finite-difference solver for massively parallel DNS of incompressible flows. The present work will extend the solver to include buoyancy effects using the above-mentioned Boussinesq approximation, and an immersed-boundary method for the porous medium.

Immersed boundary methods allow for simulating the flow simulate flow over obstacles very efficiently when compared to standard approaches based on body-fitted grids. In a nutshell, this method adds an extra force term in the momentum equation, which allows for mimicking no-slip and no-penetration boundary conditions with satisfactory accuracy, while retaining the efficiency of the Navier-Stokes solver. Several methods have been identified to formulate the forcing term over the last few decades. Since Peskin (1972) first explored forcing in terms of regularized Dirac delta functions, this approach has been adopted by many works, and extended in numerous flavours, such as the works of Uhlmann (2005); Griffith and Patankar (2020)), and many more. Indeed, immersed-boundary methods have a much bigger advantage over conformal grids in terms of computational efficiency, as there is much less communication per grid point (Verzicco (2023)).

In the present thesis, we will consider one of two possible IBM methods – the volume penalisation method and the stress IBM method. The volume penalisation method was formulated by Kajishima et al. (2001) who used it to simulate spherical particles in turbulent channel flow. In this method, the boundary conditions are imposed on the solid-fluid interface in a way such that the fluid velocity near the interface is penalised by the solid velocity. This method will be instrumental in simulating the porous media in the present thesis and along with isotropic, anisotropic porous media flows can also be attempted.

The stress IBM was formulated in the paper by Breugem and Boersma (2005). The main advantage here is that it is highly accurate – for geometries that can conform to the underlying grid, this IBM ensures that there is an exact formulation of the no-slip boundary condition at the interfaces. However, this method cannot be extended to the case of anisotropic porous media composed of more irregular pores.

Finally, a one-fluid formulation will be used for solving the transport of thermal energy within the porous medium, as described in Ardekani et al. (2018).

Lastly, it is seen in section 2.5, that there is a huge disparity between the thermal diffusion timescales for turbulent flow and inside the porous media. This makes the simulation computationally inefficient and it becomes very difficult to test the setup with finer resolution. This leads to the temperature field convergence increasingly difficult, as is explained in later sections.

2.6 Summary of literature review

The literature review presented above gives an elaborate overview of the various facets of the thesis problem statement. It is shown that the literature describing Rayleigh-Bénard convection is extensive, and a summary of the $Nu - Ra$ scaling has been presented. The review covers the literature regarding convection in the presence of a porous layer and also when there is a turbulent flow over a porous layer without convection. Finally, it is shown that despite the literature being extensive for the cases described above, when there is turbulent flow along with mixed convection over a porous wall layer, the literature becomes scarce and inconclusive as far as the physics is concerned.

3

Research goals and Scope

"The general focal point in the present thesis is to solve the Navier-Stokes equations for thermal convection under the Oberbeck-Bounssinesq approximation, to study mixed convection with turbulent flow over a porous layer. The ultimate goal is to understand and draw inferences on how this thermal coupling with buoyancy affects momentum and heat transfer characteristics, particularly in the fluid/porous interface region."

The plan is to vary the bulk Richardson number Ri_b, which is essentially a ratio of buoyancy dominance to shear dominance. From another point of view, the Rayleigh number Ra can be derived as a function of Ri_b,Re_b and Pr, given by $Ra = Ri_b Re_b^2 Pr$. The Re_b is fixed at 5500 and Pr is set at 0.1. The plan is to vary Ri_b from 0 till about $\mathcal{O}(10)$. When Ri_b is zero, it indicates that the buoyancy force is zero and thus even the Ra is zero. The flow is entirely shear dominated with forced convection prevailing. At $Ri_b \sim 1$, the buoyancy and shear forcing are of the same order as the $Ra \sim 3 \times 10^6$. This Ra according to the literature described above will be a transition regime to turbulent RB convection and plumes start shedding from the walls. Also in the porous layer, the Ra^* (Rayleigh-Darcy number) is too low to trigger columnar convective structures(Lapwood (1948)), considering the $Da = 3.4 \times 10^{-4}$ used by Breugem and Boersma (2005). Thus convective thermal layers are expected to be seen in the porous layers. It will also be interesting to see how the external bulk flow alters these phenomena in both regions. At about $Ri_b \sim \mathcal{O}(10)$, the buoyancy production dominates over the shear production. The Ra can be calculated to be around $\mathcal{O}(3 \times 10^7)$, so turbulent RB convection completely sets in inside the clear-fluid region with the plume structures decreasing in spatial scales. $Ra^* \sim 10^4$, which is higher than 1300 and columnar thermal structures appear in the porous wall layer.

It is important to compare and check the $Nu - Ra$ scalings when Ri_b is varied, with the cases of classical RB convection and convection in a porous layer. A scaling of 1/4 is seen for RB convection. When convection starts in the porous layer, a linear scaling for $Nu - Ra$ is seen. Thus, the $Nu - Ra$ for the present case might lie between a 1/4 and 1 scaling, but how the external forced convection will alter this is yet to be unravelled. If a higher Ri_B is examined, the shear production will be almost negligible and the Ra increases too. Plume shedding is expected to increase from the solid top wall as the turbulence in the free region will increase much more. It will be interesting to examine how plume shedding starts at the transition region and how they interact with the convective rolls being formed inside the porous layer. Also, it might be seen that plumes are not at all formed at the transition region, rather convective rolls, corresponding to vortices as seen by Breugem and Boersma (2005) in case of a turbulent flow, are seen. At even higher Ri_b, if the Ra^* crosses 1300, columnar convective structures in the porous media will be

formed. How these columnar structures give way to the vigorous plume shedding (or convective rolls) in the clear region, with the external flow acting on these structures, can prove to be a topic with rich underlying physics.

The scope of the present thesis is limited to keeping the kinematic viscosity, density and specific heat capacity constant with the fluid being incompressible. Also viscous heating is neglected in the energy equation. This simulation, with such parameters and subsequent settings, will thus be instrumental in solving the critical problem statement which is being addressed in this thesis.

4

Methods

The present thesis aims at exploring the momentum and heat transfer characteristics when mixed convection occurs in the presence of a turbulent flow over a porous wall layer. The Navier-Stokes equation is solved for the incompressible fluid phase and the Oberbeck-Boussinesq approximation is implemented to model buoyancy-driven convection. The Immersed Boundary Method with a volume penalization approach (Kajishima et al. (2001)) is implemented to simulate the porous wall layer. These modified equations are solved using a finite-difference solver CaNS using a 3rd-order Runge-Kutta temporal discretization scheme.

4.1 Governing Equation

The principle equations governing the incompressible fluid phase are the continuity equation and Navier-Stokes equation, given as:

$$\nabla \cdot \mathbf{u} = 0, \tag{4.1.1}$$

$$\rho_f \frac{\partial \mathbf{u}}{\partial t} + \rho_f \nabla \cdot \mathbf{uu} = -\nabla p + \eta_f \nabla^2 \mathbf{u} + \rho_f \mathbf{f}, \tag{4.1.2}$$

where $\mathbf{u}$ is the fluid phase velocity, p is the pressure, ρ_f is the fluid phase velocity, η_f is the dynamic viscosity of fluid phase and $\mathbf{f}$ is the body force.

In the present work, the Navier-Stokes equations are modified to include the Bousinessq approximation term to model buoyancy (provided density variations are small, and constant in the present work). The Bousinessq approximation related the fluid phase density ρ_f with temperature as: $\rho = \rho_0(1 - \alpha(T - T_{ref}))$, where α is the volumetric coefficient of thermal expansion. Further, the Immersed Boundary Method forcing term to model the solid phase is also included in the momentum equation. The modified Navier-Stokes equation is given as:

$$\nabla \cdot \mathbf{u} = 0, \tag{4.1.3}$$

$$\rho_f \frac{\partial \mathbf{u}}{\partial t} + \rho_f \nabla \cdot \mathbf{uu} = -\nabla p + \eta_f \nabla^2 \mathbf{u} + \rho_f \mathbf{g}\alpha(T - T_{ref}) + f_{IBM}, \tag{4.1.4}$$

where f_{IBM} denotes the volume penalization forcing term. Further, for the heat transfer analysis, the energy equation is solved for the entire domain, given as:

$$\rho c_p \frac{\partial T}{\partial t} + \rho c_p \nabla \cdot \mathbf{u}T = \nabla^2 (k_{eff} T). \tag{4.1.5}$$

The effective heat capacity and effective thermal conductivities are given by :

$$\rho c_p = \psi \rho c_p|_s + (1-\psi)\rho c_p|_l; \tag{4.1.6}$$

$$k_{eff} = \psi k_s + (1-\psi)k_l, \tag{4.1.7}$$

where $\psi(\mathbf{x})$ is the phase indicator function such that:

$$\psi(\mathbf{x}) = \begin{cases} 1, & \text{if } \mathbf{x} \in \text{solid} \\ 0, & \text{if } \mathbf{x} \in \text{fluid} \end{cases}$$

where $\mathbf{x}$ represents the location of a grid cell in the computational domain. $\rho c_p|_l$ denotes heat capacity of fluid, $\rho c_p|_s$ denotes heat capacity of solid, k_l denotes thermal conductivity of fluid and k_s is thermal capacity of solid.

4.2 Numerical Method

The above-defined equations are solved using a low-storage explicit, 3-step Runge-Kutta scheme for discretization of the terms. A structured Cartesian grid is employed, which is uniformly spaced in two directions (x and y direction in the present case) and a stretched grid. Second-order finite difference schemes are used to discretize the equations spatially with a staggered arrangement of grid points (pressure p at grid centres and velocities u_i at grid faces). A pressure-correction method is adopted to couple the continuity equation to the Navier-Stokes equations and subsequently, the energy equation is solved in the end. The RK-3 time-stepping equations at every substep k (k = 1,2,3; $k = 1$ corresponds to previous timestep n and $k = 3$ corresponds to new timestep $n+1$) is given as:

$$\mathbf{u}^* = \mathbf{u^k} + \Delta t(\alpha_k \mathbf{RHS}^k + \beta_k \mathbf{RHS}^{k-1} - \gamma_k \nabla p^{k-\frac{1}{2}} + \gamma_k \mathbf{RHSB}^k), \tag{4.2.1}$$

$$\mathbf{u}^{**} = \mathbf{u}^* + \Delta t f_{IBM}, \tag{4.2.2}$$

$$\nabla^2 \Phi = \frac{\nabla \cdot \mathbf{u}^{**}}{\gamma_k \Delta t}, \tag{4.2.3}$$

$$\mathbf{u^{k+1}} = \mathbf{u}^{**} - \gamma_k \Delta t \nabla \Phi, \tag{4.2.4}$$

$$p^{k+\frac{1}{2}} = p^{k-\frac{1}{2}} + \Phi, \tag{4.2.5}$$

$$T^{k+1} = T^k + \Delta t(\alpha_k \mathbf{RHSE}^k + \beta_k \mathbf{RHSE}^{k-1}). \tag{4.2.6}$$

Here

$$\mathbf{RHS} = -\nabla \cdot \mathbf{uu} + \nu_f \nabla^2 \mathbf{u}, \tag{4.2.7}$$

$$\mathbf{RHSB} = \mathbf{g}\alpha \Delta T, \tag{4.2.8}$$

and

$$\mathbf{RHSE} = -\nabla \cdot \mathbf{u}T + \nabla^2(\kappa_{eff} T), \tag{4.2.9}$$

The constants are given by: $\alpha_1 = \frac{32}{60}$, $\beta_1 = 0$, $\alpha_2 = \frac{25}{60}$, $\beta_2 = -\frac{17}{60}$, $\alpha_3 = \frac{45}{60}$ and $\beta_3 = -\frac{25}{60}$. γ_k is expressed as $\alpha_k + \beta_k$. The first prediction velocity u^* is calculated by making use of present and previous timesteps. Then this prediction velocity is used to calculate the IBM forcing term, which will be elaborated upon in the following section. A second prediction velocity u^{**} is determined by including the IBM forcing term f_{IBM}, following which the correction pressure Φ is calculated by solving a Poisson equation. A fast FFT-based solver is used to solve the Poisson equation, provided the grid-spacing in two directions (x and y in this case) are constant and the boundary conditions are homogenous. The constant coefficient Poisson equation takes the form of a tridiagonal matrix, which is solved effectively by the Gauss elimination method. The velocity at new timestep level $n+1$ is obtained by correcting the second prediction velocity u^{**} using the corrected pressure.

4.3 Immersed Boundary Method

The Immersed Boundary Method used in the present work is the volume-penalization method (Kajishima et al. (2001)) where essentially the velocity inside the dispersed phase (solid phase in this case) is achieved by penalizing the continuous phase velocity in the position of the dispersed phase. The velocity of such a system where a solid is suspended in fluid, can be defined as:

$$\mathbf{u} = (1 - \phi)\mathbf{u}_f + \phi\mathbf{u}_s \tag{4.3.1}$$

where ϕ is the fraction of solid in the computational cell, $\mathbf{u}_f$ is the fluid velocity and $\mathbf{u}_s$ is the solid velocity. In the present case, the solid phase is stationary and so $\mathbf{u}_s = 0$.

In section 4.2, it is shown that the second prediction velocity $\mathbf{u}^{**}$ is calculated by including the IBM forcing. It will now be elaborated upon on how f_{IBM} is derived. The second prediction velocity can be written as velocity defined in 4.3.1, which gives the equation as:

$$(1 - \psi)\mathbf{u}_f + \psi\mathbf{u}_s = \mathbf{u}^* + \Delta t f_{IBM} \tag{4.3.2}$$

$$(1 - \psi)\mathbf{u}_f - \mathbf{u}_f = \Delta t f_{IBM} \tag{4.3.3}$$

$$\Delta t f_{IBM} = \cancel{\mathbf{u}_f} - \psi\mathbf{u}_f - \cancel{\mathbf{u}_f} \tag{4.3.4}$$

$$f_{IBM} = \frac{-\psi\mathbf{u}_f}{\Delta t}. \tag{4.3.5}$$

This ensures that when $\psi = 1$, $\mathbf{u}^{**} = \mathbf{u}_s$ and when $\psi = 0$, f_{IBM} equals 0, which ensures that no penalization is necessary. The next question that arises is that which timestep should the IBM forcing correspond to. Ideally, the forcing term for IBM should be calculated from the u^{n+1}. But in that case, conserving mass becomes difficult in the domain. So a compromise is made by using u^* as a proxy for u^{n+1} and the forcing term is calculated from u^*.

4.3.1 Formulation of ψ field for model inspired from Breugem and Boersma (2005)

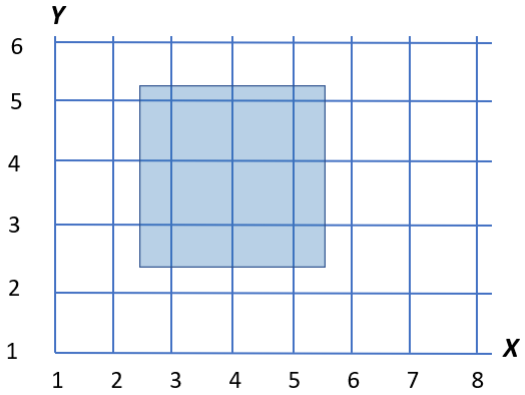

Figure 4.1: Schematic showing cube placement in a uniform Cartesian grid.

Before the Immersed Boundary forcing is calculated, it is important to determine the solid volume fraction field ψ. An algorithm is devised to calculate the solid volume fraction field for 5400 cubes with 30 in x direction, 20 in y direction and 9 in z direction as modelled in Breugem and Boersma (2005), given by: Line fractions are calculated in 3 directions (x, y and z), which are multiplied to calculate the volume fraction. The fraction varies from 0 in the fluid to 1 in the solid. To calculate the line fraction, the centres of the cubes are calculated. Following that, the position of the start and end of the cube is calculated based on the cube dimensions. The x, y or z cell with the start of the cube is calculated. If the start or the end falls between two cell faces, the modulus of the start or end position with the x, y or z coordinate before that position is calculated, which denotes the line fraction of solid in that cell. Having calculated the line fraction in the cells with

the starting and end of the cube, the cells lying inside the cube are assigned a value of 1. In figure 4.1, the starting of the cube lies in the $2nd$ grid cell and the ending is in the $5th$ grid cell. So the modulus value gives the solid fraction in $2nd$ and $5th$ cells. $3rd$ and $4th$ cells are assigned a line fraction of 1. Ultimately the ψ field is calculated by multiplying all three line fractions.

5

Validation

The present thesis breaks down the problem of analysing mixed convection with turbulent flow over a porous wall layer into several stages. The first stage is to validate the fundamental buoyancy-driven convection which is done by modelling a differentially heated cavity. Following that, Rayleigh-Bénard convection is analysed and the passive scalar quantities like temperature are validated. The Immersed Boundary Method implemented is validating it against a dataset for the drag of cubes at varying Reynolds numbers. Finally, the momentum and passive scalar heat transfer characteristics are validated on the model inspired from Breugem and Boersma (2005). After these successful validations, the results section focuses on the effects of adding natural convection to the pre-existing work and analyses it at varying Ri_b.

5.1 Buoyancy-driven convection

Buoyancy-driven convection is modelled in a differentially heated cavity, based on Le Quéré (1991). Le Quéré (1991) simulated the flow field inside a 2D square cavity with constant viscosity, where constant temperature boundary conditions were prescribed on the right and left vertical walls ($T_{left} > T_{right}$) to model differential heating, while the upper and lower walls were kept adiabatic. The direction of gravity is set to point vertically downwards ($-z$ direction). Ra is varied from 10^6 to 10^8, and the corresponding Nu is calculated across $x = 0$ and $x = 1/2$. In 5.1a,5.1b and 5.1c $x = 0, z = 0$ is the bottom left corner with the x axis extending towards the right and the z axis towards the top. The Nu is calculated as:

$$Nu_{x=x_0} = \int_0^1 \left(Ra^{0.5} u\theta - \frac{\partial \theta}{\partial x} \right) (x = x_0, z) dz, \tag{5.1.1}$$

where the temperature is normalized by the temperature difference between the hot and cold wall, and the velocity is non-dimensionalized by the convective velocity scaling. The present work validates the Nu values as shown in 5.1. The simulations are carried out in a uniform grid of 256×256. Since the total heat flux is expected to be constant across the domain, the Nu values should be the same across all the x planes, which is also seen in 5.1. Since the left wall is prescribed a higher temperature ($\theta = 0.5$), the fluid gets less denser and rises up whereas at the right wall with a lower temperature($\theta = -0.5$), the fluid gets heavier and sinks down. This forms a large-scale convective circulation inside the differentially heated cavity, as seen in Figure 5.1. This type of LSC is the most fundamental type of convective structure seen in natural convection. In the later parts of the thesis, it will be seen that more complex LSC structures can arise with changing flow

conditions and geometries.

Ra	$\mathbf{10^6}$	$\mathbf{10^7}$	$\mathbf{10^8}$
$Nu(x = 1/2, z)$ - Present Work	8.88	17	30.74
$Nu(x = 1/2, z)$ - Le Quéré (1991)	8.83	16.52	30.23
$Nu(x = 0, z)$ - Present Work	8.85	15.7	30.74
$Nu(x = 0, z)$ - Le Quéré (1991)	8.83	16.52	30.23

Table 5.1: Validation of Nu with Le Quéré (1991) across $z = 0$ and $z = 1/2$.

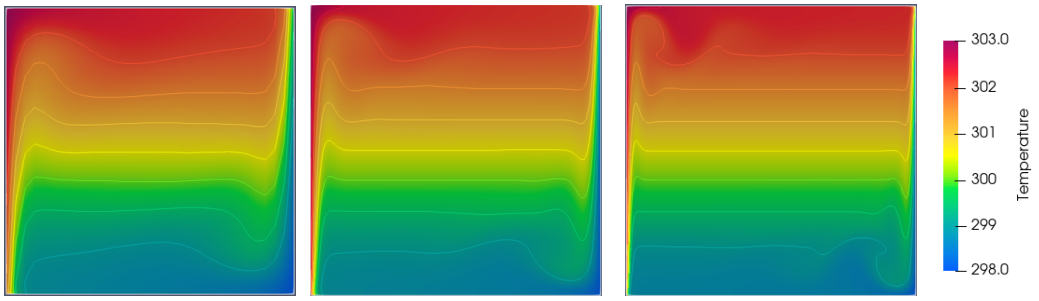

(a) (b) (c) (d)

Figure 5.1: Differentially heated cavity with left wall $(x = 0, z)$ at temperature 303K and right wall $(x = 1, z)$ at temperature 298K for (a) $Ra = 10^6$, (b) $Ra = 10^7$ and (c) $Ra = 10^8$.

5.2 Rayleigh-Bénard convection

Rayleigh-Bénard convection is a special case of buoyancy-driven convection where the temperature gradient is aligned with gravity. Before the porous media is implemented using IBM, it is important to validate if the present code can model natural convection. Mean and fluctuation passive scalar profiles are validated with the data from Kaczorowski and Wagner (2009). Although Kaczorowski and Wagner (2009) analysed RB convection inside a duct and in the present thesis, a channel will be considered, the momentum and thermal structures remain almost unaltered. Despite other sources of literature that have simulated RB convection inside channels, the work by Kaczorowski and Wagner (2009) showed a very interesting analysis of how boundary layer thickness changes and how the plumes spatially decrease in size with increasing Ra, so a choice was made to validate the mean and fluctuating temperature with their data. The domain size was prescribed as $1 \times 5 \times 1$ and after a grid convergence study, the mesh size was defined to be a $256 \times 512 \times 256$ uniform grid. 5.4 shows that with increasing Ra, the large convective roll structures seen for $Ra = 3.5 \times 10^5$ starts breaking up. Ultimately at $Ra = 2.31 \times 10^8$, the thermal rolls have completely broken up and given way to small thermal streaks, much smaller in spatial dimensions than the rolls seen at lower Ra. It would be interesting to see, how, in the presence of a porous wall layer and turbulent flow, these thermal plumes behave and if a similar pattern is observed for increasing Ra.

The mean and RMS temperature profiles have been validated with Kaczorowski and Wagner (2009) as shown in Figure 5.2. It is observed from the profiles that both in the mean and RMS profiles, there is evidence of the thermal boundary layer thickness decreasing with increasing Ra, which is also seen in Table 5.2. Nu is verified with that of Kaczorowski and Wagner (2009). As expected, it is seen that with increasing Ra, the Nu increases. Also, the $Nu \sim Ra^{0.25}$ is also seen in 5.3. This further shows that the model being simulated follows the Grossman-Lohse theory of Rayleigh-Bénard convection.

Ra	$\mathbf{3.5 \times 10^5}$	$\mathbf{3.5 \times 10^6}$	$\mathbf{3.5 \times 10^7}$	$\mathbf{2.31 \times 10^8}$
Nu - Present Work	6.27	12.16	22.76	40.26
Nu - Kaczorowski and Wagner (2009)	6.23	12.12	22.87	40.62
$\delta_\theta = 1/(2Nu)$	0.079	0.041	0.022	0.012

Table 5.2: Validation of Nu with Kaczorowski and Wagner (2009).

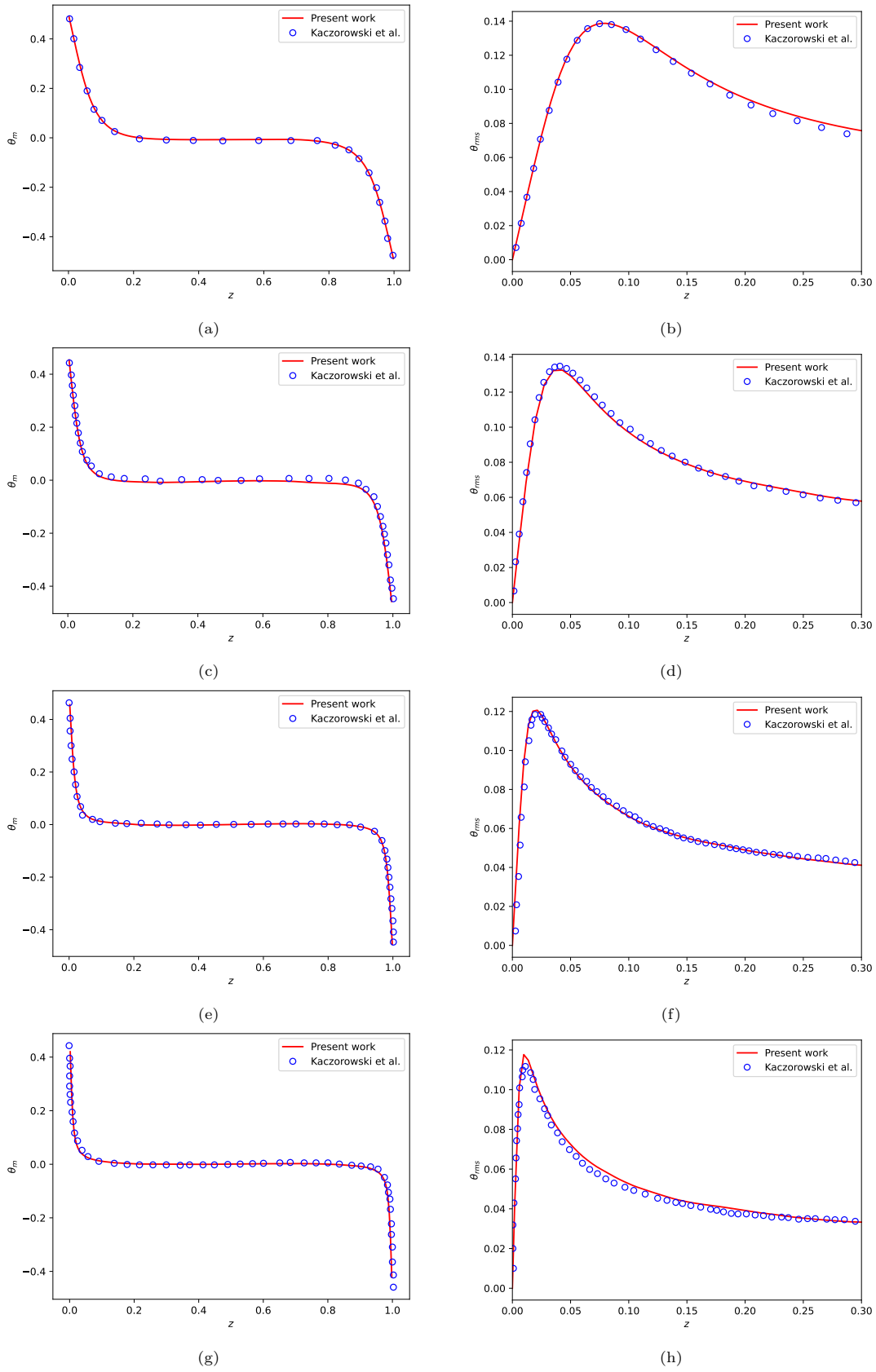

Figure 5.2: (a),(c),(e),(g) Mean temperature validation with Kaczorowski and Wagner (2009) for $Ra = 3.5 \times 10^5$, $Ra = 3.5 \times 10^6$, $Ra = 3.5 \times 10^7$ and $Ra = 2.31 \times 10^8$;(b),(d),(f),(h) Root mean squared temperature validation with Kaczorowski and Wagner (2009) for $Ra = 3.5 \times 10^5$, $Ra = 3.5 \times 10^6$, $Ra = 3.5 \times 10^7$ and $Ra = 2.31 \times 10^8$ till $z = 0.3$.

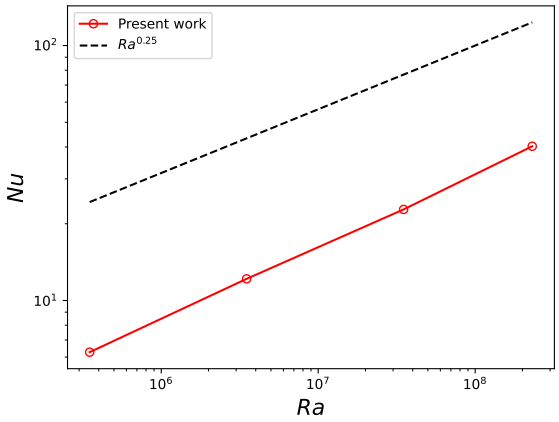

Figure 5.3: $Nu - Ra$ scaling for Rayleigh-Bénard convection.

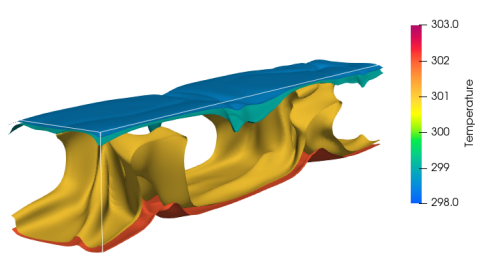

(a) Temperature contour for $Ra = 3.5 \times 10^5$.

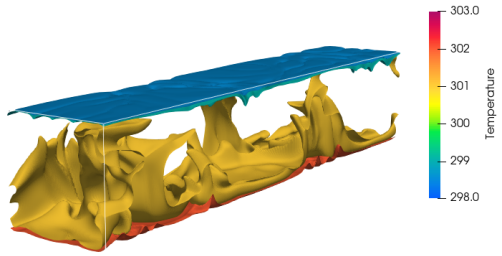

(b) Temperature contour for $Ra = 3.5 \times 10^6$.

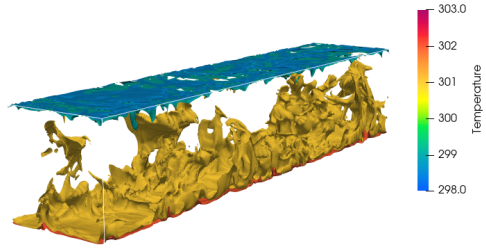

(c) Temperature contour for $Ra = 3.5 \times 10^7$.

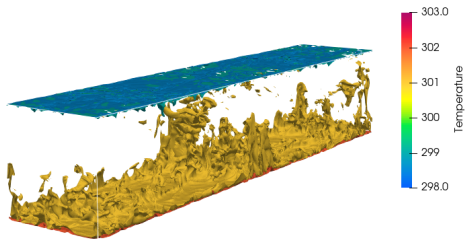

(d) Temperature contour for $Ra = 2.31 \times 10^8$.

Figure 5.4: Temperature contours for Rayleigh-Bénard convection for 4 Ra values, showcasing the transition of large-scale convective rolls to small scale thermal plumes. It is important to note the colourbar shows values from $298K$ to $303K$, which correspond to $\theta = -0.5$ to $\theta = 0.5$

5.3 Turbulent flow over a porous medium

Breugem and Boersma (2005) simulated turbulent flow over a porous media by using IBM which modelled 5400 cubes in an arrangement of $30 \times 20 \times 9$ distributed in the lower half of a channel with the upper half being a free channel. The number of mesh points used by the authors is $600 \times 400 \times 400$. Chandesris et al. (2013) extended the work to include the effects of temperature as a passive scalar (the Bousinessq term is neglected because $Ra \cdot Pr << 1$) and studied the heat transfer characteristics in addition to momentum. Before adding natural convection to that setup, which is the goal of the present work it is important to validate the pre-existing work. Thus the final stage of validation includes comparing the mean and RMS velocity, temperature and pressure data for turbulent flow over a porous media with that of Breugem and Boersma (2005) and Chandesris et al. (2013).

Breugem and Boersma (2005) calculated volume-averaged quantities by using a weighting function acting as a filter. A filter inherently filters out small-scale structures and only passes infor-

	$Re_b = \frac{U_b H}{\nu}$	$Re_\tau^p = \frac{u_\tau^p H}{\nu}$	$Re_\tau^t = \frac{u_\tau^t H}{\nu}$	$Re_K = \frac{u_\tau^p \sqrt{K_c}}{\nu}$	$Re_d = \frac{u_\tau^p d_p}{\nu}$
Breugem and Boersma (2005)	5500	669	394	12.4	33.4
Present work	5500	659	394	12.17	33

Table 5.3: Reynolds numbers and their values used by Breugem and Boersma (2005).

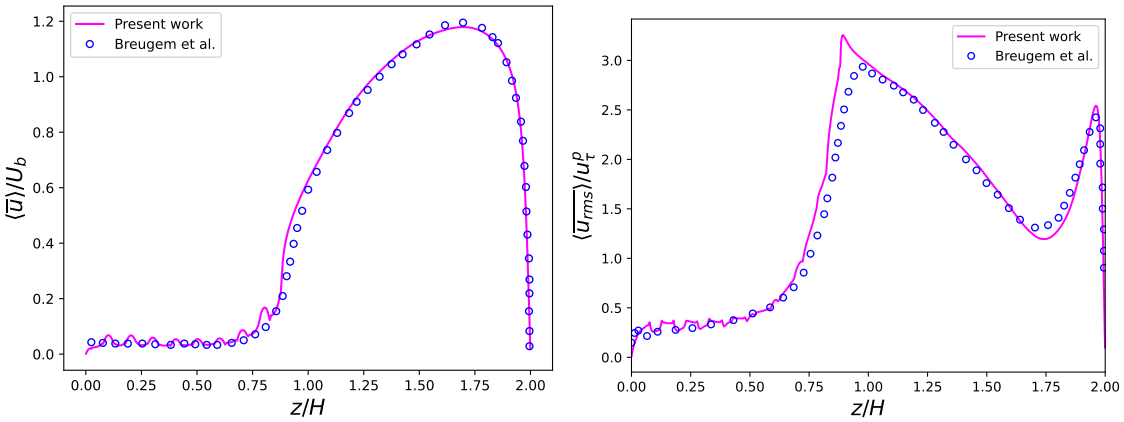

(a) (b)

Figure 5.5: (a) Validation of intrinsic, Reynolds averaged mean velocity normalized by bulk velocity U_b with superficial, volume averaged mean velocity data from Breugem and Boersma (2005); (b) Validation of intrinsic, Reynolds averaged mean velocity normalized by bulk velocity U_b with superficially, volume averaged mean velocity data from Breugem and Boersma (2005).

mation on large-scale structures. The condition for a weighting function to act as a filter is that it should satisfy the condition:

$$\int_V m(\mathbf{y}) dV = 1. \tag{5.3.1}$$

where $m(\mathbf{y})$ is the filter function. Further, the data was Reynolds-averaged and phase-averaged. In the present thesis, a filter is not applied, but rather just Reynolds-averaged and phase-averaged quantities. That is the reason in the porous region, the undulations in the data from the present work denote the fluid space inside the porous region, whereas in Breugem and Boersma (2005) the quantities are smoothened out in the porous region because of the weighting function. In Figure 5.5, the RMS profile validation shows that near the porous wall interface, there is some deviation where the fluctuations peak. This deviation can probably be attributed to Breugem and Boersma (2005) using a weighting function, as described above, which smoothens out the sharp interfaces. Similar reasoning can also be used to explain the deviation of the RMS temperature plots in Figure 5.6 near the boundaries.

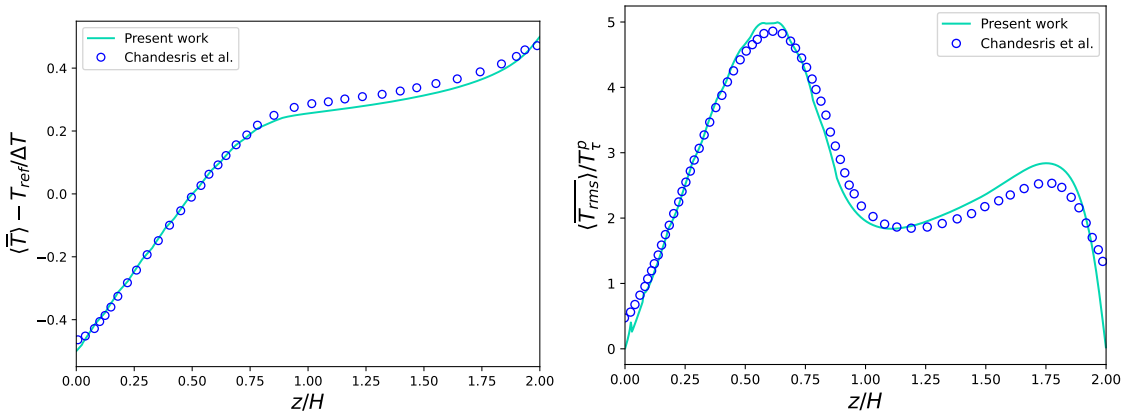

(a) Mean temperature validation.

(b) RMS temperature validation.

Figure 5.6: (a) Validation of intrinsic, Reynolds averaged mean temperature normalized by temperature difference ΔT with superficial, volume averaged mean temperature data from Chandesris et al. (2013); (b) Validation of intrinsic, Reynolds averaged root mean squared temperature normalized by friction temperature at permeable wall $T_\tau^p = Q/u_\tau^p$ with superficially, volume averaged mean velocity data from Chandesris et al. (2013).

6

Geometry, Mesh and Implementation

A crucial part of any computational fluid dynamics problem is the precise description of the geometry being used, the mesh being implemented and the parameters used to simulate the flow. The following sections deal with the reasoning behind the choice of geometry and the kind of mesh used. A section on parameter specification is also included where a dimensional analysis reveals the important non-dimensional parameters necessary for the problem analysis. Finally, the methods of averaging used to interpret the DNS data set have been discussed.

6.1 Geometry and boundary conditions

For the present thesis, a channel geometry is selected with a porous wall layer occupying the lower region from $z = 0$ to $z = h$. For the sake of simplicity, h is set to be equal to the height of the free region, H. Thus from $z = H$ to $z = 2H$, the region is treated as a free channel, as shown in 6.1. The domain lengths in x and y direction are set as $3H$ and $2H$ respectively. A bulk velocity is prescribed for the free channel region, U_b and periodic boundary conditions for velocity are set in x and y directions. Further, no-slip boundary conditions are set for top and bottom boundaries at $z = 0$ and $z = 2H$. The temperature boundary conditions are the same as the velocity boundary conditions with the exception at $z = 0$ and $z = 2H$ where $T(x, y, z = 0) = 303K$ and $T(x, y, z = 2H) = 298K$. This maintains a temperature ratio $T_{hot}/T_{cold} \sim 1.01$, which is well within the validity of the Oberbeck-Bousinessq approximation. Pressure boundary conditions are maintained as periodic in x and y direction and zero Neumann condition is prescribed at $z = 0$ and $z = 2H$. The simulation model is inspired from the work done by Breugem and Boersma (2005), where the turbulent flow was simulated over an arrangement of 5400 cubes distributed as $30 \times 20 \times 9$ in the x, y and z direction. As shown in 6.1, d_p denotes the cube size which is fixed at 0.05 and the intercube spacing at d_f. Also d_f equals d_p and the porosity can be calculated as $\epsilon = 0.875$.

6.2 Parameter specification

The problem described above can be conceptualized as a turbulent bulk mass flow over a porous wall layer, in the presence of thermally induced buoyancy-driven convection (Figure 6.1).

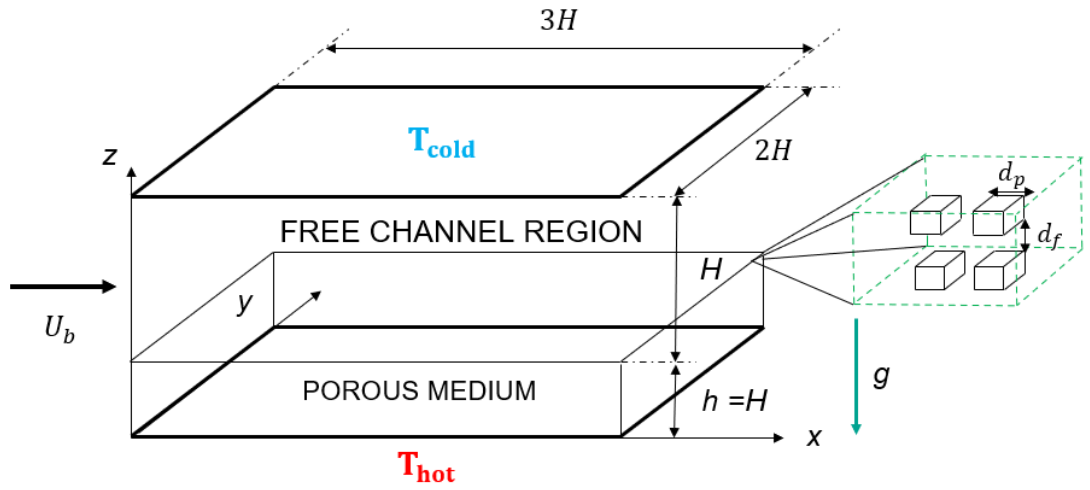

Figure 6.1: Schematic to represent setup for external-pressure driven flow over porous layer coupled with thermal gradient driven convection. The enlarged inset on the right is a zoomed in view showing the porous cube sizes and the spacing between the porous cubes.

A wall friction velocity can be defined for such pressure-driven turbulent flows given by:

$$u_\tau = \sqrt{-\frac{1}{\rho_f}\frac{\partial p_e}{\partial x}\frac{H}{2}}. \tag{6.2.1}$$

where $H/2$ is taken as the characteristic length scale, $-\frac{\partial p_e}{\partial x}$ is the external pressure gradient (e denotes external) and ρ_f is the density of the fluid. (Note: Although the flow is pressure-driven, the simulations are actually carried on with a constant bulk velocity forcing and the pressure gradient is allowed to become statistically steady after the transient phase. The momentum field is said to have reached a steady state then.)
The convective heat transfer coefficient can be defined as:

$$h_{conv} = \frac{\dot{q}}{T_{hot} - T_{cold}}, \tag{6.2.2}$$

where $\dot{q}$ is the heat flux.
The physics behind the thermo-fluids governing this problem, thus can be expressed as a function of the following parameters:

$$h_{conv} = f(\nu_f, u_B, h, H, d_p, d_f, \alpha\Delta T g, \rho c_p|_f, \rho c_p|_p, k_f, k_p), \tag{6.2.3}$$

where h is the convective heat transfer coefficient inside the domain, ν_f is the kinematic viscosity of the fluid, u_τ is the wall friction velocity, u_B is the bulk velocity. h is the height of the porous media, H is the total height of the domain, L is the length of the domain, d_p is the spacing between two cubes inside the porous media, d_f is the size of the cubes in the porous media, $\alpha\Delta T g$ is the buoyancy forcing (acceleration due to buoyancy), $\rho c_p|_f$ is the thermal capacity of the fluid, $\rho c_p|_p$ is the thermal capacity of the porous media, k_f is the thermal conductivity of the fluid and k_p is the thermal conductivity in the porous media solid.
Dimensional analysis using Buckingham π theorem yields 8 dimensionless parameters (12 parameters and 4 fundamental quantities - kg, m, s and K) given by :

- $Ri_B = \frac{\alpha\Delta T g}{u_B^2/(2H)}$ (Bulk Richardson number - ratio between buoyancy production and shear production),
- $Pr = \frac{\nu}{\kappa}$ (Prandtl number),
- $Re_B = \frac{u_B H}{\nu_f}$ (Bulk Reynolds number),
- $\rho c_p|^* = \frac{\rho c_p|_f}{\rho c_p|_p}$ (Ratio of thermal capacities between fluid and solid)

- $\kappa^* = \frac{k_f/\rho c_p|_f}{k_s/\rho c_p|_s} = \frac{\kappa_f}{\kappa_p}$ (Ratio of thermal diffusivities between fluid and solid),
- $h^* = \frac{h}{H}$ (Height ratio),
- $d^* = \frac{d_p}{d_f}$ (Geometrical property of porous layer),

Therefore it can be concluded from the dimensional analysis that :

$$\boxed{Nu = f(Ri_B, Pr, Re_B, \rho c_p|^*, \kappa^*, h^*, d^*)} \tag{6.2.4}$$

In the present work, Re_B is fixed at 5500, Pr is kept at 0.1,κ^* is infinity because the κ_s is fixed at 0, h^* is fixed at 1 and d^* is fixed at 1. Ri_B is varied from 0 to 5 to cover the spectrum from shear-driven flow to buoyancy-driven flow. u_B is kept at 1 and as a result u_τ changes with changing Ri_B at the porous interface and the top solid wall.

6.3 Mesh selection and flow resolution at walls

The viscous wall unit, z^+, given by zu_τ/ν, is the controlling parameter for resolving flows near the wall for shear-driven flows. Effectively, for a flow to be well resolved near the wall, the smallest grid cell at the wall should be of $z+ \sim \mathcal{O}(1)$. However, when convection is also present, it is important to determine if the flow resolving is still governed by the convective wall unit given by zw_f/ν where w_f is the inner region convective velocity scale. w_f for the inner wall region is given as:

$$w_f = \left(\frac{g}{T_{ref}}\overline{w'T'}z_h\right)^{\frac{1}{3}}, \tag{6.3.1}$$

where z_h is the length scale for the inner wall region. z_h scales with κ/w_f near the wall, so ultimately, w_f can be written as:

$$w_f = \left(\frac{g}{T_{ref}}\overline{w'T'}\kappa\right)^{\frac{1}{4}}, \tag{6.3.2}$$

Now, to determine the ratio of length scales and figure out which one dominates at a particular Richardson number,it is important to figure out the ratio $z_h/(\nu/u_\tau)$.

- $\frac{z_H}{D} = \frac{\kappa}{w_f D} = \frac{\kappa}{\left(\frac{g}{T_{ref}}\overline{w'T'}\kappa\right)^{\frac{1}{4}} D}$

From the Turbulent Kinetic Energy equation:

$$\frac{\partial \frac{1}{2}\overline{u_i'^2}}{\partial t} = \underbrace{\frac{g}{T_{ref}}\overline{w'T'}}_{\text{Buoyancy production}} - \underbrace{\overline{u_i'u_j'}\frac{\partial \overline{u_i}}{\partial x_j}}_{\text{Shear production}} + ... \tag{6.3.3}$$

The flux Richardson number Ri_f, in a fully developed channel flow, is defined as the ratio of buoyancy production to shear production given as:

$$Ri_f = \frac{\frac{g}{T_{ref}}\overline{w'T'}}{\overline{u'w'}\frac{\partial \overline{u}}{\partial z}}. \tag{6.3.4}$$

Substituting the shear production term with its scaling in terms of u_τ and D which is the length scale for outer region,

$$Ri_f = \frac{\frac{g}{T_{ref}}\overline{w'T'}}{u_\tau^3/kD}, \tag{6.3.5}$$

which can be rewritten as:

$$\kappa \frac{g}{T_{ref}} \overline{w'T'} = \frac{Ri_f u_\tau^3 \kappa}{kD} \tag{6.3.6}$$

where $k = 0.4$ and is the von-Karman constant and D is the outer region length scale (channel height in this case).
Substituting the relation in $\frac{z_H}{D}$:

$$\frac{z_H}{D} = \frac{\kappa^{\frac{3}{4}} k^{\frac{1}{4}}}{Ri_f^{\frac{1}{4}} u_\tau^{\frac{3}{4}} D^{\frac{3}{4}}} \tag{6.3.7}$$

$$= \left(\frac{\kappa}{\nu}\right)^{\frac{3}{4}} \left(\frac{\nu}{u_\tau D}\right)^{\frac{3}{4}} \frac{k^{\frac{1}{4}}}{Ri_f^{\frac{1}{4}}} \tag{6.3.8}$$

$$= \frac{1}{Pr^{\frac{3}{4}}} \frac{1}{Re_\tau^{\frac{3}{4}}} \frac{k^{\frac{1}{4}}}{Ri_f^{\frac{1}{4}}}. \tag{6.3.9}$$

Similarly, ν/u_τ scaled with D can be written as:

$$\frac{\nu/u_\tau}{D} = \frac{1}{Re_\tau}. \tag{6.3.10}$$

Therefore $z_H/(\nu/u_\tau)$ can be written as:

$$\frac{z_H}{\nu/u_\tau} = \left(\frac{kRe_\tau}{Ri_f Pr^3}\right)^{\frac{1}{4}}. \tag{6.3.11}$$

For the convective length scale to be the dominating factor over the viscous length scale, this ratio has to be of $\mathcal{O}(1)$. This gives:

$$Ri_f = \frac{kRe_\tau}{Pr^3} \tag{6.3.12}$$

$$\frac{Ri_f}{Re_\tau} = \frac{k}{Pr^3} \sim 400, \tag{6.3.13}$$

taking $Pr = 0.1$ as is used in the present work. It is seen from the simulations, that Re_τ at both the permeable wall and the solid wall are always about $\mathcal{O}(10^3)$ greater than the prescribed Ri_f (Ri_B is prescribed but it is later shown that $\mathcal{O}(Ri_f) \sim \mathcal{O}(Ri_B)$). So for this particular Pr, viscous wall unit always dominates. Convective length scale can dominate only at very high Pr, but then it is difficult to predict how Re_τ is going to vary with Ri_f. The grid dimensions in terms of wall units at the permeable wall and the top solid wall have been calculated and presented in Table 6.1. To resolve the flow, the grid in the wall-normal direction at the walls should be of the order of the Kolmogorov length scale to capture all the length scales. To ensure this, $z^+ \sim \mathcal{O}(1)$ is desired. It is seen that the z direction grid spacing is of $\mathcal{O}(1)$ for lower to moderate Ri_b, whereas it increases slightly at the permeable wall for higher Ri_b. However, it is seen that the flow remains resolved nevertheless.

6.3.1 Grid selection

In the beginning, a uniform grid of $900 \times 600 \times 600$ was selected for the simulations, but it became difficult to perfectly resolve the flow at the walls and interface. To resolve the flow, a finer grid was needed but having a uniform grid would increase the computational time exponentially. So a grid stretching algorithm was adopted such that at the two walls and the porous interface, the grid is fine. The grid relaxes in the core regions, to accommodate for the stretching at the walls as seen in 6.2. The grid stretching function is given as:

$$z_i = 1 - \frac{\tanh(\alpha(1 - 2i/N_z)}{\tanh(\alpha)} \tag{6.3.14}$$

where i is the grid point index and ranges from 1 to N_z. N_z is the number of gridpoints in the z and α is the grid stretching factor. In the present work a grid size of $600 \times 400 \times 400$ is used with α equals 3. It is important to mention that the grid is only stretched in the z direction. In the x and y direction a uniform grid is used with $dx = dy = 0.005$.

$\mathbf{Ri_b}$	**0**	**0.001**	**0.01**	**0.1**	**0.5**	**1**	**5**	**10**
Δx_p^+	3.43	3.45	3.40	3.65	4.49	5.09	7.77	8.91
Δx_w^+	1.95	1.94	1.93	1.98	2.13	2.24	2.60	2.74
Δy_p^+	3.43	3.45	3.40	3.65	4.49	5.09	7.77	8.91
Δy_w^+	1.95	1.94	1.93	1.98	2.13	2.24	2.60	2.74
Δz_p^+	1.05	1.06	1.04	1.12	1.38	1.56	2.39	2.74
Δz_w^+	0.6	0.59	0.59	0.61	0.65	0.68	0.80	0.84

Table 6.1: Grid spacing in terms of wall units at permeable and top wall. The subscripts p and w refer to permeable and solid walls respectively.

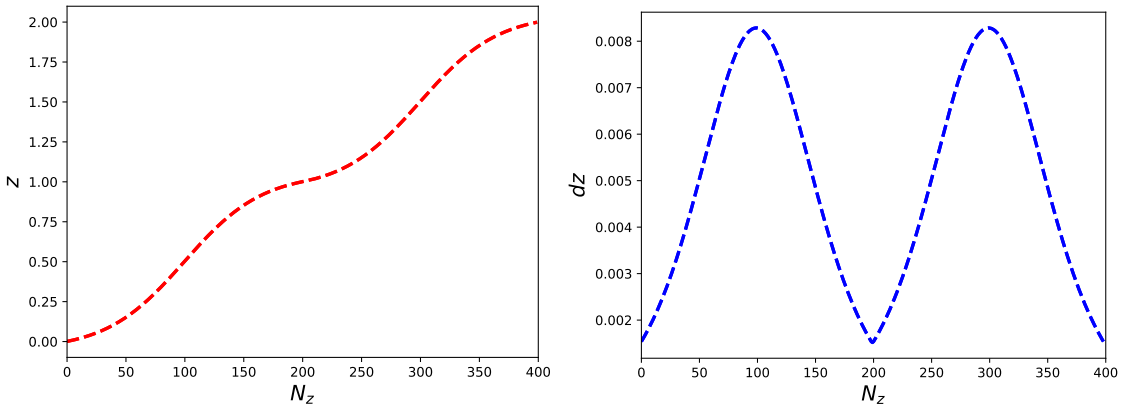

(a) (b)

Figure 6.2: (a) Stretched grid point coordinates in z direction; (b) Grid point spacing dz.

6.4 Postprocessing

The DNS data generated from the simulations go through postprocessing routines to arrive at observations from the data. The following subsections describe the spatial and temporal averaging techniques used to make the DNS data interpretable.

6.4.1 Intrinsic, superficial and Reynolds average

The direct numerical simulation produces 3-dimensional velocity, pressure and temperature fields. Due to the prescribed periodic boundary conditions in x (streamwise) and y (spanwise) directions, the statistical properties can be assumed to be homogeneous in these directions. So statistical variations will only be seen in the wall-normal or z direction. So intrinsic and superficial plane-averaged quantities are calculated. The superficial plane average quantities for the fluid phase are given by:

$$\langle Q \rangle^s = \frac{1}{L_x L_y} \int_A (1 - \psi(\mathbf{r})) Q(\mathbf{r}) dx dy \tag{6.4.1}$$

where Q is the physical quantity being averaged, V is the averaging volume, ψ is the solid phase indicator function which is 1 when $\mathbf{r}$ points in solid phase and 0 when it points to fluid phase.

Intrinsic averages are obtained when the quantities are averaged only in the fluid phase. It is obtained by:

$$\langle Q \rangle = \frac{\int_A (1 - \psi(\mathbf{r})) Q(\mathbf{r}) dA}{\int_A (1 - \psi(\mathbf{r})) dA} \tag{6.4.2}$$

The velocity or temperature field can be decomposed into plane-averaged and subfilter scale quan-

tities given by:

$$Q = \langle Q \rangle + \widetilde{Q}, \tag{6.4.3}$$

where $\langle Q \rangle = \frac{\langle Q \rangle^s}{\epsilon}$ where ϵ is the porosity given by:

$$\epsilon = \frac{1}{A} \int_A (1 - \psi(\mathbf{r})) dA. \tag{6.4.4}$$

Just like superficial and intrinsic averages take care of spatial averaging, Reynolds averaging finds temporal averages by means of time averaging. Temporal decomposition allows the quantities to be decomposed into the Reynolds average and fluctuations from the Reynolds average, given by:

$$Q = \overline{Q} + Q'. \tag{6.4.5}$$

Merging the spatial and temporal averaging:

$$Q = \langle Q \rangle + \widetilde{Q} \tag{6.4.6}$$

$$\langle \overline{Q} + Q' \rangle + \widetilde{\overline{Q} + Q'} \tag{6.4.7}$$

$$\langle \overline{Q} \rangle + \langle Q' \rangle + \widetilde{\overline{Q}} + \widetilde{Q'} \tag{6.4.8}$$

So finally:

$$Q = \underbrace{\langle \overline{Q} \rangle + \langle Q' \rangle}_{\text{Intrinsically averaged Reynolds averaged mean and fluctuations}} + \underbrace{\widetilde{\overline{Q}} + \widetilde{Q'}}_{\text{Sub-filter scale quantities}}. \tag{6.4.9}$$

The physical quantities in this present thesis will be intrinsically plane-averaged in the z-direction and Reynolds averaged in time to filter out the sub-filter scale quantities and fluctuations.

6.5 Parameter space chosen for simulation

To cover the entire spectrum from purely shear-driven to buoyancy-driven, a range of Ri_b needs to be selected. After careful consideration, 8 bulk Richardson numbers are chosen - 0, 0.001, 0.01, 0.1, 0.5, 1, 5 and 10. Above $Ra = 1700$, convection is triggered, whereas, above $Ra^* = 1300$, which translates to $Ra = 3.8 \times 10^6$, columnar convective structures appear in porous media convection. Also, below $Ri_b = 1$, the flow is shear driven, whereas above it the flow regime is buoyancy driven. This results in the parameter space being divided into 4 distinct regimes, with 2 additional regimes where conduction prevails. But these additional regimes are not considered in the thesis. Figure 6.3 shows the 8 simulation points being considered. In the analysis, the focus is placed on $Ri_b = 0$, $Ri_b = 0.1$, $Ri_b = 1$ and $Ri_b = 10$ to cover the different regimes.

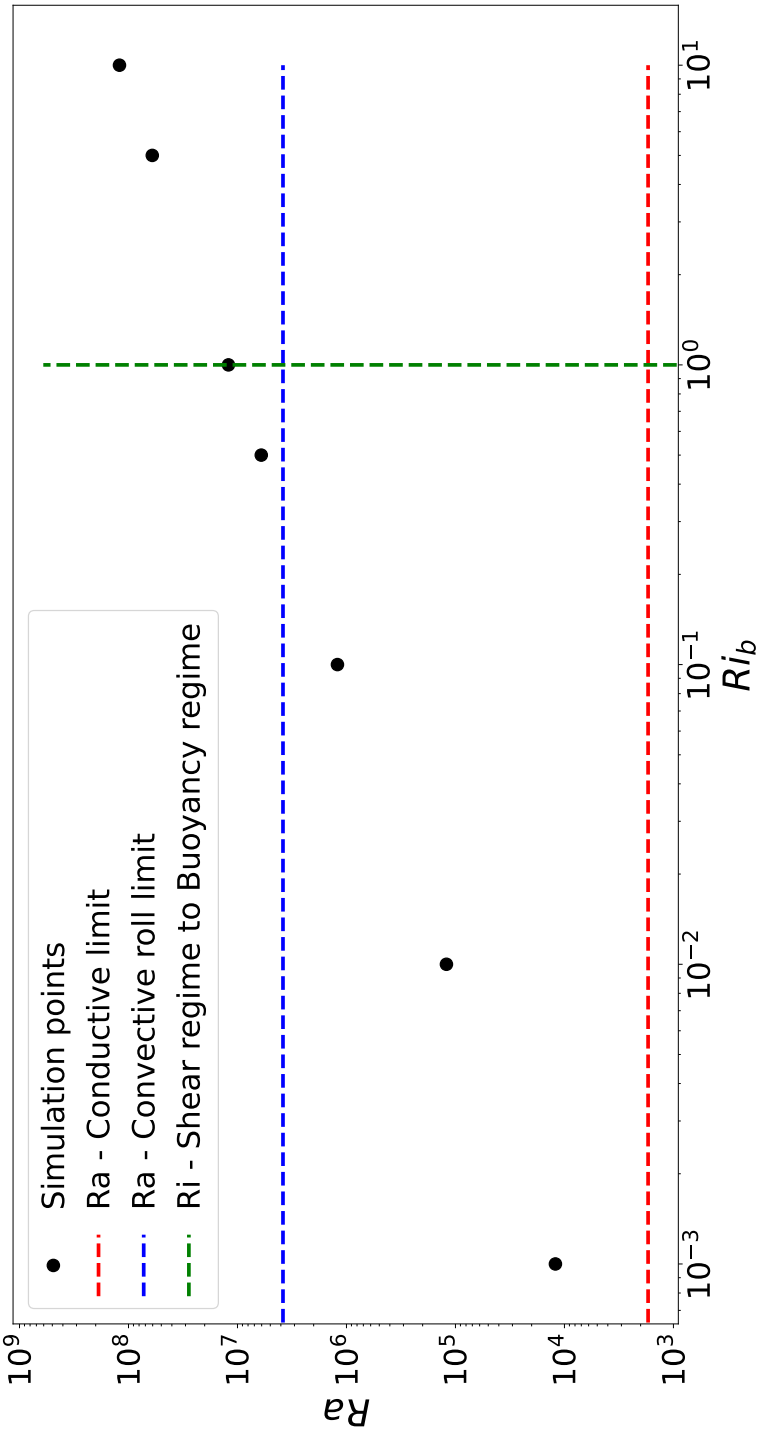

Figure 6.3: Parameter space divided into 4 regimes: the horizontal regime change shows a shift from shear-driven to buoyancy-driven, whereas the vertical regime change shows the transition from conduction in porous layers to convective waves to convective columnar structures.

7

Results

The present work aims at uncovering the underlying physics of mixed convection in turbulent channels over a porous wall layer, with unstable stratification. In pressure-driven channel flow with a porous wall layer, direct numerical simulations are carried out over a wide range of Richardson numbers. The effects of mixed convection on momentum and heat transfer characteristics combined with the presence of the porous media, uncovers various unique thermal structures. These structures work in redistributing the momentum and temperature in ways that deviate from the pure Rayleigh-Bénard case or the turbulent channel flow case.

7.1 Flow parameters

The present work is governed by a large set of parameters as shown in Section 6.2. However, after fixing the geometrical parameters and calculating Nusselt and Stanton numbers as a post-processing step, the problem boils down to 3 global parameters:

- $Ra = \frac{8H^3\alpha_f g\Delta\theta}{\kappa\nu}$: Rayleigh number, which is prescribed on the entire domain height $2H$ from $z = 0$ to $z = 2H$ where $\Delta\theta$ is the temperature difference between the two walls.
- $Re_b = \frac{Hu_b}{\nu}$: Bulk Reynolds number, prescribed on the bulk region of the domain ranging from $z = H$ to $z = 2H$.
- $Pr = \frac{\nu}{\kappa_f}$: Prandtl number.

A $4th$ dimensionless number can be reproduced from these, the bulk Richardson number, given by:

$$Ri_B = \frac{Ra}{Re_b^2 Pr} = \frac{8H\alpha_f g\Delta\theta}{u_b^2}. \tag{7.1.1}$$

In the present work, the Rayleigh number is calculated according to the prescribed Ri_B. The gravity term is calculated from Ri_b and used in the Bousinessq term in the wall-normal momentum equation. The bulk velocity u_B is set as 1 and the reference length scale is set at $l_{ref} = 2H$. (Note: The bulk Richardson number is kept positive throughout the thesis. This is mainly because it is treated as a bulk quantity providing information about the magnitude of buoyancy dominance over shear dominance.)

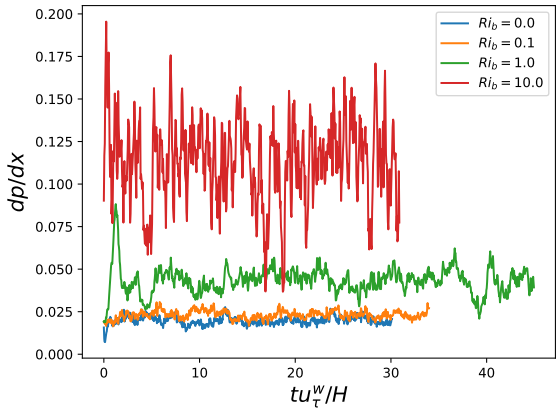

Figure 7.1: Streamwise pressure gradient convergence with non-dimensionalized time for $Ri_b = 0, 0.1, 1, 10$.

7.2 Convergence of simulations

Figure 7.1 visualizes the evolution of the streamwise pressure gradient with non-dimensionalized time. The time is non-dimensionalized by u_τ^w/H which is also the inverse of eddy turnover time in the free channel. The simulations are carried out in a way where $Ri_b = 0$ is allowed to attain a steady state first after overcoming the transient state. The temperature, pressure and velocity fields from that steady timestep are used to restart the simulations of higher Ri_b. This is mainly done to save computational time by avoiding the transient state. So essentially, in Figure 7.1, the starting points have been shifted to $t^* = 0$ for all Ri_b. It is seen that with increasing Ri_b the fluctuation increases, which is expected because the turbulence intensity also increases.

$\mathbf{Ri_b}$	**0**	$\mathbf{10^{-3}}$	$\mathbf{10^{-2}}$	$\mathbf{10^{-1}}$	**0.5**	**1**	**5**	**10**
Ra	0	6050	6.05×10^4	6.05×10^5	3.025×10^6	6.05×10^6	3.025×10^7	6.05×10^7
Nu	1.8917	1.8925	1.8014	2.6641	4.7989	7.1326	16.7222	23.2631
St	0.003439	0.00344	0.00327	0.00484	0.008725	0.01296	0.0304	0.04229
C_f^p	0.0304	0.0315	0.0293	0.0353	0.0540	0.0687	0.1597	0.2103
C_f^w	0.0101	0.01	0.00985	0.0104	0.0122	0.0132	0.0179	0.0199
$\frac{C_f^p}{C_f^w}$	2.96	2.81	2.97	3.27	4.426	5.73	8.03	10.57

Table 7.1: Variation of relevant non-dimensional parameters at different bulk Richardson numbers.

7.3 Flow statistics - Mean and RMS quantities

The flow statistics for momentum and thermal energy transfer for flow simulations ranging from purely shear-driven cases to high Ri_b are presented in this section. The different Reynolds numbers used for characterizing the flow situations are listed in Table 7.1. The friction Reynolds number

at the top solid wall is given as $Re_\tau^w = u_\tau^w H/\nu$. At the permeable wall, friction Reynolds number is given as $Re_\tau^p = u_\tau^p H/\nu$. u_τ^p is defined as the friction velocity at the permeable wall given as: $u_\tau^p = \sqrt{-\langle\overline{u'w'}\rangle + \nu\partial\langle\overline{u}\rangle/\partial y_{y=H}}$. The effect of varying Richardson numbers for Ri_b ranging from 0 to 10 is illustrated in Figure 7.2. All quantities are intrinsically averaged, which means only the value of the quantities in the fluid domain is used in the averaging. In a perfect pressure-driven channel flow ($Ri_b = 0$), for $Re_b = 5500$, a turbulent flow profile is expected with distinct viscous sublayer, log-layer and core region. Breugem and Boersma (2005) showed that in the presence of a porous wall region, the permeable wall behaves like a roughness layer which effectively shifts the peak of mean velocity, causing a deviation from the turbulent flow profile. Breugem and Boersma (2005) derived a relation between the position of maximum velocity and the wall friction velocities which is:

$$\frac{\delta_w}{H} = \frac{(u_\tau^p)^2}{(u_\tau^w)^2 + (u_\tau^p)^2}, \tag{7.3.1}$$

where δ_w is the position of peak velocity.

With increasing Ri_b, the effect of buoyancy starts setting in. It is however seen that until $Ri_b < 0.01$ there is no deviation from the pure shear-driven case. The position of peak velocity shifts very slightly towards the solid wall because of increasing shear stress at the permeable wall. At around $Ri_b = 1$, the skewness of the velocity profile starts flattening out. Delving deeper, it is actually seen that there is a peak seen for higher Ri_b at the position of zero shear stress, but that peak is much lower than for pure shear-driven flows. However, another peak is seen to form near the permeable wall, which is formed due to momentum transfer from the flattening of the profile near the solid wall. In the core region, with increasing buoyancy, the profile is almost flat. The coefficient of skin friction values at the permeable wall (C_f^p) and the solid wall (C_f^w) are listed in Table 7.1. It is seen that the ratio between the skin frictions goes up with increasing Ri_b, especially in the buoyancy regime. The detailed reason behind the shear stress ratio increase is explained in 7.4.

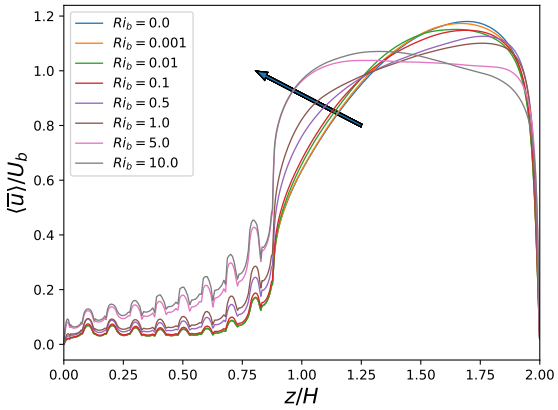

Figure 7.2: Instrinsic, Reynolds averaged mean velocity normalized by bulk velocity for varying bulk Richardson number. The arrow indicates that in the pointed direction, with increasing Ri_b, the velocity profile progressively becomes blunted and increases near the permeable wall, while decreasing near the solid wall.

The dip in peak mean velocity for increasing Ri_b can also be attributed to the increase in buoyancy-induced turbulence. Due to increasing turbulence, the streamwise and wall-normal fluctuations also increase. Inside the porous media, for lower Ri_b, the fluctuations are low because smaller velocity scales are filtered out by the solid matrix. Inherently, the porous matrix acts as a dissipation zone of fluctuations. Larger scale fluctuations decrease slowly inside the porous layer. Since turbulence does not play a role inside this region, the velocity fluctuations inside the region are induced by pressure fluctuations, as also seen by Breugem et al. (2006). In the free region, there are two main regions for the production of fluctuations – near the permeable wall induced by Kelvin-Helmholtz-type instabilities, and near the solid wall induced by velocity streaks. Both these regions show a peak in fluctuation quantities as seen in 7.3a. Since the mode of production of these fluctuations is different, the one near the permeable wall shows broader peaks than near the solid walls. With increasing Ri_b, the peaks keep increasing and the trend stays similar for streamwise velocity fluctuations, as is expected.

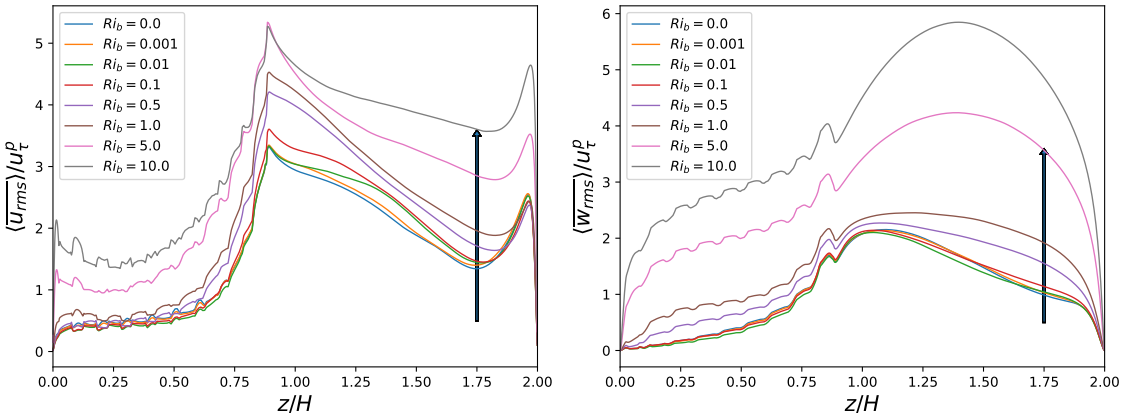

Figure 7.3: (a) Intrinsic, Reynolds root mean squared averaged streamwise velocity normalized by friction velocity at permeable wall. (b) Intrinsic, Reynolds averaged root mean squared wall-normal velocity normalized by friction velocity at permeable wall. Appendix 9.2 shows the way these intrinsic quantities are calculated. The arrow points in the direction of increasing Ri_b.

The wall-normal velocity fluctuations, however, act in a different way with the increasing influence of buoyancy, as seen in 7.3b. For purely shear-driven flows at $Ri_b = 0$, a peak for w_{rms} is seen just above the permeable wall. This production zone for wall-normal fluctuations can be attributed to the presence of K-H instabilities. No similar production zones are seen near the top solid wall, as is expected for a shear-driven turbulent flow. The behaviour inside the porous media is similar to that of u_{rms} with the fluctuation decreasing rapidly as the flow penetrates the solid matrix deeper. An interesting trend is observed for increasing Ri_b where the peak of w_{rms} keeps increasing and flattening, especially at $Ri_b > 1$. At $Ri_b = 5$, the peak is seen to have shifted to the core region of the free channel. This shows that buoyancy is the driving force behind the production of w_{rms} at higher Ri_b unlike at sub-unity Ri_b where the effect of buoyancy is minimal. Since buoyancy is the driving factor, the production zone shifts to the core region proving that buoyancy has a dominating effect in the bulk. It is also seen that in the porous region, there are significant wall-normal fluctuations at $Ri_b > 1$. This shows that the solid matrix does not filter the smaller velocity scales effectively and turbulence penetrates the porous media. Another possible explanation for the increase in turbulence intensity inside the porous matrix can be traced to the formation of columnar plumes in the buoyancy regime. These thermal plumes, at high Ri_b, give rise to instabilities, which in turn act as production zones for turbulence. The solid matrix however do not let the perturbations grow and due to drag dissipation, the turbulence is much lesser than that in the free channel.

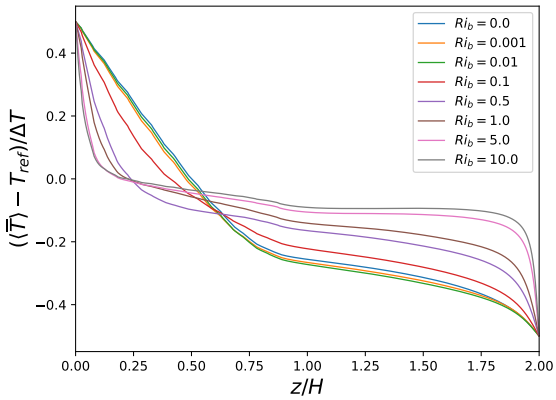

Figure 7.4: Instrinsic, Reynolds averaged mean temperature normalized by the temperature difference between hot and cold wall for varying bulk Richardson number. ($T_{ref} = (T_{hot} + T_{cold})/2$)

The analysis of the temperature field for flow situations from shear-driven flows to buoyancy-driven flows reveals interesting regime changes which will be discussed in detail in this part of the section. When the effect of shear dominates the flow conditions for $Ri_b = 0, 0.001, 0.01$, it is seen in 7.4 that inside the porous region, a linear mean temperature profile is seen which seems to overlap each other. In the free channel region, due to turbulent mixing, the temperature profile flatten out and no longer show a linear variation. This trend starts changing from $Ri_b = 0.1$, where a deviation is seen from the laminar temperature profile in the porous layer. The trend points towards the formation of a distinct temperature boundary layer inside the porous wall region, near the wall. A similar feature is noticeable in the free region also where the profile in the core starts flattening out, giving way to sharp gradients at the wall. For $Ri_b = 1$, the profile starts to show a strong resemblance with the temperature profile in a pure Rayleigh Bénard convection case, indicating that the effects of shear stress have very less or no effect anymore on the thermal energy transfer. By increasing Ri_b to 10, the profile in the core is almost flat with steep gradients at the walls. However, it is also seen that the characteristics of the mean temperature curve in the porous and free region are a bit different even at very high Ri_b. This shows that though at high Ri_b, turbulence penetrates into the porous matrix, the presence of the porous media prevents the profile from completely flattening and a very slight gradient is formed. The intrinsically averaged

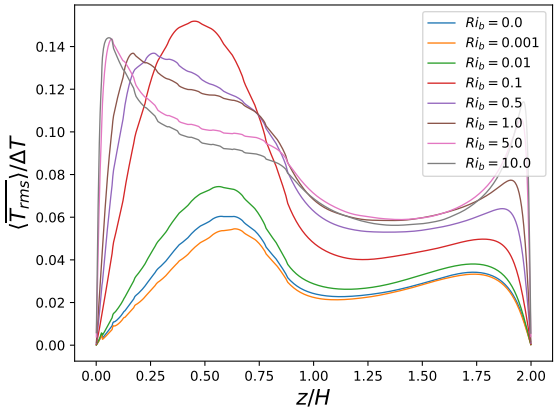

Figure 7.5: Instrinsic, Reynolds averaged root mean squared temperature normalized by the temperature difference between hot and cold wall for varying bulk Richardson number.

root-mean squared temperature profiles, calculated as $T_{rms} = \sqrt{\langle\overline{T'^2}\rangle}$ are shown in 7.5. A general trend observed across all tested Ri_b is that two peaks are observed - one near the solid wall and one inside the porous region. The reason behind the occurrence of peaks or production zones of T_{rms}, however, differs for low and high Ri_b. At low Ri_b till 0.01, a peak is seen near the top solid wall denoting the position for maximum production of temperature fluctuations in the buffer region of the free channel. The surprising phenomenon is the presence of a local maxima inside the porous region. For shear-driven flows with little or no effect of buoyancy, turbulence does not penetrate the porous media because the solid matrix filters out small-scale fluctuations. The large-scale structures that do advect into the matrix, are inactive in the sense they do not enable mixing and do not aid in thermal or momentum transfer. Rather, they themselves are largely induced by pressure waves. These large-scale waves give rise to large thermal gradients as seen in 7.4, and thus maxima of fluctuations occur inside the porous media. With increasing Ri_b, a very unique feature is observed. Suddenly at about $Ri_b = 0.1$, a large jump in the peak inside the porous media is observed. A suitable reasoning can be formulated based on the observations made by Hewitt et al. (2012) who noticed that around Rayleigh-Darcy number 1300, in pure porous media convection, columnar thermal structures start appearing in the bulk region, which was termed as 'megaplumes' by the author. The $Ra - Da$ when $Ri_b = 0.1$ can be calculated as $Ra^* = Ri_b Re_b^2 PrDa = 102$. Clearly, this is much lower than the transition limit seen by Hewitt et al. (2012). However, columnar plumes are seen to develop as seen in Figure 7.7 at $Ri_b = 1$ and greater. So it can be theorized that for mixed convection, the transition regime starts earlier than that for pure convection in porous media. The T_{rms} trends start showing influences of buoyancy past $Ri_b = 0.1$, with significant flattening in the core regions. In the porous layer, the peak shifts towards the wall because of the increasing influence of buoyancy-induced turbulence which starts

penetrating inside the solid region. So the reason for the formation of production zones inside the porous layer at higher Ri_b is turbulent mixing, unlike that at lower Ri_b. Noticeable differences are still seen between the characteristics of T_{rms} between free and porous layers. This shows that even though the effect of the presence of the solid matrix is highly reduced, it still manages to filter out some of the smallest scales. This in turn prevents the profile from completely flattening out in the solid region, unlike the free channel region.

7.3.1 Qualitative analysis of flow

At $Ri_b = 0$, the flow is purely shear-driven. As seen in Figure 7.7a, the flow structures at the top solid wall and the permeable wall are different as seen in the $x - z$ plane. A similar phenomenon is also noted by Breugem and Boersma (2005), where streaks appear at the top wall as is expected for a turbulent channel flow but Kelvin-Helmholtz-type instability-driven eddies are seen at the permeable wall. The emergence of K-H-type instabilities is a consequence of the top layer of the porous layer acting like a roughness layer. Figure 7.6b shows that the wall-normal mean velocity is almost zero everywhere except at the positions of the K-H instabilities. The flow is laminar inside the porous layer because small-scale fluctuations do not advect inside the solid layer. By increasing the effect of buoyancy at $Ri_b = 0.1$, updrafts slowly start appearing. Figure 7.6d shows that the updrafts are not vertical exactly, but due to the persisting shear flow are somewhat inclined. The K-H instabilities start breaking up as a result of this, as also seen in Figure 7.7c. Subsequently, it is also seen the boundary layer thickness decreases at the top solid wall indicating that turbulent intensity has increased in the domain. For $Ri_b = 1$, the effect of buoyancy is effectively the same as that of shear in the domain. The updrafts near the permeable wall increase as seen in Figure 7.7e and 7.6f, while small rollers start appearing in the bulk of the free region which is representative of convective turbulence. These structures grow smaller spatially and the instabilities are not localized near the permeable wall anymore at $Ri_b = 10$ as in Figure 7.7g. The wall-normal mean velocity also shows small spatial structures, almost streak-like (Figure 7.6h). The whole domain has increased turbulence intensity, with the fluctuations penetrating the porous media also. The flow is no longer completely laminar inside the porous region. The boundary layer at the top wall is almost insignificant because of increased Re_τ there. From Table 7.2, it is observed that above $Ri_b = 1$, the roughness Reynolds number Re_d is more than 55. Hinze (1975) stated that when $Re_d > 55$, the wall can be classified as a fully rough wall. Even though in this case, the increase in Re_d is attributed to increasing u_τ^p, qualitatively it can be stated that for high Ri_b, the permeable wall starts behaving like a roughness layer. The Re_K also increases which in turn facilitates the penetration of the flow inside the porous matrix.

Close inspection of the thermal field reveals very interesting features with increasing Ri_b. Figure 7.7b shows the fluctuations of θ at the pure shear-driven case. The fluctuations are low inside the porous media and increase in the bulk of the free channel. An almost stratified, temperature pattern is seen in the porous zone, decreasing linearly from the wall towards the interface. Due to turbulence in the channel region, there is significant mixing, which makes the mean temperature almost the same in this region. With increasing Ri_b at 0.1, a sudden increase in fluctuation is seen in the porous wall layer (Figure 7.7d). This probably signifies the start of a regime change for thermal structures inside the porous media. In the channel region, visible inclined thermal structures are seen which shows that although buoyancy has started to set in, the effect of shear is still dominant. $Ri_b = 1$ shows unique columnar structures in the porous media, which are characteristic of porous media convection around $Ra^* = 1300$. The interesting phenomenon noticeable is that these columnar structures somewhat start diffusing and start inclining in the direction of flow. This beautifully illustrates that at $Ri_b = 1$, when shear production and buoyancy production are almost equally dominating, the porous media shows increased effects of buoyancy whereas the channel region still shows features of a shear-driven flow. This is further indicative of the fact that buoyancy-driven fluctuations penetrate more into the solid matrix.

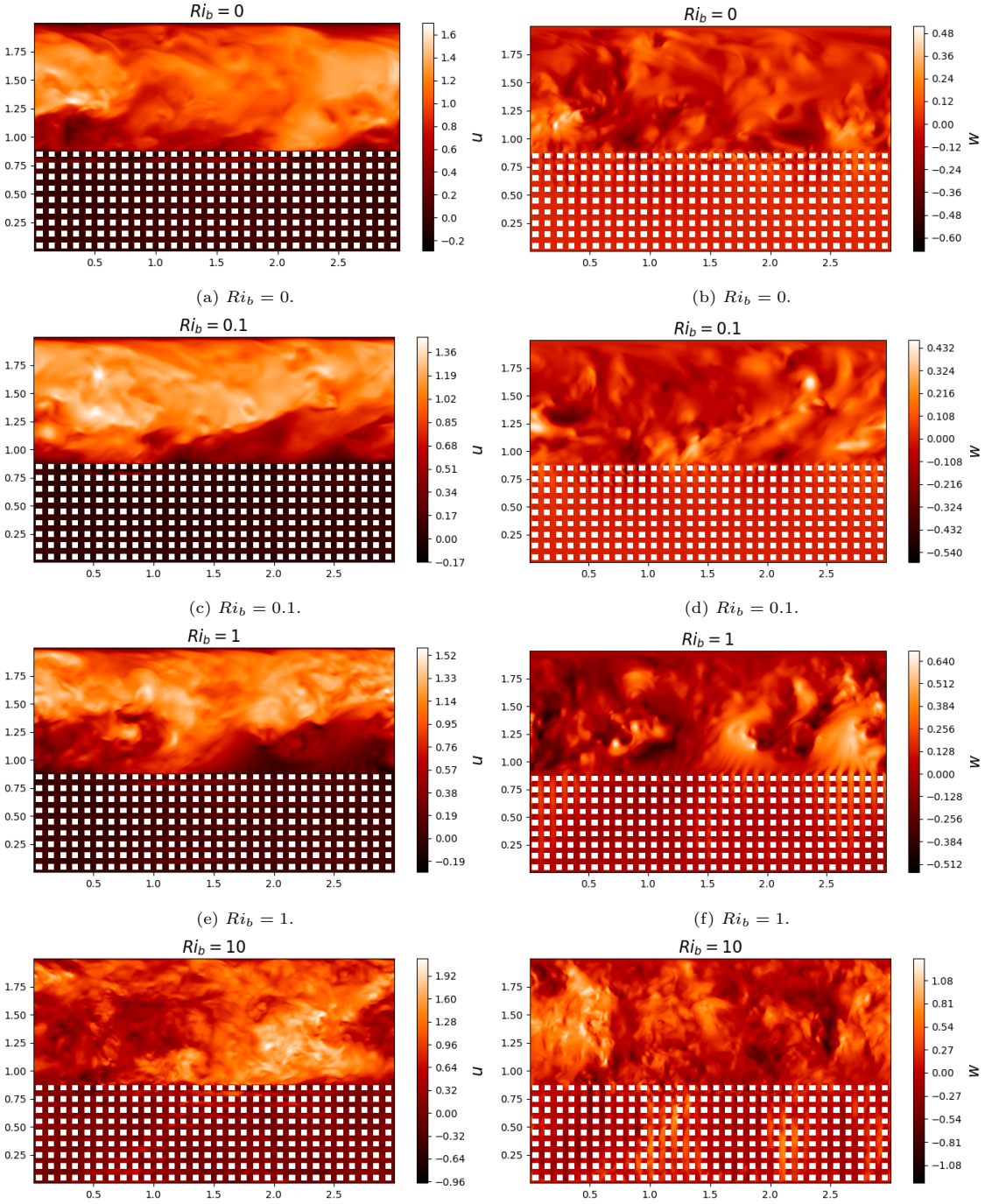

(a) $Ri_b = 0$.

(b) $Ri_b = 0$.

(c) $Ri_b = 0.1$.

(d) $Ri_b = 0.1$.

(e) $Ri_b = 1$.

(f) $Ri_b = 1$.

(g) $Ri_b = 10$.

(h) $Ri_b = 10$.

Figure 7.6: (a),(c),(e),(g) Streamwise velocity contours in the $x - z$ plane; (b),(d),(f),(h) Wall-normal velocity contours in the $x - z$ plane.

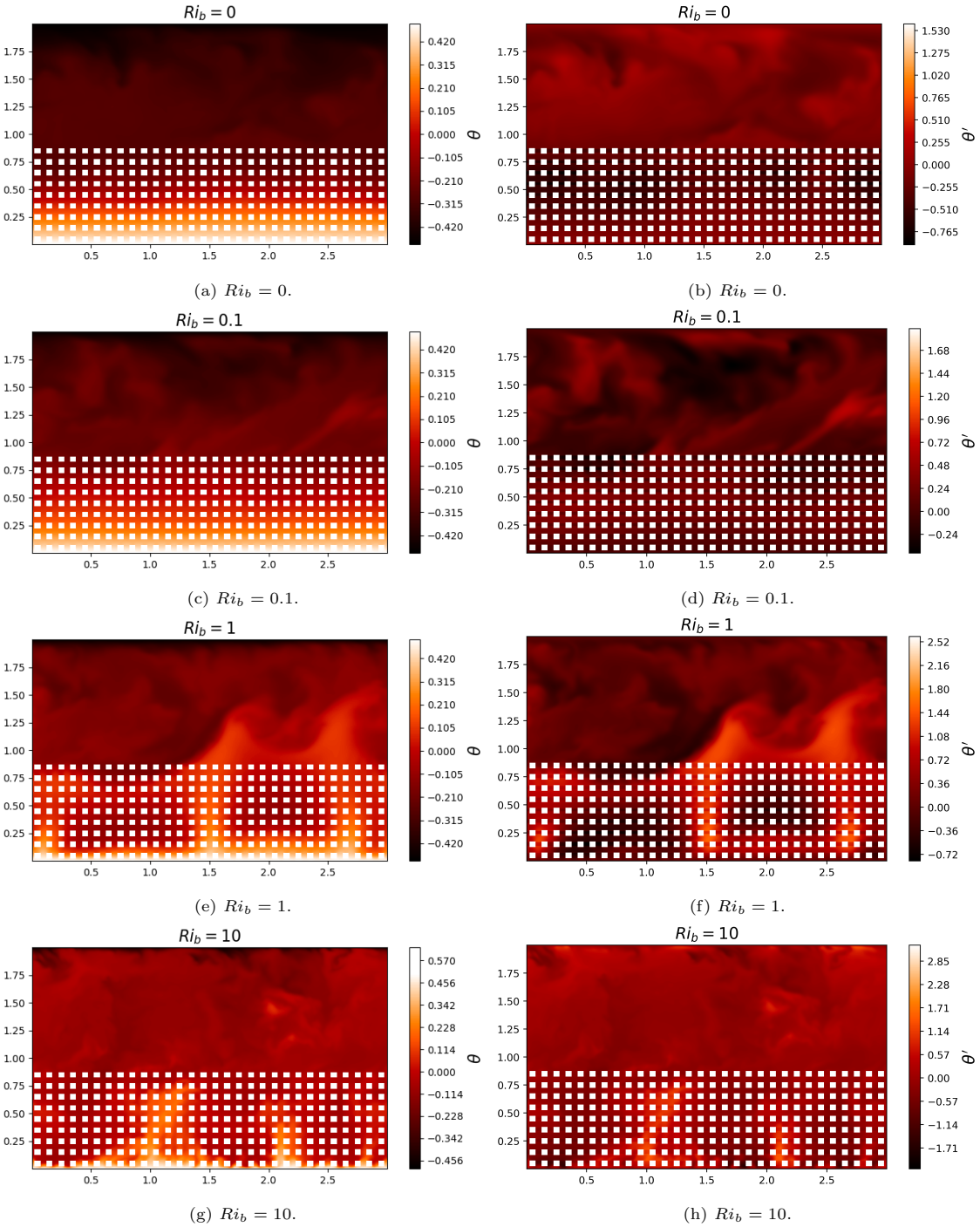

(a) $Ri_b = 0$.

(b) $Ri_b = 0$.

(c) $Ri_b = 0.1$.

(d) $Ri_b = 0.1$.

(e) $Ri_b = 1$.

(f) $Ri_b = 1$.

(g) $Ri_b = 10$.

(h) $Ri_b = 10$.

Figure 7.7: (a),(c),(e),(g) Temperature contours in the $x - z$ plane; (b),(d),(f),(h)Temperature fluctuation contours in the $x - z$ plane.

7.4 Stress and heat-flux budget

7.4.1 Stress budget

An important aspect differentiating turbulent flow over smooth walls and rough, permeable walls is how the characteristics of drag on the walls vary. To investigate the drag, the total shear stress exerted has to be determined. The total stress for a pressure-driven channel flow can be computed as:

$$\overline{\tau_{ij}} = -\overline{\rho u_i' u_j'} + \mu \frac{\partial \overline{u_i}}{\partial x_j}, \tag{7.4.1}$$

which for xz plane translates to:

$$\overline{\tau_{xz}} = \underbrace{-\overline{\rho u' w'}}_{\text{Reynolds stress}} + \underbrace{\mu \frac{\partial \overline{u}}{\partial z}}_{\text{Viscous stress}} . \tag{7.4.2}$$

Also, after intrinsically averaging, the equations become:

$$\langle \overline{\tau_{xz}} \rangle = \underbrace{-\langle \overline{\rho u' w'} \rangle}_{\text{Reynolds stress}} + \underbrace{\mu \frac{\partial \langle \overline{u} \rangle}{\partial z}}_{\text{Viscous stress}} . \tag{7.4.3}$$

In the present work, the total stress for varying Ri_b is shown in Figure 7.8. The stress profiles are normalized with $(u_\tau^w)^2$. So effectively the stress at the top solid wall takes a value of -1 in all the cases across all Ri_b. The analysis for the stress characteristics can be done separately for the porous and the channel region. In the porous region, at lower Ri_B, when the flow is still shear-driven and turbulence has not penetrated the solid matrix, both the Reynolds stress and the viscous stresses are very low. The sudden peaks and troughs in the viscous stress can be attributed to the undulations in the intrinsic mean velocity profile. With increasing Ri_B, it is seen that the viscous stress remains almost the same in the porous region which shows that convection does not have a direct influence on viscous stresses. This also reinforces the fact that buoyancy acts on the bulk of the fluid and has little or no influence on the molecular diffusion of momentum. The viscous stress peaks a bit at the permeable wall, but not as strongly as that at the top wall. This can be attributed to the no-penetration boundary condition being nullified to an extent at the permeable wall. The Reynolds stress on the other hand shows significant variation with increasing Ri_B. As the regime crosses over from shear-driven to buoyancy-driven, the Reynolds stress increases in magnitude and this is instrumental in showing that buoyancy induces turbulence penetration inside the solid matrix. The Reynolds stress is maximum at the permeable wall due to the reduced effect of the wall-confinement effect. In a perfectly shear-driven setup, the porous layer filters out small-scale velocity fluctuations and causes the flow to laminarize inside the solid matrix. With increasing buoyancy, the filtering is rendered almost ineffective.

In the free region, the total stress profile is expected to have a linear profile as a function of the wall-normal distance z and can be scaled as:

$$\frac{\overline{\tau_{xz}}}{\rho} = -\overline{u'w'} + \nu \frac{\partial \overline{u}}{\partial z} = (u_\tau^p)^2 \left(2 - \frac{z}{H}\right) + (u_\tau^w)^2 \left(\frac{z}{H} - 1\right), \tag{7.4.4}$$

where z ranges from H to $2H$.

This trend is indeed observed in the total stress profile characteristics in the clear region. However, it is also observed that with increasing Ri_b, the total stress at the interface scaled with the friction velocity at the solid wall increases. Also, the position of zero stress shifts towards the solid wall, which also denotes the position of mean velocity maxima. The viscous stress remains almost close to zero, except at the permeable wall and the inner region near the solid wall. The majority of the contribution to total stress comes from Reynolds stress $\langle \overline{u'w'} \rangle$, which increases with the increasing dominance of buoyancy in the clear region, like the porous region. This raises a question of how much of a contribution the Bousinessq approximation term has to the Reynolds stress term. From a general point of view, the shear stress balance is obtained from the streamwise

$\mathbf{Ri_B}$	**0**	$\mathbf{10^{-3}}$	$\mathbf{10^{-2}}$	$\mathbf{10^{-1}}$	**0.5**	**1**	**5**	**10**
Re_τ^p	670.92	690.50	666.75	731.37	909.74	1019.84	1554.39	1783.82
Re_τ^w	390.24	388.94	386.74	397.29	431.12	448.33	521.21	548.68
Re_d	33.712	34.529	33.337	36.568	45.487	50.992	77.719	89.191
Re_K	12.24	12.38	12.29	13.48	16.77	18.81	28.66	32.89

Table 7.2: Table showing Reynolds numbers and how they vary with changing bulk Richardson number.

momentum balance. But the buoyancy term appears in the wall-normal momentum balance, so it does not influence the stress balance directly. However, the buoyancy term affects the wall-normal velocity fluctuations, which affects the Reynolds stress term. To delve deeper into this, the transport equation for $\langle\overline{u'w'}\rangle$ is investigated. It is seen that with increasing Ri_b, especially past $Ri_b = 1$, the buoyancy production of shear stress dominates over the shear production of shear stress. So inherently, buoyancy does play a role in influencing the shear stress balance. The detailed analysis is done in 7.4.1.1. Further, it is also observed that Re_τ^p increases faster with increasing Ri_b than Re_τ^w as seen in Table 7.2. This increase is also attributed to the Reynolds stress increasing at a faster rate and is explained in 7.4.1.1.

7.4.1.1 Determination of contribution of buoyancy to the production of Reynolds stress

The Reynolds-averaged transport equation for $\overline{u'w'}$ is given as:

$$\frac{\partial\overline{u'w'}}{\partial t} + \frac{\partial w\overline{u'w'}}{\partial z} = - \underbrace{\left(\overline{u'w'}\frac{\partial\overline{w}}{\partial z} + \overline{w'^2}\frac{\partial\overline{u}}{\partial z}\right)}_{\text{Shear stress production for Reynolds stress}} - \underbrace{\left(\frac{g}{T_{ref}}\overline{w'T'} + \frac{g}{T_{ref}}\overline{u'T'}\right)}_{\text{Buoyancy production for Reynolds stress}} \tag{7.4.5}$$

$$+ \text{Transport terms} + \text{Dissipation terms}. \tag{7.4.6}$$

Focusing just on the shear stress and buoyancy production terms, it is necessary to analyse how the buoyancy starts to increase its dominance over the shear production term in the free region. It is seen that the peak shear production of Reynolds stress increases manifold with increasing Ri_b, at the interface. If examined closely in Figure 7.9, the rate of increase increases with increasing Ri_b, especially in the buoyancy-dominated regime. It is also observed that the shear region near the permeable wall gets narrower when the influence of gravity increases. It can be thus concluded that, with increasing Ri_b, buoyancy forces the shear regime to get narrower, while increasing the shear production term to peak at the interface. Subsequently, the friction Reynolds number also increases at the permeable all. This, in turn, forces the position of zero shear more towards the top wall.

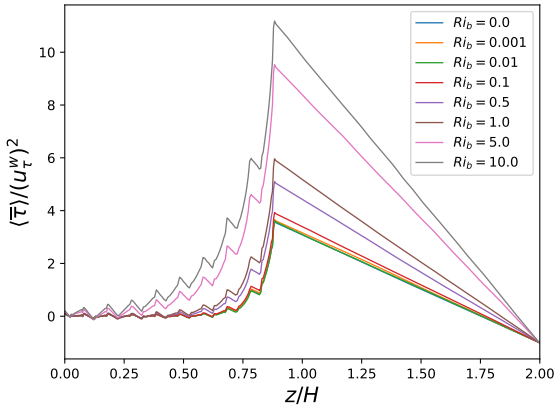

Figure 7.8: Total shear stress with varying Richardson number.

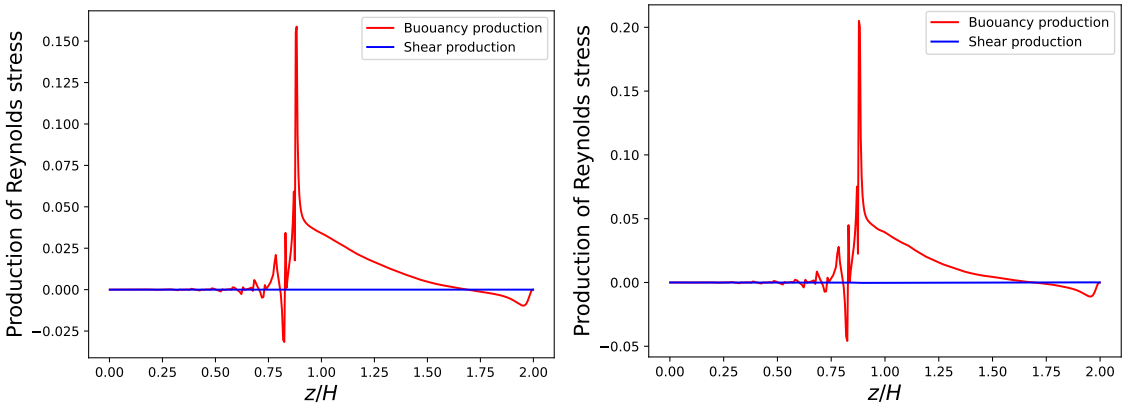

(a) $Ri_b = 0$.

(b) $Ri_b = 0.1$.

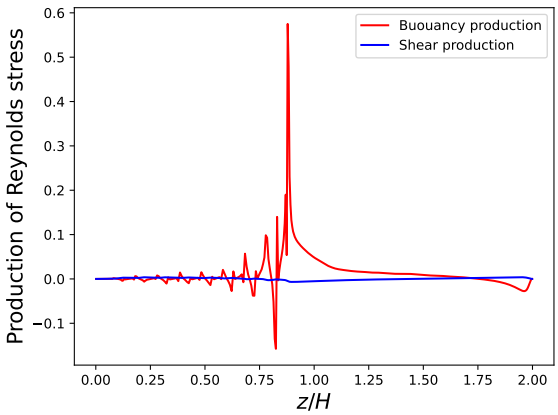

(c) $Ri_b = 1$.

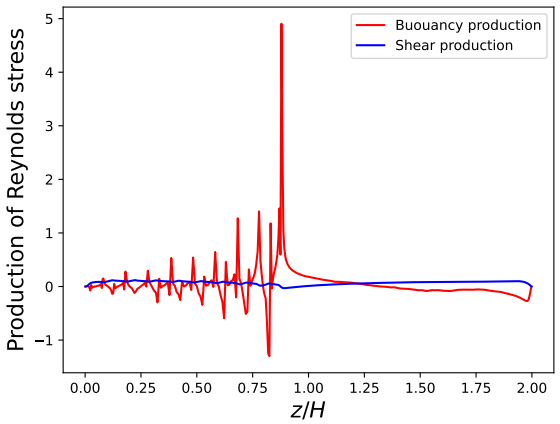

(d) $Ri_b = 10$.

Figure 7.9: Shear production and buoyancy production of Reynolds stress for (a)$Ri_b = 0$, (b)$Ri_b = 0.1$, (c)$Ri_b = 1$ and (d)$Ri_b = 10$.

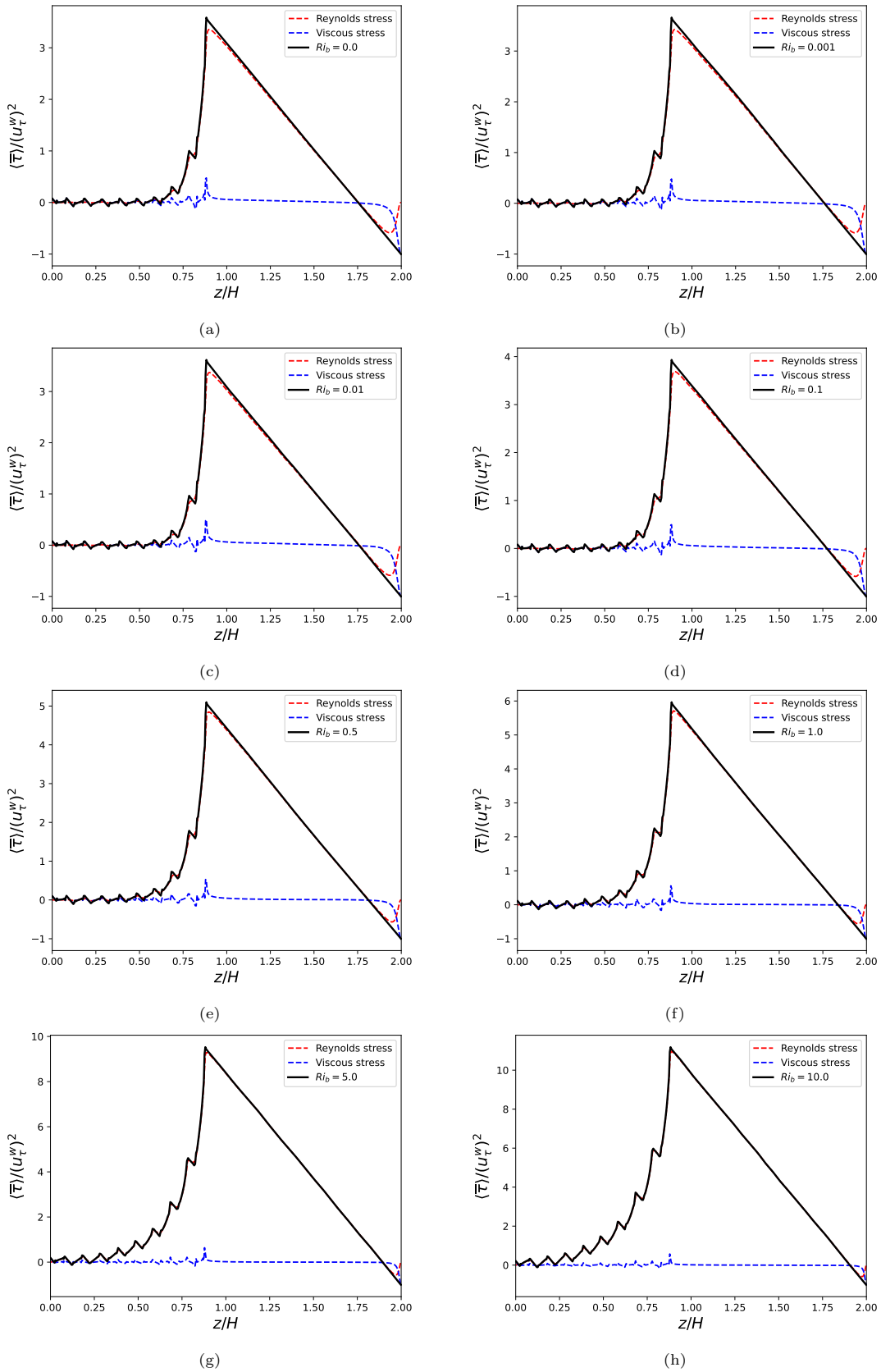

Figure 7.10: The contribution of viscous stress and Reynolds stress to total stress with varying Richardson number: (a) $Ri_b = 0$, (b) $Ri_b = 0.001$, (c) $Ri_b = 0.01$, (d) $Ri_b = 0.1$, (e) $Ri_b = 0.5$, (f) $Ri_b = 1$, (g) $Ri_b = 5$ and (h) $Ri_b = 10$.

7.4.2 Heat-flux budget

To analyse the effects of varying Richardson numbers on thermal characteristics, obtaining a heat-flux budget is essential. The heat-flux budget provides information on how the different flux components vary with increasing buoyancy, but essentially the budget remains constant over the domain. The energy equation is given by:

$$\rho c_p|_l \frac{\partial T}{\partial t} = \frac{\partial \left(k_{eff} \frac{\partial T}{\partial x_j} \right)}{\partial x_j} - \frac{\partial \left(\rho c_p u_j T \right)}{\partial x_j}. \tag{7.4.7}$$

Normalizing the energy equation with $\rho c_p|_l$:

$$\frac{\rho c_p|_l}{\rho c_p|_l} \frac{\partial T}{\partial t} = \frac{\partial \left(\frac{k_{eff}}{\rho c_p|_l} \frac{\partial T}{\partial x_j} \right)}{\partial x_j} - \frac{\partial \left(\frac{\rho c_p}{\rho c_p|_l} u_j T \right)}{\partial x_j} \tag{7.4.8}$$

which can be written as:

$$\frac{\rho c_p|_l}{\rho c_p|_l} \frac{\partial T}{\partial t} = \frac{\partial \left(\frac{k_{eff}}{\rho c_p|_l} \frac{\partial T}{\partial x_j} - \frac{\rho c_p|_l}{\rho c_p|_l} u_j T \right)}{\partial x_j} \tag{7.4.9}$$

The total heat flux can be estimated from the RHS of the equation by:

$$q_{total} = \underbrace{\frac{k_{eff}}{\rho c_p|_l} \frac{\partial T}{\partial x_j}}_{\text{Molecular dissipation}} - \underbrace{\frac{\rho c_p|_l}{\rho c_p|_l} u_j T}_{\text{Turbulent heat flux}} \tag{7.4.10}$$

In the present simulations, $\rho c_p|_l$ is taken to be 1. Thus the resulting heat flux becomes:

$$q_{total} = \kappa_{eff} \frac{\partial T}{\partial x_j} - u_j T \tag{7.4.11}$$

Focusing on the vertical z-direction and after intrinsic and Reynolds averaging, the total heat flux in the z-direction is:

$$\langle \overline{q_{z,total}} \rangle = \overline{\langle \kappa_{eff} \frac{\partial T}{\partial z} \rangle} - \langle \overline{wT} \rangle \tag{7.4.12}$$

The heat flux has been calculated as shown in 7.4.11. The resulting profiles have been normalized by $w_\tau^p T_\tau^p$ where w_τ^p is the wall-normal friction velocity at the permeable wall as is also done by Chandesris et al. (2013). T_τ^p is the friction temperature at the permeable wall given by $T_\tau^p = -\langle \overline{w'T'} \rangle + \kappa \partial \langle \overline{T} \rangle / \partial z_{y=H} / (\rho c_p u_\tau^p)$. Note that the total flux in the whole domain is constant, which is expected if there is no energy production inside the domain and the total heat flux is conserved. The total heat flux has contributions from two leading quantities: the molecular diffusion term or the diffusive term and the wall-normal turbulent heat flux or the convective term. At lower Ri_b where shear stress dominates the flow, the velocity fluctuations are filtered out by the porous matrix and the large-scale fluctuations that do penetrate inside are induced by pressure waves, and do not participate in turbulent mixing. As a result for lower Ri_b, the core of the free channel region is dominated by turbulent heat flux with diffusion taking over in the wall region. However, in the porous region, molecular diffusion dominates since the flow there is mostly laminar in nature. An expected trend is seen with increasing Ri_b with the turbulent heat flux penetrating more into the depth of the solid matrix. At $Ri_b = 10$, the heat flux in almost the whole domain is dominated by wall-normal turbulent heat flux, except in the viscous sublayer where molecular diffusion is present.

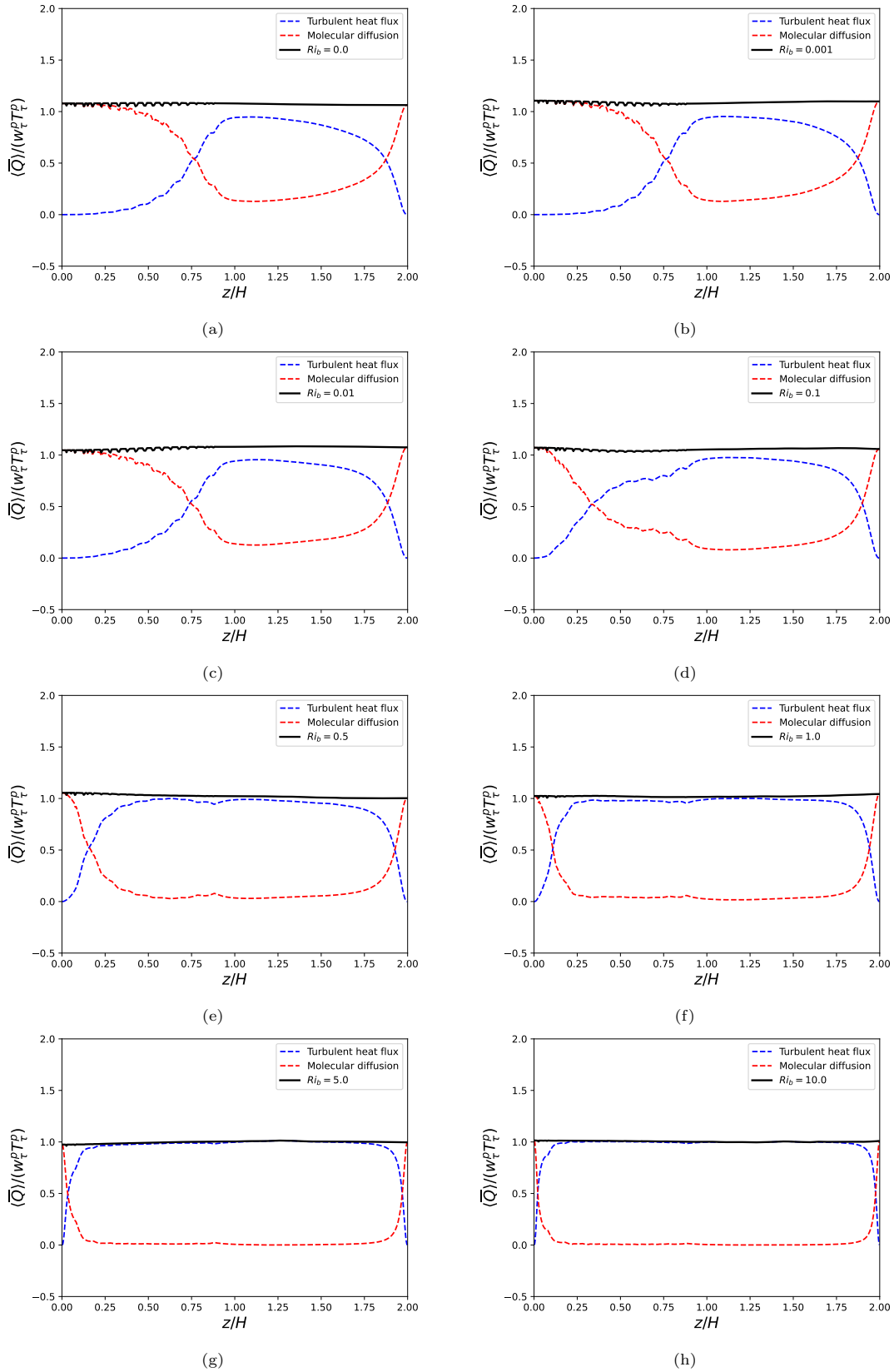

Figure 7.11: Total heat flux budgets normalized with wall-normal friction velocity and friction temperature at permeable wall with contribution from molecular diffusion and turbulent heat flux for varying bulk Richardson number: (a) $Ri_b = 0$, (b) $Ri_b = 0.001$, (c) $Ri_b = 0.01$, (d) $Ri_b = 0.1$, (e) $Ri_b = 0.5$, (f) $Ri_b = 1$, (g) $Ri_b = 5$ and (h) $Ri_b = 10$.

7.5 The flux Richardson number

Analysing the localized contributions of shear and buoyancy to the turbulent kinetic energy is crucial to analyse the changing effects of increasing Richardson number on the flow conditions in mixed convection. The Turbulent Kinetic Energy equation is given by:

$$\frac{\partial k}{\partial t} + \overline{u_j}\frac{\partial k}{\partial x_j} = \overline{-u_i' u_j'}\frac{\partial \overline{u_i}}{\partial x_j} + g\alpha\overline{w'T'} + \frac{\partial\left(\nu\frac{\partial k}{\partial x_j} - \overline{u_j' k} - \frac{1}{\rho}\overline{p' u_j'}\right)}{\partial x_j} + \overline{\nu\left(\frac{\partial u_i'}{\partial x_j}\right)^2}, \tag{7.5.1}$$

where $\alpha = 1/T_{ref}$ for ideal gas. The third and fourth terms are the transport and dissipation terms respectively. These terms are not necessary for the analysis of Ri_f and will be neglected henceforth. For a fully-developed plane channel flow, the TKE is given as:

$$0 = \underbrace{\overline{-u'w'}\frac{\partial \overline{u}}{\partial z}}_{\text{Shear production}} + \underbrace{\frac{g}{T_{ref}}\overline{w'T'}}_{\text{Buoyant production}} + \text{Transport terms} + \text{Dissipation terms} \tag{7.5.2}$$

$$0 = \overline{-u'w'}\frac{\partial \overline{u}}{\partial z}\left(1 - Ri_f\right) + \text{Transport terms} + \text{Dissipation terms}, \tag{7.5.3}$$

where

$$Ri_f = \frac{\alpha g\overline{w'T'}}{-\overline{u'w'}\frac{\partial \overline{u}}{\partial z}} \text{is the flux Richardson number.} \tag{7.5.4}$$

For buoyant production $Ri_f < 0$ and buoyant destruction for $Ri_f > 0$. Figures shown in 7.13 show the buoyancy production, shear production and the portion in the domain where the flux Richardson number approximately equals the bulk Richardson number. 4 Ri_b values have been chosen ranging from low to moderate to high which are 0.001, 0.1, 1 and 10. The flux Richardson number is a localized indicator of dynamical dominance between shear-production and buoyancy production. It is seen in almost all the cases that near the permeable wall, the Ri_f is very low and increases in the log-layer. This is because, at the wall region, the flow is shear dominated and the local Ri_f is low. At some point in the log layer, the Ri_f equals Ri_b. Note that only a portion of the Ri_f graphs, near the permeable wall, ranging from $z/H = 1.1$ to about $z/H = 1.6$ has been shown, to focus the analysis on the buffer layer near the permeable wall. In a way, it can be rationalized that the point where Ri_b and Ri_f are equal, is the position where buoyant production starts dominating over shear production towards the core of the channel. It is noticeable that with increasing Ri_b, this point shifts towards the permeable wall - showing that the shear production zone in the wall layer becomes thinner. It is important to note here that the Ri_b is based on the entire domain height $2H$ whereas Ri_f is a local indicator. So essentially the comparison shown in the Ri_f graphs with Ri_b is more of a qualitative method of showing that near the permeable wall, there is a point where the local Richardson number reaches the bulk value, magnitude-wise.

The Monin-Obukhov length scale qualifies the cut-off limit before which shear production dominates and after which buoyancy production takes over. It is given by:

$$L = \frac{u_\tau^3}{\alpha g Q}, \tag{7.5.5}$$

where u_τ is the friction velocity, which in this case is the one at the permeable wall. α is the volumetric expansion coefficient, g is the acceleration due to gravity and Q is the total heat flux. Pirozzoli et al. (2017) found a scaling $L_{MO}/H \approx 3.34 Ri_b^{-0.85}$ for mixed convection with unstable stratification. Blass et al. (2020) carried on a similar study on wall-sheared thermal convection in a turbulent flow and formulated a -0.91 scaling for L_{MO} with Ri_b. In the present work with turbulent flow over a porous medium with unstable stratification, a similar scaling of $L_{MO}/H \sim Ri_b^{-0.96}$ is obtained. Qualitatively, it is pointless to consider calculating L_{MO}/H fo $Ri_b < 1$ because the values are more than 1. This realistically does not hold any meaning and points to the fact that the whole region is shear dominated. For $Ri_b = 5$ and $Ri_b = 10$, the length scale is given by, 0.59H and 0.32H, from the permeable wall.

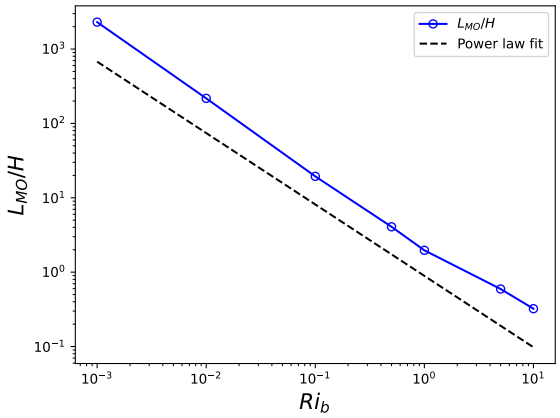

Figure 7.12: Variation of the Monin-Obukhov length scale for the turbulent channel with varying bulk Richardson number. A power law fit of $Ri_b^{-0.96}$ is also shown.

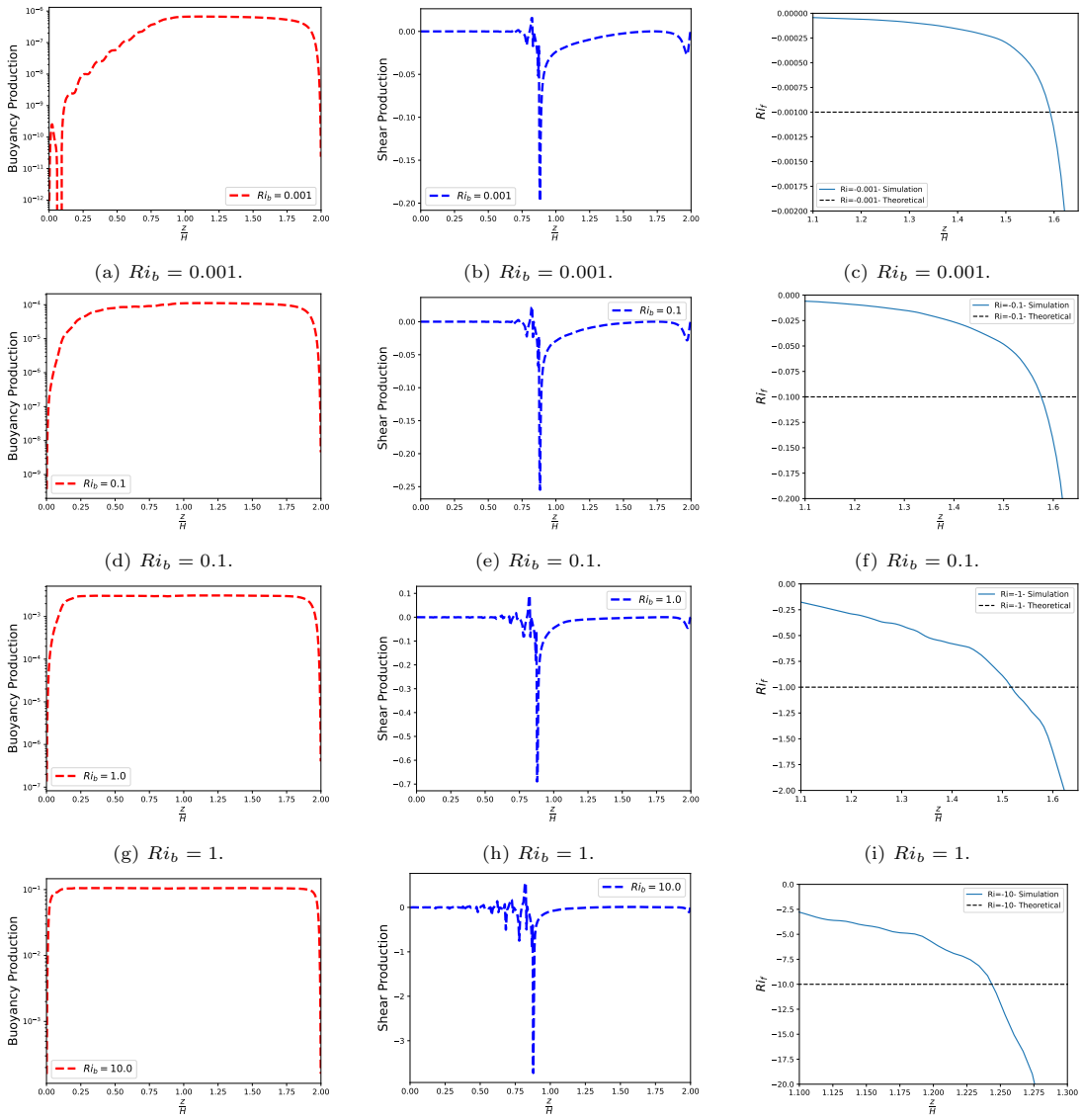

(a) $Ri_b = 0.001$. (b) $Ri_b = 0.001$. (c) $Ri_b = 0.001$.

(d) $Ri_b = 0.1$. (e) $Ri_b = 0.1$. (f) $Ri_b = 0.1$.

(g) $Ri_b = 1$. (h) $Ri_b = 1$. (i) $Ri_b = 1$.

(j) $Ri_b = 10$. (k) $Ri_b = 10$. (l) $Ri_b = 10$.

Figure 7.13: (a),(d),(g),(j) show the buoyancy production term $\frac{g}{T_{ref}}\overline{w'T'}$; (b),(e),(h),(k) show the shear production term -$\overline{u'w'}\frac{\partial \overline{u}}{\partial z}$; (c),(f),(i),(l) show the flux Richardson number Ri_f in the log-layer near the permeable wall.

7.6 Correlation between streamwise and wall-normal fluctuations with temperature fluctuations

Cross-correlation coefficients are used to compare the turbulence production mechanisms between velocity and temperature fluctuations. In the present work, the correlation coefficients analysed are:

- $R_{uw} = \frac{\langle \overline{u'w'} \rangle}{u_{rms} w_{rms}}$
- $R_{uT} = \frac{\langle \overline{u'T'} \rangle}{u_{rms} T_{rms}}$
- $R_{wT} = \frac{\langle \overline{w'T'} \rangle}{w_{rms} T_{rms}}$

As shown in Figure 7.14 common feature seen for all the flow simulations is the dissimilarity or rather opposing trends between R_{uw} and R_{wT}. This shows that across all regimes, the mechanisms behind the generation of wall-normal turbulent heat flux and Reynolds stress are different. However, a similarity is spotted between trends of R_{uw} and R_{uT}. For lower Ri_b, R_{uw} is around 0.4 in the core of the channel region and peaks at 0.6 at the interface of the permeable wall. This peak can be attributed to the presence of Kelvin-Helmholtz instabilities. With increasing Ri_b, R_{uw} decreases in the channel region, which can be indicative of the K-H instability eddies growing smaller in size because of buoyancy breaking them up. Inside the porous region, the Reynolds stress drops almost immediately because of the fluctuations inside the porous matrix being induced by pressure waves.

The correlation between u' and T' essentially is an indicator of how efficiently streamwise velocity fluctuations transport temperature fluctuations. It is seen that there is a persistent peak present at the permeable wall for R_{uT} because of the roughness layer giving rise to instabilities. However, in the core of the channel, with increasing Ri_b till 0.1, the streamwise turbulent heat flux peaks and then dips when the Ri_b increases further. This shows that as buoyancy sets in, the streamwise velocity fluctuation facilitates the transport of temperature fluctuations more efficiently. The wall-normal velocity correlation with temperature increases with Ri_b. Post $Ri_b = 0.1$, R_{uT} starts dipping and R_{wT} rises. This shows that with the increasing dominance of buoyancy wall-normal velocity becomes more active in transporting temperature flux than streamwise velocity fluctuations.

In the porous region, R_{uT} goes approximately around zero because of velocity fluctuations being inactive and having no relation with the temperature fluctuations, which does not reduce to zero. R_{wT} on the other hand keeps increasing Ri_b and reaches a near 1 value for $Ri_b > 1$. This shows that the increase in temperature fluctuations can almost wholly be attributed to w', which also increases due to buoyancy-induced turbulence penetrating the matrix. To delve deeper into the production mechanisms of temperature and streamwise velocity fluctuations, the transport equations for these fluctuations need to be analysed, which can be performed in future work.

7.7 Stanton number vs. Friction coefficient

Forced convection is best quantified using the Stanton number, which is the total heat transfer non-dimensionalized by the thermal capacity of the fluid. The Stanton number is given as:

$$St = \frac{h_{conv}}{\rho c_p u_b}, \tag{7.7.1}$$

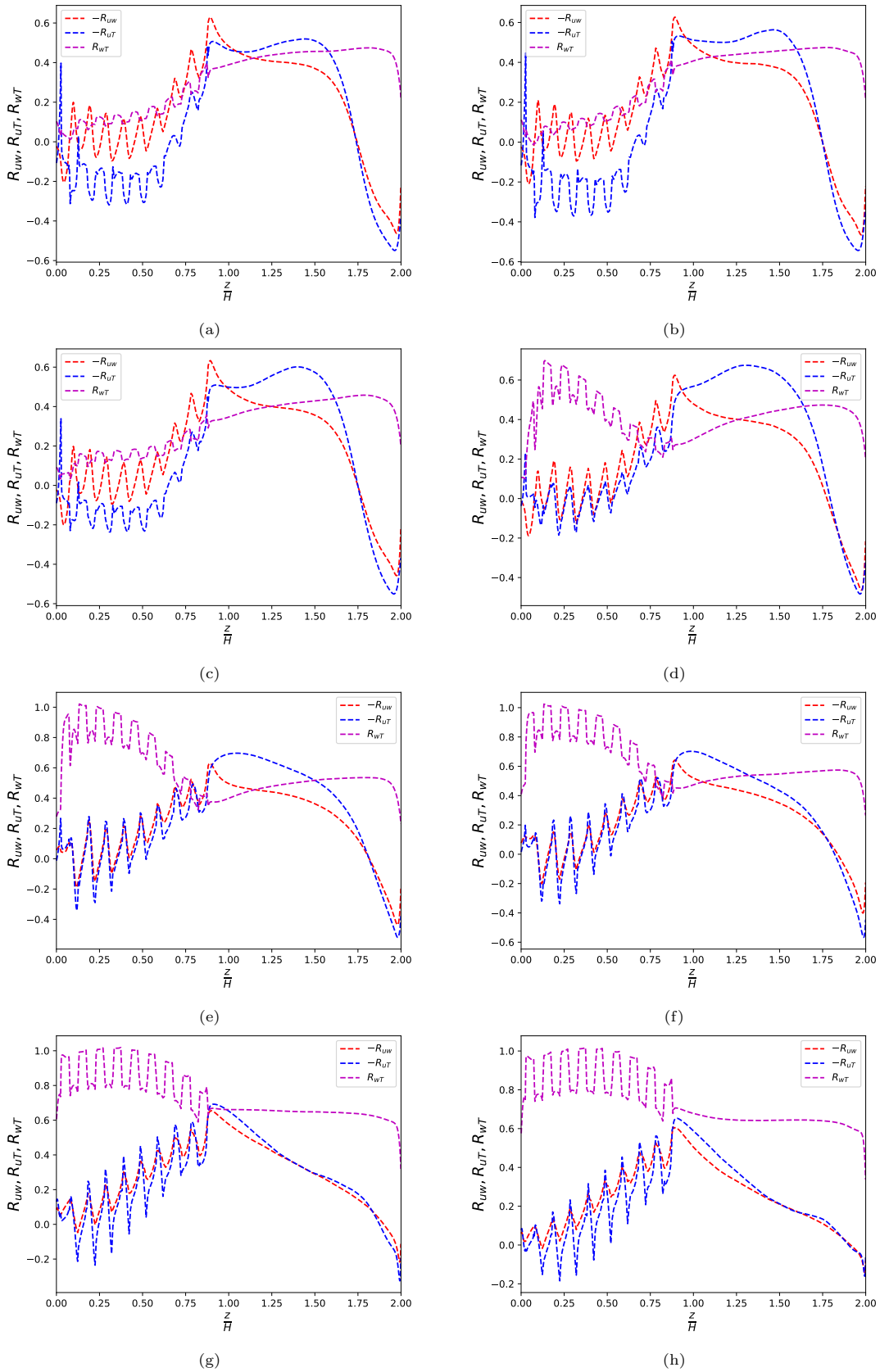

Figure 7.14: Correlation coefficients R_{uw}, R_{uT} and R_{wT} with varying Richardson number: (a) $Ri_b = 0$, (b) $Ri_b = 0.001$, (c) $Ri_b = 0.01$, (d) $Ri_b = 0.1$, (e) $Ri_b = 0.5$, (f) $Ri_b = 1$, (g) $Ri_b = 5$ and (h) $Ri_b = 10$.

where h_{conv} is the convective heat transfer coefficient. It can also be expressed in terms of the Nusselt number Nu as:

$$St = \frac{h_{conv}}{\rho c_p u_b} \tag{7.7.2}$$

$$= \frac{h_{conv} H}{k} \frac{\nu}{u_b H} \frac{k}{\rho c_p \nu} \tag{7.7.3}$$

$$= \frac{Nu}{Re_b Pr}. \tag{7.7.4}$$

The Coefficient of Friction on the other hand is the non-dimensionalized version of the shear stress exerted on the wall, given as:

$$C_f = 2\frac{\tau}{\rho u_b^2} \tag{7.7.5}$$

$$= 2\frac{u_\tau^2}{u_b^2}. \tag{7.7.6}$$

The Reynolds analogy relates the momentum transfer to heat transfer in a turbulent flow. It is essentially necessary in cases where an approximation of the heat transfer needs to be made, and can be done so if shear stress is known. The Reynolds analogy states that essentially:

$$St = \frac{C_f}{2} \tag{7.7.7}$$

In the present case, turbulent channel flow over a porous layer is simulated. So obviously, the Reynolds analogy is not expected to hold. This is because the first assumption of the analogy states that the flow should not have an external pressure gradient, which is not the case in a channel flow. Also, the Pr should be equal to 1, whereas in the present case, $Pr = 0.1$. This necessarily means that from solely a theoretical perspective, Reynolds analogy breaks down. A modification to the Reynolds analogy was provided by the Chilton-Colburn analogy to include the effect of the Prandtl number not equal to 1. The Chilton-Colburn analogy is given by:

$$StPr^{\frac{2}{3}} = \frac{C_f}{2}. \tag{7.7.8}$$

But the Prandtl number limit for the validity of the Chilton-Colburn analogy is $Pr > 0.6$, so technically would not be applicable to the present case. So it is important to decipher the relationship between heat transfer and skin friction at the permeable wall. Figure 7.15 shows the variation of St with $C_{f,p}$ for Ri_b. In the shear regime, not much conclusion about the $St - Cf$ relation can be drawn from the graph. From $Ri_b = 0.1$ onwards, a linear relation can be formulated given as:

$$St = 0.185 C_{f,p}. \tag{7.7.9}$$

Although a linear relation is established for the buoyancy regime, it is important to determine if the Stanton number increases at a faster rate than the coefficient of friction with increasing Ri_b. This will help determine if the increasing effect of buoyancy has a dominant effect on increasing heat transfer or momentum transfer. Differentiating both sides of equation 7.7.9 with respect to bulk Ri_b:

$$\frac{\partial St}{\partial Ri_b} = 0.185 \ \frac{\partial C_{f,p}}{\partial Ri_b}. \tag{7.7.10}$$

Table 7.1, Figure 7.16a and 7.16b also show that the friction coefficient at permeable wall increases faster than the increase in Stanton number. The trend in the shear regime does not provide any logical conclusion, but in the buoyancy regime, the dominance of the rate of change of $C_{f,p}$ over that of St is clear. This is an expected result. While both the friction drag from the roughness layer and the form drag or pressure drag contribute to increasing the friction coefficient with increasing Re_τ, the heat transfer enhancement only occurs due to friction drag. An obvious

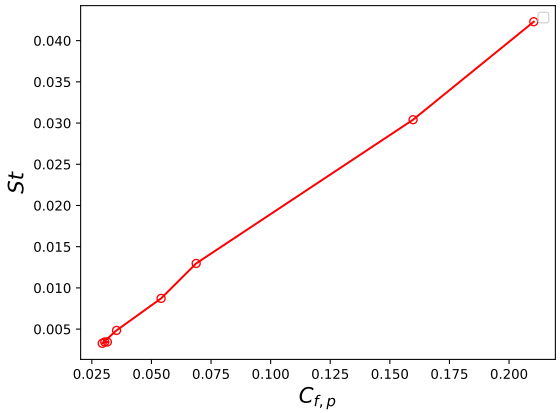

Figure 7.15: Variation of Stanton number with the coefficient of friction at the permeable wall for $Ri_b > 0.1$.

question might arise if Re_τ^p is being calculated at the centerline of the domain $z = H$ and not across the roughness layer exactly, how does form drag come into play? It is assumed that $z = H$ falls inside the boundary layer due to flow over the porous medium, and the profile of the roughness layer will have the influence of the friction Reynolds number calculated at $z = H$. On the other hand, the pressure drag plays no role in the increase of St.

So it can be sufficiently concluded that in mixed convection with turbulent flow over a porous wall layer, the heat transfer enhancement is slower than the shear stress enhancement at the permeable wall. For moderate to high Ri_b, a linear relation between heat transfer and skin friction can be formulated, where the rate of change of heat transfer with increasing Ri_b is smaller by about $\mathcal{O}(10)$ than the rate of change of skin friction coefficient.

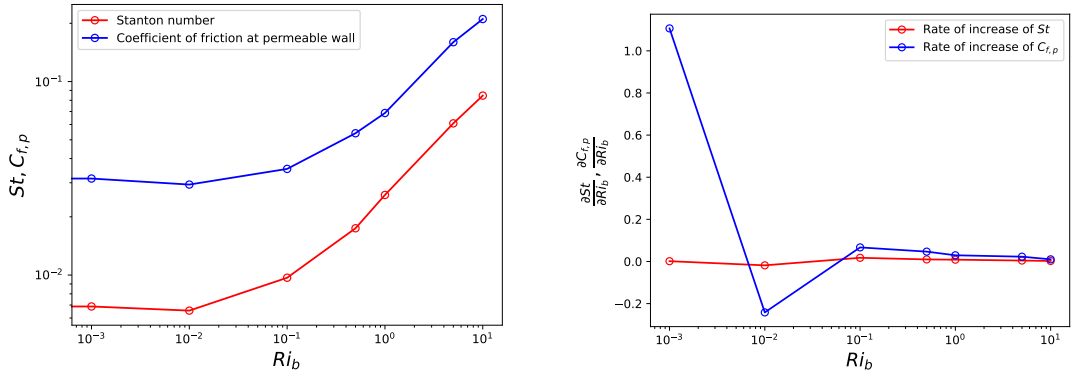

(a) (b)

Figure 7.16: (a)Variation of Stanton number and Coefficient of Friction at the permeable wall with bulk Richardson number; (b)Variation of the rate of change of Stanton number and Coefficient of Friction at the permeable wall with bulk Richardson number.

7.8 The Nusselt and Rayleigh number scaling

The dependence of the Nusselt number on the Rayleigh number has been one of the central focus points in the thesis from the start. It is seen that for Rayleigh-Bénard convections, a 0.25 scaling holds. For natural convection in a porous media, the scaling is around 1. However, the scaling for mixed convection over a porous wall layer remains undetermined. The present work tried to shed light on this. From Figure 7.17, it is seen, that two separate regime scalings can be formulated. When buoyancy starts dominating, from $Ri_b = 1$ around $Ra \sim 10^7$, a 0.58 power-law fit can be formulated. This is interesting because, in the buoyant regime, this scaling falls between the pure Rayleigh-Bénard scaling and the porous media convection power law. Summarizing, the $Nu - Ra$ scaling can be formulated for mixed convection in the buoyancy regime, where the Re_b and Pr are kept constant, as:

$$\boxed{Nu \approx 0.0016 Ra^{0.53}}, \tag{7.8.1}$$

in the buoyancy-dominated regime.

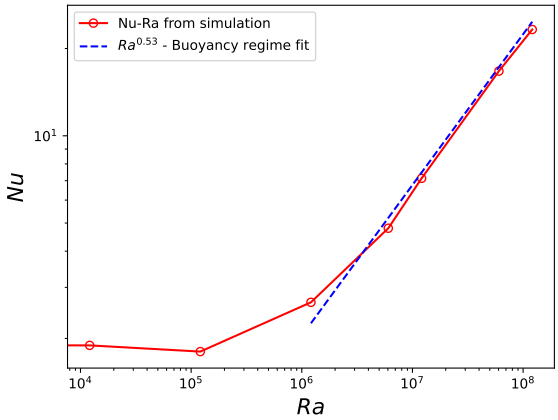

Figure 7.17: Nusselt number with varying Rayleigh number.

7.9 Regime map

The bulk Richardson number is an indicator of the bulk dominance of buoyancy over shear production. For varying Ri_b, it is expected that the regimes of the flow will change. At low Ri_b, the flow is shear driven and inside the porous region, the flow is almost laminar. With increasing Ri_b, the regime passes over to being in a buoyancy-driven zone. It is thus important to first distinguish between these two regimes, based on length and velocity scales. Firstly, for shear-driven flows, a clear wall region and a logarithmic region can be distinguished. However, at the permeable wall, the effect of viscosity is negligible. So the single relevant length scale for the inner region is $\sqrt{K_c}$. For the porous region also, the length scale is $\sqrt{K_c}$. This is because Re_K is high and the roughness Reynolds number is relatively small. For buoyancy regimes, logarithmic regions cannot be distinguished clearly and the wall regions get narrower. The Monin-Obukhov length scale is the relevant length scale in this case. For the shear-dominated region, the length scale is L, whereas the length scale in the buoyancy-dominated region is $H - L$. d_p is the relevant length scale in the porous region because in the buoyancy regime Re_d is high and dominates over the effect of Re_K. Figure 7.18 shows the scaling regions for shear-driven and buoyancy-driven flows. The velocity and length scaling for the shear-driven cases are given by:

- 1 : Velocity scale - u_τ^w; Length scale - ν/u_τ^w.
- 2 : Velocity scale - u_τ^w; Length scale - $H - \delta_w$.
- 3 : Velocity scale - u_τ^p; Length scale - δ_w.
- 4 : Velocity scale - u_τ^p; Length scale - $K_c^{0.5}$.

- 5 : Velocity scale - u_τ^p; Length scale - $K_c^{0.5}$.

Similarly, for buoyancy-driven cases, the scaling is given by:

- 1 : Velocity scale - u_τ^w; Length scale - ν/u_τ^w.
- 2 : Velocity scale - w_f; Length scale - $H - L$.
- 3 : Velocity scale - u_τ^p; Length scale - L.
- 4 : Velocity scale - u_τ^p; Length scale - d_p.

Here δ_w is the position of maximum velocity and L is the Monin-Obukhov length scale. K_c is the permeability at the top layer of the porous row. w_f is the outer region convective velocity scale given by $(g\alpha\Delta TH)^{\frac{1}{3}}$. d_p is the cube dimension in the porous media.

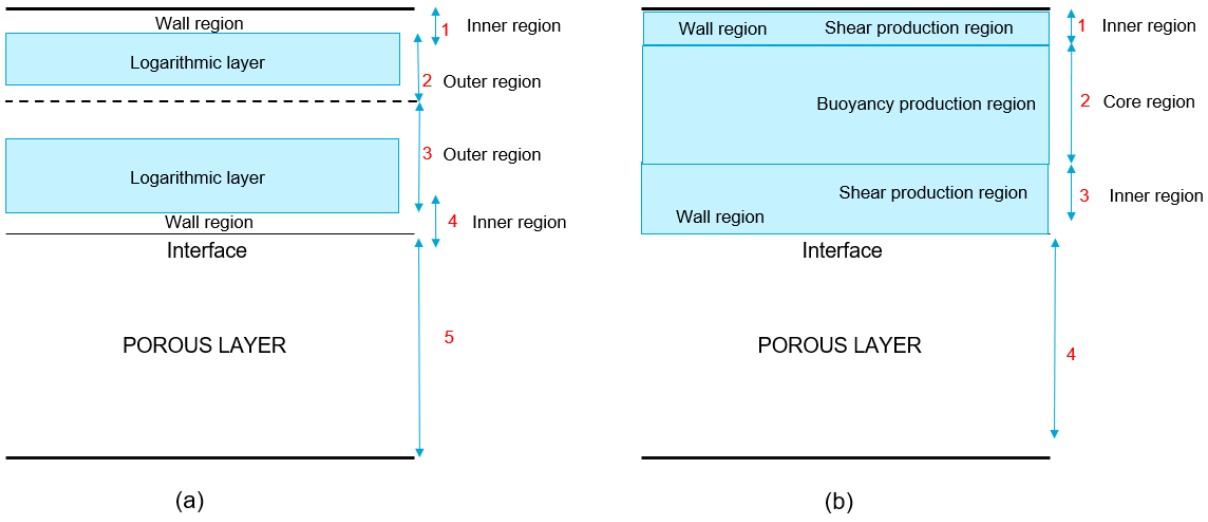

Figure 7.18: (a) Shear-driven flow scaling regions (dotted line represents the distance δ_w from the solid line at the interface); (b) Buoyancy-driven flow scaling regions.

A more detailed regime map is shown in Figure 7.19a. The red line in the figure refers to the critical Ra after which convective rolls are triggered in natural convection. The blue line is the critical limit for convection in porous media. Below this limit, the convective structures appear as large-scale circulations, while above it columnar plumes appear. The green line denotes the shift from a shear-dominated regime to a buoyancy-dominated zone.

- Figure 7.19b shows temperature fluctuation for $Ri_b = 0.001$ which shows the thermal structures for the lower end of shear driven - convective roll-dominated regime.
- Figure 7.19c shows temperature fluctuation for $Ri_b = 0.1$ which shows the thermal structures for the higher end of shear driven - convective roll-dominated regime.
- Figure 7.19d shows temperature fluctuation for $Ri_b = 1$ which shows the thermal structures for the critical limit between shear-driven and buoyancy-driven - convective columnar plume dominated regime.
- Figure 7.19e shows temperature fluctuation for $Ri_b = 10$ which shows the thermal structures for the higher end of buoyancy-driven - convective columnar plume-dominated regime.

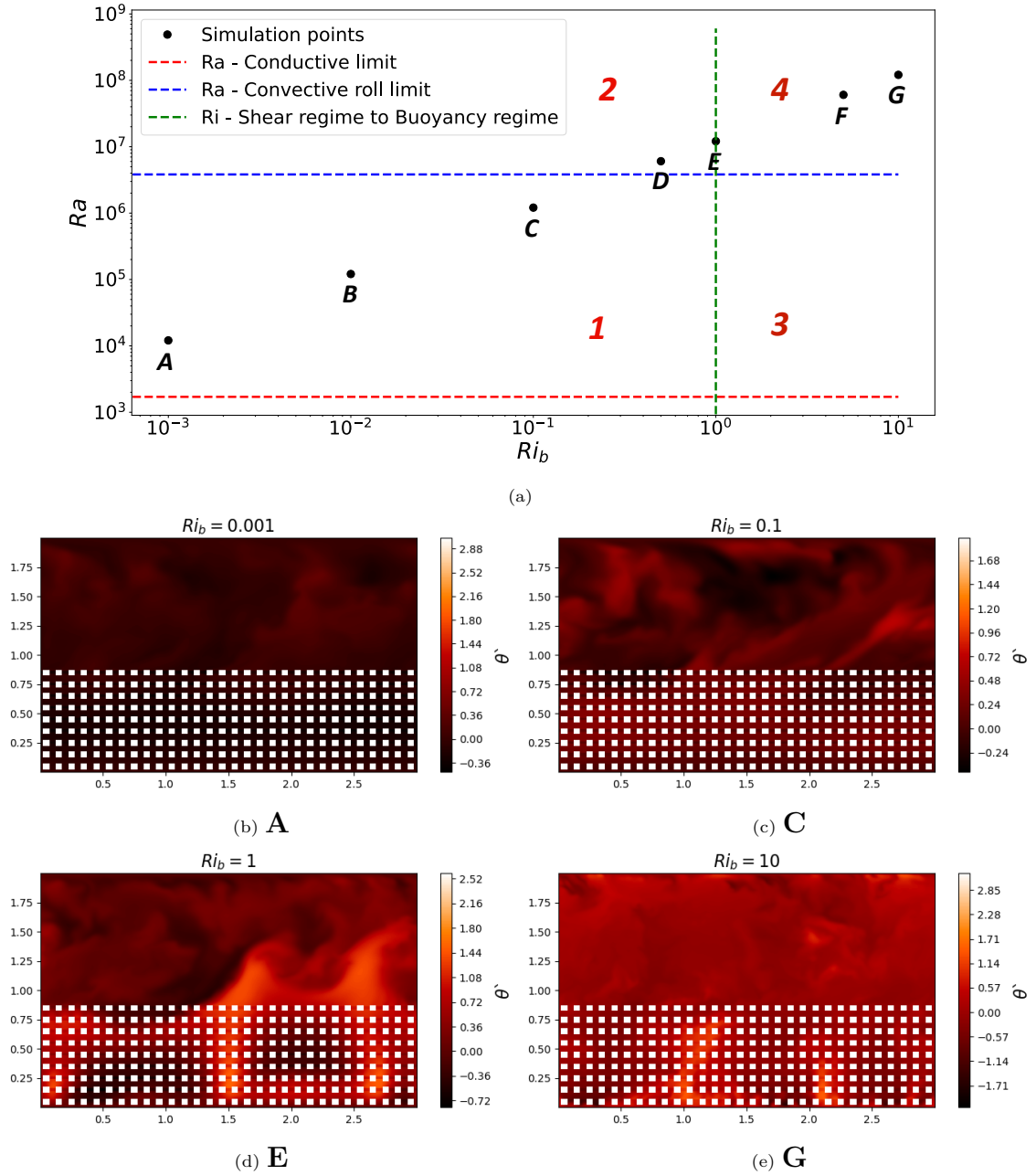

(a)

(b) **A**

(c) **C**

(d) **E**

(e) **G**

Figure 7.19: (a) Regime map defining 4 distinct regimes: **1**-Shear driven with convective roll; **2**-Shear driven with convective columnar structures; **3**-Buoyancy driven with convective rolls and **4**-Buoyancy driven with convective columnar structures; temperature fluctuation contour for (b) $Ri_b = 0.001$ - point **A**, (c) $Ri_b = 0.1$ - point **C**, (d) $Ri_b = 1$ - point **E** and (d) $Ri_b = 10$ - point **G**.

8

Conclusions and Future Recommendations

8.1 Summary and Conclusion

The present thesis aimed at shedding light on the physics governing mixed convection with a turbulent flow over a porous wall layer. The evolution of momentum and thermal characteristics for Rayleigh-Bénard convection and convection in porous media have been studied in the past extensively as described in the literature review. Also, quite a few DNS studies have focused on mixed convection in turbulent channels with unstable stratification. However, an intensive literature review revealed that there lacks a study providing a framework combining all of the conditions. The primary goal was to thus establish this framework using high-fidelity numerical simulations.

Breugem and Boersma (2005) had carried out simulations for turbulent flow over an ordered porous media. Chandesris et al. (2013) extended this study to include temperature as a passive scalar. The present thesis adopted the model used by the authors where the lower half of a channel is occupied by porous media with a porosity of 0.875. The upper half is a free channel region with turbulent flow. The present work extended the study to induce buoyancy-driven convection. The Navier-Stokes equations are modified to include the Bousinnesq approximation and the Immersed Boundary forcing term. These equations are temporally discretized using a 3rd-order Runge-Kutta numerical scheme. Further, these equations are solved using a finite-difference solver CaNS (Costa (2018)). The porous media is simulated using a volume-penalization IBM, where the volume fraction field is formulated by multiplying line fractions.

Firstly, validations are carried out for buoyancy-driven convection in a differentially heated cavity. Following this, Rayleigh-Bénard convection inside a duct is simulated and the temperature statistics are validated. The Immersed Boundary method to model the porous media is finally implemented and the momentum and temperature statistics are checked with literature. Having successfully validated the setup, convection is included in the model. The bulk Reynolds number and Prandtl number are kept constant, whereas the bulk Richardson number is varied from 0 to 10, to cover the spectrum from pure shear-driven turbulent channel flow to buoyancy-driven convection over a porous media.

The mean and root-mean-squared statistics for velocity and temperature reveal that at about $Ri_b = 0.1$, a distinct change is seen in the type of profiles. For both mean velocity and temperature, the profile blunts out in the channel region with increasing Ri_b. It is also observed that wall-normal fluctuations start dominating over streamwise fluctuations when buoyancy starts dominating. With

increasing Ri_b, the fluctuations penetrate the solid matrix more, showing that the filtering of small-scale fluctuations by the porous media is rendered almost ineffective. In the purely shear-driven case, temperature fluctuations inside the porous media are induced by pressure waves, whereas for higher Ri_b, turbulent mixing directly aids the increase of fluctuations.

To analyse the effects of how the shear stress varies in characteristics between the permeable wall and the top wall, stress budgets are formulated. It is seen that viscous stress does not change with increasing Ri_b and dominates only near the top wall. At the permeable wall, due to the relaxation of no-slip condition, the viscous stress is lower than at the top wall. The Reynolds stress dominates in the channel region except at the top wall. It is also seen that the Reynolds stress increases in the porous region with increasing Ri_b. The most interesting observation was that the shear stress at the permeable wall increases at a faster rate than the top, solid wall. A heat-flux budget is also analysed, and it is seen that at lower Ri_b, the channel region is dominated by turbulent heat flux, but the porous media is dominated by molecular diffusion. At higher Ri_b, this changes and as turbulence penetrates the solid matrix the turbulent heat flux dominates the entire domain except at the top and bottom walls.

Cross-correlation coefficients reveal that, at lower Ri_b, the buoyancy induces streamwise fluctuation increases which transports temperature fluctuations more efficiently in the channel. At higher Ri_b, this role is taken up by wall-normal fluctuations, which also aid temperature fluctuations penetrate the porous layer. Finally, different length and velocity scales are formulated for shear-driven and buoyancy-driven regimes for the different regions in the channel flow and the porous layer. A deeper analysis reveals the existence of 4 distinct convective regimes - shear-driven or buoyancy-driven based on if $Ri_b < 1$ or $Ri_b > 1$. Further, distinct regimes are also formulated based on critical Ra for triggering convection in free media and porous media. Subsequent temperature fluctuation contours reveal that indeed the theorized regime changes are observed through the simulations.

8.2 Future Recommendations

- The present simulation campaign deals with constant Re_b and constant Pr. It will be interesting to see what kind of regime changes are seen when either of these is varied along with Ri_b.
- A filter can be adapted to smoothen out the averaging in the porous media using a weighting function, as used by Breugem and Boersma (2005), so that one can devise closures for the volume-filtered Navier-Stokes equations.
- The permeability K is kept constant, which in turn keeps the Darcy number constant. Further studies could focus on varying the permeability, by varying the porosity of the porous media.
- The temperature equations are now second-order discretized. Further work can include higher-order flux-preserving schemes to simulate higher Ri_b more accurately.
- GPU-acceleration can be implemented to make the computational time lower to counter the thermal time scale disparity between porous media and the channel region.
- A more accurate Immersed Boundary method can be implemented so that the edges of the cubes are more distinct and are not smoothened out. The stress IBM used by Breugem and Boersma (2005) can be a suitable choice for a more accurate approach to modelling the cubes.

9

Appendix

9.1 Effective thermal conductivity

It is important to analyse if the effective thermal conductivity of the porous media matches or comes close to theoretical models. In the present simulation, $k_s = 0$ to maintain adiabatic cubes, $k_f = 0.001818$ and $\phi = 0.125$.

9.1.1 Maxwell's model for dilute suspension of spherical particles

Maxwell's model of effective thermal conductivity states that the effective thermal conductivity of a dilute suspension of spherical particles (thermal conductivity k_s in a fluid (thermal conductivity k_f), can be estimated as:

$$k_{eff} = k_f \left(1 + \frac{3\phi}{\frac{k_s + 2k_f}{k_s - k_f} - \phi} \right).$$

Substituting the values, the following value is obtained:

$$\boxed{k_{eff} = 0.001818 \left(\frac{2 - 2 \times 0.125}{2 + 0.125} \right) = 0.001497}.$$

Volume of fluid approach for effective thermal conductivity

VOF approach for effective thermal conductivity is given by :

$$\boxed{k_{eff} = k_f(1 - \phi) + k_s\phi = 0.001818 \times 0.875 = 0.001591}.$$

9.1.2 Effective thermal conductivity calculation from present simulation

The heat transfer $\dot{q}$ is estimated as the average of the heat transfer rate from top and bottom boundaries.

$$\dot{q}_{top} = k_f \left.\frac{\partial T}{\partial z}\right|_{top} = 0.007744$$

and

$$\dot{q}_{bottom} = k_f \left.\frac{\partial T}{\partial z}\right|_{bottom} = 0.007846.$$

Thus, $\dot{q}_{average} = 0.007795$.
The k_{eff} can be estimated as:

$$\dot{q}_{average} = k_{eff} \left.\frac{\partial T}{\partial z}\right|_{laminar}$$

and therefore

$$k_{eff} = \frac{\dot{q}_{average}}{\left.\frac{\partial T}{\partial z}\right|_{laminar}}.$$

This gives :

$$\boxed{k_{eff} = 0.007795/4.608 = 0.0016916}.$$

This shows that the calculated k_{eff} is indeed close to the Volume-Of-Fluid approach taken to calculate the effective thermal conductivity in the code.

9.2 Calculation of intrinsic RMS and heat-flux quantities

The intrinsic Reynolds averaged mean temperature $\overline{\langle T_m \rangle}$ is given as : $\overline{\langle T_m \rangle} = \frac{\overline{\gamma T}}{\overline{\gamma}}$ where γ is the fluid phase indicator function.
To estimate the intrinsic Reynolds averaged RMS temperature we get:

$$\begin{aligned}
\overline{\langle T_{rms} \rangle} =& \sqrt{\frac{\overline{\gamma (T - T_m)^2}}{\overline{\gamma}}} \\
&= \sqrt{\frac{\overline{\gamma (T^2 + T_m^2 - 2TT_m)}}{\overline{\gamma}}} \\
&= \sqrt{\frac{\overline{\gamma T^2} + \overline{\gamma T_m^2} - \overline{2\gamma T T_m}}{\overline{\gamma}}} \\
&= \sqrt{\frac{\overline{\gamma T^2} + \overline{\gamma} T_m^2 - \overline{2\gamma T T_m}}{\overline{\gamma}}} \\
&= \sqrt{\frac{\overline{\gamma T^2}}{\overline{\gamma}} + \frac{\overline{\gamma} T_m^2}{\overline{\gamma}} - \frac{\overline{2\gamma T T_m}}{\overline{\gamma}}} \\
&= \sqrt{\frac{\overline{\gamma T^2}}{\overline{\gamma}} + T_m^2 - 2T_m^2} \\
&= \sqrt{\frac{\overline{\gamma T^2}}{\overline{\gamma}} - T_m^2} \\
&= \sqrt{\frac{\overline{\gamma T^2}}{\overline{\gamma}} - \left(\frac{\overline{\gamma T}}{\overline{\gamma}} \right)^2}.
\end{aligned}$$

The intrinsic Reynolds averaged mean streamwise velocity $\overline{\langle u_m \rangle}$ is given as : $\overline{\langle u_m \rangle} = \frac{\overline{\gamma u}}{\overline{\gamma}}$ where γ is the fluid phase indicator function.

To estimate the intrinsic Reynolds averaged streamwise turbulent heat flux we get:

$$\begin{aligned}
\overline{\langle u'T' \rangle} =& \frac{\overline{\gamma (u - u_m)(T - T_m)}}{\gamma} \\
&= \frac{\overline{\gamma uT - \gamma uT_m - \gamma u_m T + \gamma u_m T_m}}{\gamma} \\
&= \frac{\overline{\gamma uT} - \overline{\gamma uT_m} - \overline{\gamma u_m T} + \overline{\gamma u_m T_m}}{\overline{\gamma}} \\
&= \frac{\overline{\gamma uT}}{\overline{\gamma}} - \frac{\overline{\gamma uT_m}}{\overline{\gamma}} - \frac{\overline{\gamma u_m T}}{\overline{\gamma}} + \frac{\overline{\gamma u_m T_m}}{\overline{\gamma}} \\
&= \frac{\overline{\gamma uT}}{\overline{\gamma}} - \frac{\overline{\gamma u} T_m}{\overline{\gamma}} - \frac{\overline{\gamma u_m} T}{\overline{\gamma}} + \frac{\overline{\gamma} u_m T_m}{\overline{\gamma}} \\
&= \frac{\overline{\gamma uT}}{\overline{\gamma}} - 2u_m T_m + u_m T_m \\
&= \frac{\overline{\gamma uT}}{\overline{\gamma}} - u_m T_m \\
&= \frac{\overline{\gamma uT}}{\overline{\gamma}} - \left(\frac{\overline{\gamma u}}{\overline{\gamma}} \right) \left(\frac{\overline{\gamma T}}{\overline{\gamma}} \right).
\end{aligned}$$

Bibliography

G. Ahlers, S. Grossmann, and D. Lohse. Heat transfer and large scale dynamics in turbulent rayleigh-bénard convection. *Reviews of Modern Physics*, 81:503–537, 4 2009. ISSN 00346861. doi: 10.1103/RevModPhys.81.503.

R. N. Anderson, M. A. Hobart, and M. G. Langseth. Geothermal convection through oceanic crust and sediments in the indian ocean. *Science*, 204(4395):828–832, 1979. doi: 10.1126/science.204.4395.828. URL `https://www.science.org/doi/abs/10.1126/science.204.4395.828`.

M. Ardekani, O. Abouali, F. Picano, and L. Brandt. Heat transfer in laminar couette flow laden with rigid spherical particles. *Journal of Fluid Mechanics*, 834:308–334, 2018. doi: 10.1017/jfm.2017.709.

M. A. Bees. Advances in bioconvection. *Annual Review of Fluid Mechanics*, 52(1):449–476, 2020. doi: 10.1146/annurev-fluid-010518-040558. URL `https://doi.org/10.1146/annurev-fluid-010518-040558`.

J. Birkholzer. potential-impacts-of-co2-leakage-on-groundwater-quality. 2009. URL `https://eesa.lbl.gov/projects/potential-impacts-of-co2-leakage-on-groundwater-quality/`.

A. Blass, X. Zhu, R. Verzicco, D. Lohse, and R. J. A. M. Stevens. Flow organization and heat transfer in turbulent wall sheared thermal convection. *Journal of Fluid Mechanics*, 897:A22, 2020. doi: 10.1017/jfm.2020.378.

J. Bousinessq. Théorie analytique de la chaleur. 1903.

W. P. Breugem and B. J. Boersma. Direct numerical simulations of turbulent flow over a permeable wall using a direct and a continuum approach. *Physics of Fluids*, 17(2):025103, 2005. doi: 10.1063/1.1835771. URL `https://doi.org/10.1063/1.1835771`.

W. P. Breugem, B. J. BOERSMA, and R. E. UITTENBOGAARD. The influence of wall permeability on turbulent channel flow. *Journal of Fluid Mechanics*, 562:35–72, 2006. doi: 10.1017/S0022112006000887.

R. Britter and S. Hanna. Flow and dispersion in urban areas. *ARFM*, 35:469–496, Jan 2003. doi: 10.1146/annurev.fluid.35.101101.161147. URL `https://doi.org/10.1146/annurev.fluid.35.101101.161147`.

K. Bühler, K. R. Kirchartz, and H. Oertel. Steady convection in a horizontal fluid layer. *Acta Mechanica*, 31(3-4):155–171, Sept. 1979. doi: 10.1007/bf01176845. URL `https://doi.org/10.1007/bf01176845`.

B. Castaing, G. Gunaratne, F. Heslot, L. Kadanoff, A. Libchaber, S. Thomae, X.-Z. Wu, S. Zaleski, and G. Zanetti. Scaling of hard thermal turbulence in rayleigh-bénard convection. *Journal of Fluid Mechanics*, 204:1–30, 1989. doi: 10.1017/S0022112089001643.

M. Chandesris, A. D'Hueppe, B. Mathieu, D. Jamet, and B. Goyeau. Direct numerical simulation of turbulent heat transfer in a fluid-porous domain. *Physics of Fluids*, 25(12):125110, 2013. doi: 10.1063/1.4851416. URL https://doi.org/10.1063/1.4851416.

F. Chillà and J. Schumacher. New perspectives in turbulent rayleigh-bénard convection. *European Physical Journal E*, 35, 7 2012. ISSN 12928941. doi: 10.1140/epje/i2012-12058-1.

X. Chu, G. Yang, S. Pandey, and B. Weigand. Direct numerical simulation of convective heat transfer in porous media. *International Journal of Heat and Mass Transfer*, 133:11–20, 2019. ISSN 0017-9310. doi: https://doi.org/10.1016/j.ijheatmasstransfer.2018.11.172. URL https://www.sciencedirect.com/science/article/pii/S0017931018356436.

O. Coceal, T. G. Thomas, I. P. Castro, and S. E. Belcher. Mean flow and turbulence statistics over groups of urban-like cubical obstacles. *Boundary-Layer Meteorology*, 121(3):491–519, Dec 2006. ISSN 1573-1472. doi: 10.1007/s10546-006-9076-2. URL https://doi.org/10.1007/s10546-006-9076-2.

O. Coceal, A. Dobre, and T. Thomas. Unsteady dynamics and organized structures from dns over an idealized building canopy. *International Journal of Climatology*, 27, Nov 2007. doi: 10.1002/joc.1549. URL https://doi.org/10.1002/joc.1549.

P. Costa. A fft-based finite-difference solver for massively-parallel direct numerical simulations of turbulent flows. *Computers Mathematics with Applications*, 76(8):1853–1862, 2018. ISSN 0898-1221. doi: https://doi.org/10.1016/j.camwa.2018.07.034. URL https://www.sciencedirect.com/science/article/pii/S089812211830405X.

M. De Paoli, F. Zonta, and A. Soldati. Influence of anisotropic permeability on convection in porous media: Implications for geological co2 sequestration. *Physics of Fluids*, 28(5):056601, 2016. doi: 10.1063/1.4947425. URL https://doi.org/10.1063/1.4947425.

V. Dubovsky, G. Ziskind, S. Druckman, E. Moshka, Y. Weiss, and R. Letan. Natural convection inside ventilated enclosure heated by downward-facing plate: experiments and numerical simulations. *International Journal of Heat and Mass Transfer*, 44(16):3155–3168, 2001. ISSN 0017-9310. doi: https://doi.org/10.1016/S0017-9310(00)00324-0. URL https://www.sciencedirect.com/science/article/pii/S0017931000003240.

P. Forchheimer. Wasserbewegung durch boden. *Z. Ver. Deutsch, Ing.*, 45:1782–1788, 1901.

B. E. Griffith and N. A. Patankar. Immersed methods for fluid–structure interaction. *Annual Review of Fluid Mechanics*, 52(1):421–448, Jan. 2020. doi: 10.1146/annurev-fluid-010719-060228. URL https://doi.org/10.1146/annurev-fluid-010719-060228.

S. Grossmann and D. Lohse. Scaling in thermal convection: a unifying theory. *Journal of Fluid Mechanics*, 407:27–56, 2000. doi: 10.1017/S0022112099007545.

S. Grossmann and D. Lohse. Thermal convection for large prandtl numbers. *Phys. Rev. Lett.*, 86: 3316–3319, Apr 2001. doi: 10.1103/PhysRevLett.86.3316. URL https://link.aps.org/doi/10.1103/PhysRevLett.86.3316.

S. Grossmann and D. Lohse. Fluctuations in turbulent rayleigh–bénard convection: The role of plumes. *Physics of Fluids*, 16(12):4462–4472, 2004. doi: 10.1063/1.1807751. URL https://doi.org/10.1063/1.1807751.

G. Grötzbach. Direct numerical simulation of laminar and turbulent bénard convection. *Journal of Fluid Mechanics*, 119:27–53, 1982. ISSN 14697645. doi: 10.1017/S0022112082001256.

G. Hadley. Vi. concerning the cause of the general trade-winds. *Philosophical Transactions of the Royal Society of London*, 39(437):58–62, 1735. doi: 10.1098/rstl.1735.0014. URL https://royalsocietypublishing.org/doi/abs/10.1098/rstl.1735.0014.

H. Hassanzadeh, M. Pooladi-Darvish, and D. Keith. The effect of natural flow of aquifers and associated dispersion on the onset of buoyancy-driven convection in a saturated porous medium. *AIChE Journal*, 55:475–485, Feb 2009. doi: 10.1002/aic.11664. URL https://doi.org/10.1002/aic.11664.

F. Heslot, B. Castaing, and A. Libchaber. Transitions to turbulence in helium gas. *Phys. Rev. A*, 36:5870–5873, Dec 1987. doi: 10.1103/PhysRevA.36.5870. URL https://link.aps.org/doi/10.1103/PhysRevA.36.5870.

D. R. Hewitt. Vigorous convection in porous media. *Proceedings of the Royal Society A: Mathematical, Physical and Engineering Sciences*, 476(2239):20200111, 2020. doi: 10.1098/rspa.2020.0111. URL https://royalsocietypublishing.org/doi/abs/10.1098/rspa.2020.0111.

D. R. Hewitt, J. A. Neufeld, and J. R. Lister. Ultimate regime of high rayleigh number convection in a porous medium. *Phys. Rev. Lett.*, 108:224503, May 2012. doi: 10.1103/PhysRevLett.108.224503. URL https://link.aps.org/doi/10.1103/PhysRevLett.108.224503.

Hinze. *Turbulence*. McGraw-Hill, New York, 1975.

J. Hong and M. C. Kim. Effect of anisotropy of porous media on the onset of buoyancy-driven convection. *Transport in Porous Media*, 72:241–253, Mar 2008. doi: 10.1007/s11242-007-9147-y. URL https://doi.org/10.1007/s11242-007-9147-y.

C. W. Horton and F. T. Rogers. Convection currents in a porous medium. *Journal of Applied Physics*, 16(6):367–370, 1945. doi: 10.1063/1.1707601. URL https://doi.org/10.1063/1.1707601.

O. Iida and N. Kasagi. Direct Numerical Simulation of Unstably Stratified Turbulent Channel Flow. *Journal of Heat Transfer*, 119(1):53–61, 02 1997. ISSN 0022-1481. doi: 10.1115/1.2824100. URL https://doi.org/10.1115/1.2824100.

J.C.Maxwell. A treatise on electricity and magnetism. *Clarendon Press, Oxford*, 1873.

M. Kaczorowski and C. Wagner. Analysis of the thermal plumes in turbulent rayleigh–bénard convection based on well-resolved numerical simulations. *Journal of fluid mechanics*, 618:89–112, 2009.

T. Kajishima, S. TAKIGUCHI, H. HAMASAKI, and Y. MIYAKE. Turbulence structure of particle-laden flow in a vertical plane channel due to vortex shedding. *JSME International Journal Series B*, 44(4):526–535, 2001. doi: 10.1299/jsmeb.44.526. URL https://doi.org/10.1299/jsmeb.44.526.

R. H. Kraichnan. Turbulent thermal convection at arbitrary prandtl number. *The Physics of Fluids*, 5(11):1374–1389, 1962. doi: 10.1063/1.1706533. URL https://aip.scitation.org/doi/abs/10.1063/1.1706533.

R. Krishnamurti. Some further studies on the transition to turbulent convection. *Journal of Fluid Mechanics*, 60(2):285–303, 1973. doi: 10.1017/S0022112073000170.

G. Kristóf and B. Papp. Application of gpu-based large eddy simulation in urban dispersion studies. *Atmosphere*, 9(11), 2018. ISSN 2073-4433. doi: 10.3390/atmos9110442. URL https://www.mdpi.com/2073-4433/9/11/442.

E. R. Lapwood. Convection of a fluid in a porous medium. *Mathematical Proceedings of the Cambridge Philosophical Society*, 44(4):508–521, 1948. doi: 10.1017/S030500410002452X.

G. Lauriat and V. Prasad. Non-darcian effects on natural convection in a vertical porous enclosure. *International Journal of Heat and Mass Transfer*, 32(11):2135–2148, 1989.

P. Le Quéré. Accurate solutions to the square thermally driven cavity at high rayleigh number. *Computers Fluids*, 20(1):29–41, 1991. ISSN 0045-7930. doi: https://doi.org/10.1016/0045-7930(91)90025-D. URL https://www.sciencedirect.com/science/article/pii/004579309190025D.

W. V. R. Malkus and S. Chandrasekhar. The heat transport and spectrum of thermal turbulence. *Proceedings of the Royal Society of London. Series A. Mathematical and Physical Sciences*, 225 (1161):196–212, 1954. doi: 10.1098/rspa.1954.0197. URL https://royalsocietypublishing.org/doi/abs/10.1098/rspa.1954.0197.

J. Marshall and F. Schott. Open-ocean convection: Observations, theory, and models. *Reviews of Geophysics*, 37(1):1–64, 1999. doi: https://doi.org/10.1029/98RG02739. URL https://agupubs.onlinelibrary.wiley.com/doi/abs/10.1029/98RG02739.

T. T. Meteorology. Ocean convection currents. 2011.

K. Nagano, T. Mochida, and K. Ochifuji. Influence of natural convection on forced horizontal flow in saturated porous media for aquifer thermal energy storage. *Applied Thermal Engineering*, 22 (12):1299–1311, 2002. ISSN 1359-4311. doi: https://doi.org/10.1016/S1359-4311(02)00056-X. URL https://www.sciencedirect.com/science/article/pii/S135943110200056X.

F. T. Nieuwstadt, J. Westerweel, and B. J. Boersma. *Turbulence*. Springer International Publishing, 2016. doi: 10.1007/978-3-319-31599-7. URL https://doi.org/10.1007/978-3-319-31599-7.

P. Nithiarasu, K. Seetharamu, and T. Sundararajan. Natural convective heat transfer in a fluid saturated variable porosity medium. *International Journal of Heat and Mass Transfer*, 40(16): 3955–3967, 1997. ISSN 0017-9310. doi: https://doi.org/10.1016/S0017-9310(97)00008-2. URL https://www.sciencedirect.com/science/article/pii/S0017931097000082.

A. Oberbeck. Über die wärmeleitung der flüssigkeiten bei berücksichtigung der strömungen infolge von temperaturdifferenzen. *Annalen der Physik*, 243(6):271–292, 1879.

J. Otero, L. A. DONTCHEVA, H. JOHNSTON, R. A. WORTHING, A. KURGANOV, G. PETROVA, and C. R. DOERING. High-rayleigh-number convection in a fluid-saturated porous layer. *Journal of Fluid Mechanics*, 500:263–281, 2004. doi: 10.1017/S0022112003007298.

K.-A. Park and A. E. Bergles. Natural Convection Heat Transfer Characteristics of Simulated Microelectronic Chips. *Journal of Heat Transfer*, 109(1):90–96, 02 1987. ISSN 0022-1481. doi: 10.1115/1.3248074. URL https://doi.org/10.1115/1.3248074.

C. S. Peskin. The immersed boundary method. *Acta Numerica*, 11:479–517, Jan. 1972. doi: 10.1017/s0962492902000077. URL https://doi.org/10.1017/s0962492902000077.

S. Pirozzoli, M. Bernardini, R. Verzicco, and P. Orlandi. Mixed convection in turbulent channels with unstable stratification. *Journal of Fluid Mechanics*, 821:482–516, 2017. doi: 10.1017/jfm.2017.216.

V. Prasad, F. Kulacki, and M. Keyhani. Natural convection in porous media. *Journal of Fluid Mechanics*, 150:89–119, 1985.

L. Rayleigh. Lix. on convection currents in a horizontal layer of fluid, when the higher temperature is on the under side. *The London, Edinburgh, and Dublin Philosophical Magazine and Journal of Science*, 32(192):529–546, 1916. doi: 10.1080/14786441608635602. URL https://doi.org/10.1080/14786441608635602.

J. Santiago and A. Martilli. A dynamic urban canopy parameterization for mesoscale models based on computational fluid dynamics reynolds-averaged navier–stokes microscale simulations. *Boundary-Layer Meteorology*, 137:417–439, Dec 2010. doi: 10.1007/s10546-010-9538-4. URL https://doi.org/10.1007/s10546-010-9538-4.

K. Schäfer, B. Frohnapfel, and J. P. Mellado. The effect of spanwise heterogeneous surfaces on mixed convection in turbulent channels. *Journal of Fluid Mechanics*, 950, Oct. 2022. doi: 10.1017/jfm.2022.773. URL https://doi.org/10.1017/jfm.2022.773.

X. Shan. Simulation of rayleigh-bénard convection using a lattice boltzmann method. *Phys. Rev. E*, 55:2780–2788, Mar 1997. doi: 10.1103/PhysRevE.55.2780. URL https://link.aps.org/doi/10.1103/PhysRevE.55.2780.

B. I. Shraiman and E. D. Siggia. Heat transport in high-rayleigh-number convection. *Phys. Rev. A*, 42:3650–3653, Sep 1990. doi: 10.1103/PhysRevA.42.3650. URL https://link.aps.org/doi/10.1103/PhysRevA.42.3650.

S. Sid, Y. Dubief, and V. Terrapon. Direct numerical simulation of mixed convection in turbulent channel flow: On the reynolds number dependency of momentum and heat transfer under unstable stratification. In *Proceedings of the 8th International Conference on Computational Heat and Mass Transfer, ICCHMT 2015*. CÉCI - Consortium des Équipements de Calcul Intensif, 2015.

A. J. Trowbridge, H. J. Melosh, J. K. Steckloff, and A. M. Freed. Vigorous convection as the explanation for pluto's polygonal terrain. *Nature*, 534(7605):79–81, Jun 2016. ISSN 1476-4687. doi: 10.1038/nature18016. URL https://doi.org/10.1038/nature18016.

M. Uhlmann. An immersed boundary method with direct forcing for the simulation of particulate flows. *Journal of Computational Physics*, 209(2):448–476, 2005. ISSN 0021-9991. doi: https://doi.org/10.1016/j.jcp.2005.03.017. URL https://www.sciencedirect.com/science/article/pii/S0021999105001385.

R. Verzicco. Immersed boundary methods: Historical perspective and future outlook. *Annual Review of Fluid Mechanics*, 55(1), Sept. 2023. doi: 10.1146/annurev-fluid-120720-022129. URL https://doi.org/10.1146/annurev-fluid-120720-022129.

Whitaker. *The method of volume averaging*, volume 13. Springer Science & Business Media, 1998.

M. C. Wikipedia. Mantle convection. 2007. URL https://en.wikipedia.org/wiki/Mantle_convection.

R. K. Yadav, M. Heimpel, and J. Bloxham. Deep convection–driven vortex formation on jupiter and saturn. *Science Advances*, 6(46):eabb9298, 2020. doi: 10.1126/sciadv.abb9298. URL https://www.science.org/doi/abs/10.1126/sciadv.abb9298.

P. Yang, C. Huang, Z. Zhang, T. Long, and M. Liu. Simulating natural convection with high rayleigh numbers using the smoothed particle hydrodynamics method. *International Journal of Heat and Mass Transfer*, 166:120758, 2021. ISSN 0017-9310. doi: https://doi.org/10.1016/j.ijheatmasstransfer.2020.120758. URL https://www.sciencedirect.com/science/article/pii/S0017931020336942.

G. Ziskind, V. Dubovsky, and R. Letan. Ventilation by natural convection of a one-story building. *Energy and Buildings*, 34(1):91–101, 2002. ISSN 0378-7788. doi: https://doi.org/10.1016/S0378-7788(01)00080-9. URL https://www.sciencedirect.com/science/article/pii/S0378778801000809.